THÈSE

présentée par

Dulce Carolina CAMACHO MOJICA

pour obtenir le grade de
DOCTEUR DE L'UNIVERSITÉ DE GRENOBLE
(Arrêté ministériel du 7 août 2006)
Spécialité : physique de la matière condensée et du rayonnement

Modélisation des propriétés structurales, électroniques et optiques des nanofils de nitrures GaN/AlN

Modeling of the structural, electronic and optical properties of GaN/AlN nitride nanowires

A thesis submitted on May 25, 2010 for the degree of
Philosophiæ Doctor (PhD) of Grenoble University, France
Speciality: Physics of Condensed Matter and Radiation

Soutenue publiquement le **25 mai 2010**

Thèse dirigée par Dr Frédéric LANÇON et co-dirigée par Dr Yann-Michel NIQUET

Composition du jury

Messieurs	Christophe DELERUE	Rapporteur
	Frank GLAS	Rapporteur
	Michel GENDRY	Membre du jury
	Bruno DAUDIN	Membre du jury
	Yann-Michel NIQUET	Membre du jury
	Frédéric LANÇON	Membre du jury

Thèse préparée au sein du
CEA – Institut Nanosciences et Cryogénie (INAC) – L_Sim – GRENOBLE

THÈSE

présentée par

Dulce Carolina CAMACHO MOJICA

pour obtenir le grade de
DOCTEUR DE L'UNIVERSITÉ DE GRENOBLE
(Arrêté ministériel du 7 août 2006)
Spécialité : physique de la matière condensée et du rayonnement

Modélisation des propriétés structurales, électroniques et optiques des nanofils de nitrures GaN/AlN

Modeling of the structural, electronic and optical properties of GaN/AlN nitride nanowires

A thesis submitted on May 25, 2010 for the degree of
Philosophiæ Doctor (PhD) of Grenoble University, France
Speciality: Physics of Condensed Matter and Radiation

Soutenue publiquement le **25 mai 2010**

Thèse dirigée par Dr Frédéric LANÇON et co-dirigée par Dr Yann-Michel NIQUET

Composition du jury

Messieurs	Christophe DELERUE	Rapporteur
	Frank GLAS	Rapporteur
	Michel GENDRY	Membre du jury
	Bruno DAUDIN	Membre du jury
	Yann-Michel NIQUET	Membre du jury
	Frédéric LANÇON	Membre du jury

Thèse préparée au sein du
CEA – Institut Nanosciences et Cryogénie (INAC) – L_Sim – GRENOBLE

Remerciements

Ce travail de thèse a été effectué au sein du Laboratoire de Simulation Atomistique (L_Sim) du Service de Physique des Matériaux et Microstructures de l'Institut Nanosciences et Cryogénie. A ce titre, je remercie Frédéric Lançon et Thierry Deutsch de m'avoir accueillie dans ce laboratoire.

J'adresse ma profonde reconnaissance à Yann-Michel Niquet qui a partagé avec moi ses savoirs et qui m'a encadrée et guidée au cours de ces trois années, ansi que pour la confiance accordée. Je suis reconnaisante pour tous les conseils et discussions qui ont largement contribué au succès de ce travail.

Je tiens à remercier Mr Christophe Delerue et Mr Frank Glas qui ont accepté d'être rapporteurs de cette thèse. Je remercie également Mr Michel Gendry et Mr Bruno Daudin d'avoir accepté de participer à ce jury.

Je remercie également tous les collègues du L_Sim avec qui j'ai partagé le quotidien : Pascal Pochet, Damien Caliste, Stephan Roche, Margaret Gabriel, Hector Mera, Eduardo Machado, Emmanuel Arras, Arpan Deb, Bhaarathi Natarajan, Mathieu Ospici, Cornelia Metzig, Martin Persson, Ivetta Slipukhina, Thomas Jourdan, Aurélien Lherbier, Luigi Genovese, Konstantin Rushchannskii, et Anders Bergman.

De même je voudrais remercier les collègues de l'équipe mixte CEA/CNRS/UJF "Nano-physique et Semiconducteurs", ainsi que ceux des différents laboratoires avec lesquels j'ai eu le plaisir de travailler : Bruno Daudin, Catherine Bougerol, Julien Renard, Bruno Gayral, Gabriel Tourbot, Rudeesun Songmuang, Joel Eymery, Diane Sam-Giao, Karine Hestroffer, Robert Koster, Vincent Favre-Nicolin, Francesca Mastropietro, Ana Cros, Rafael Mata, Olivier Landré et Hubert Renevier.

Pour finir, je remercie ma famille qui m'a toujours encouragée pour continuer dans cette voie: Ma mère Madgalena Mojica, mon père Adrian Camacho, mon frère Adrian Camacho Mojica, "les agradezco por estar siempre conmigo sobre todo en los momentos más difíciles".

Contents

French and spanish abstracts

Résumé en français / French abstract

Les nanofils sont des structures avec une taille latérale de l'ordre du nanomètre. Nous pouvons trouver des nanofils de différents matériaux, dont les semiconducteurs III-V, qui se distinguent par leurs applications potentielles dans les dispositifs optiques tels que les photo-détecteurs, diodes émettrices de lumière (LEDs) et lasers.

Les nanofils peuvent être été fabriqués par croissance avec la méthode Vapeur Liquide Solide (VLS). Les nanofils III-V peuvent également être réalisés sans catalyseur avec des méthodes comme l'épitaxie par jets moléculaires (MBE) ou la MOCVD ("Metal Organic Chemical Vapor Deposition"). Il est possible d'alterner les matériaux le long de l'axe de croissance des nanofils et de faire ainsi croître des "hétérostructures" de nanofils comprenant barrières tunnels et boîtes quantiques. Il est également possible de déposer une ou plusieurs "coquilles" autour du nanofil pour réaliser des hétérostructures radiales.

Ces hétérostructures de nanofils peuvent accomoder des désaccords de maille beaucoup plus importants que les hétérostructures planes conventionnelles. En effet, les nanofils de semiconducteurs peuvent relaxer efficacement les contraintes en déformant leur surface. L'épaisseur critique au delà de laquelle les dislocations apparaissent est donc d'autant plus grande que la section des fils est petite, ce qui permet de faire croître des hétérostructures originales.

Les systèmes qui constituent le sujet principal de ce thèse sont les hétérostructures de nanofils constituées de GaN et d'AlN. Ces matériaux cristallisent dans la structure wurtzite, où ils forment des liaisons ionocovalentes dans une maille hexagonale. Nous nous attacherons à modéliser leurs propriétés à l'échelle atomique, en lien avec des études expérimentales. Nous chercherons en particulier à affiner l'interprétation d'une expérience de spectroscopie optique où a été mis en évidence un fort "effet Stark confiné" dans ces hétérostructures, i.e. un décalage vers le rouge de la luminescence lié à la présence d'un champ électrique interne. Les phases wurtzite présentent en effet une polarisation électrique spontanée (pyroélectricité), qui est responsable de l'apparition de champs électriques importants. Ces expériences sont introduites dans le chapitre 1.

Les contraintes résiduelles dans ces hétérostructures ont tout d'abord modélisées avec un champ de forces de valence de type "Keating" (chapitre 2). L'énergie élastique dans ce modèle est la somme d'un terme radial, qui décrit le coût de l'allongement des liaisons avec

les premiers voisins, et d'un terme angulaire, qui décrit le coût de la modification des angles de liaisons. Deux constantes élastiques, α et β, sont associées respectivement à chacun de ces termes. Le modèle de Keating a été initialement développé pour des matériaux cubiques (zinc-blende) où toutes les liaisons sont équivalentes. Nous l'avons adapté à des structures wurtzites arbitraires où l'une des liaisons avec les quatre premiers voisins est plus longue que les autres. Nous avons établi les expressions reliant α et β aux constantes élastiques macroscopiques c_{ij}, qui nous ont permis ce calculer les valeurs de α et β pour GaN et AlN, et InN wurtzite.

Nous avons ensuite appliqué ce modèle à différentes hétérostructures GaN/AlN. Puisque le modèle de Keating ne considère que la relaxation élastique (aucune dislocation), la comparaison entre les positions atomiques obtenues par la simulation et les positions obtenues avec une méthode expérimentale telle que la microscopie peut suggérer la présence ou confirmer l'absence de dislocations dans un système. De fait, la comparaison entre les champs de contraintes théoriques et expérimentaux dans des hétérostructures GaN/AlN présentant une coquille d'AlN a permis de mettre en évidence la présence de dislocations dans la coquille. A l'inverse, dans des super-réseaux de nanofils GaN/AlN de rayon plus petit, l'accord entre la simulation et la diffraction de rayons X aussi bien que les images de TEM suggère une relaxation élastique parfaite du système.

Dans le chapitre 3, nous présentons les différentes approches possibles pour le calcul des propriétés électroniques et optiques des nanofils, en commençant par l'approximation de la masse effective. Celle-ci est une méthode de milieux continus qui peut être utilisée pour modéliser le voisinage du minimum de bande de conduction. Cette méthode reste la plus utilisée dans les matériaux semiconducteurs car elle permet souvent d'établir des expressions analytiques et de dégager des tendances. Toutefois, elle n'est pas suffisamment quantitative dans les milieux très confinés, et sa mise en oeuvre dans la bande de valence des matériaux wurtzite reste complexe. Nous introduisons ensuite la méthode des liaisons fortes, qui permet une description atomistique de la structure électronique des matériaux même très confinés. L'idée de cette méthode est de développer les fonctions d'ondes des électrons et des trous dans une base d'orbitales atomiques (s, p, d, ...) des différents atomes. Les interactions entre orbitales sont limitées aux premiers, seconds ou troisièmes voisins selon les modèles et sont ajustées pour reproduire la structure électronique des matériaux massifs, puis transférées aux nanostructures. Cette méthode a déjà été utilisée avec succès par le passé pour calculer la structure électronique de toutes sortes de nanostructures de semiconducteurs.

Nous décrivons ensuite la structure électronique de GaN et AlN massif dans les structures cubique et wurtzite. Nous montrons les similitudes et différences entre les deux phases. La structure électronique de la bande de valence est, en particulier, très complexe. Les matériaux cubiques présentent trois bandes de valence, dont deux, dégénérées en Γ (trous lourds et trous légers), sont séparées de la troisième ("split-off"/spin-orbite). La dégénérescence trous lourds/trous légers est levée par le champ cristallin dans la wurtzite, qui présente trois bandes de valence distinctes, appelées "A", "B", et "C", dont l'ordre dépend du matériau. Cet ordre est notamment différent dans GaN et AlN.

Nous décrivons ensuite un modèle pour la prise en compte de l'effet des contraintes en liaisons fortes. Ce modèle comprend une correction des termes "intrasites" qui lève la dégénérescence des orbitales p et d sous contrainte uniaxiale. Nous proposons une paramétrisation de ce modèle pour GaN et AlN.

Enfin, nous présentons une application des liaisons fortes à un système différent, celui des nanofils InAs/InP en phase cubique. Nous discutons en particulier l'effet des contraintes sur la hauteur des barrières d'InP dans des nanofils d'InAs.

Dans le chapitre 4, nous faisons une description détaillée du système GaN/AlN. Comme nous avons l'intention de comprendre les propriétés électroniques des insertions de GaN dans des nanofils d'AlN, nous discutons d'abord le confinement quantique dans deux situations limites : Puits quantiques de GaN/AlN, et fils de GaN purs. Nous décrivons ensuite les propriétés pyro- et piézoélectriques de ces matériaux. Comme les quatre premiers voisins d'un atome ne sont pas équivalents dans la structure wurtzite, le barycentre des anions et des cations ne coïncide pas dans la maille, ce qui entraîne l'apparition d'une polarisation électrique spontanée (pyroélectricité). Les contraintes, qui déplacent les cations par rapport aux anions, viennent ensuite modifier cette polarisation (piezoélectricité). Cette distribution de polarisation crée des champs électriques internes qui peuvent être très importants. Ils sont, en particulier, responsables de "l'effet Stark" dans les hétérostructures GaN/AlN : Le champ électrique sépare les électrons et les trous, ce qui entraîne un décalage vers le rouge des raies de luminescence, en deçà même de la bande interdite des matériaux massifs. Nous discutons cet effet dans les puits de GaN dans AlN. Nous montrons que le décalage vers le rouge augmente avec l'épaisseur du puits, et que la bande interdite s'annule dans des puits d'environ 5 nm d'épaisseur.

L'effet Stark a également été mis en évidence dans des hétérostructures de nanofils GaN/AlN, dans l'équipe NPSC de l'INAC. Le décalage vers le rouge mesuré est toutefois beaucoup plus petit que dans les puits et les boîtes quantiques de GaN. Ce sont ces expériences que nous nous efforcerons d'interpréter à la fin du chapitre 4 et dans le chapitre 5. Nous avons tout d'abord calculé les énergies de luminescence dans une approche "simple" qui ne tient compte que de la polarisation pyro- et piézoélectrique comme sources de champ électrique. Nous montrons que les champs électriques dans les fils devraient être comparables à ceux trouvés dans des hétérostructures planes, ce qui ne permet pas d'expliquer les résultats expérimentaux. Il manque donc dans cette approche des phénomènes d'écrantage qui réduisent l'amplitude du champ électrique.

Dans le chapitre 5, nous étudions les différents phénomènes qui écrantent le champ électrique dans ces hétérostructures. Nous démontrons que le champ électrique interne est capable de déplacer des charges dans le système. En particulier, il peut arracher des électrons aux états de surface occupés à l'extrémité des fils et les transférer sous l'hétérostructure GaN/AlN. Le gaz d'électrons ainsi formé réduit le champ électrique dans le système. Nous calculons de façon auto-cohérente le champ électrique écranté avec un modèle de Debye-Hückel, en incluant les états de surface qui peuvent capturer ou libérer des porteurs. Nous

obtenons alors un bon accord entre les énergies de luminescence calculées avec le modèle de liaisons fortes et les mesures expérimentales. Nous proposons également un modèle analytique approché pour aider la conception des hétérostructures GaN/AlN.

Resumen en español / Spanish abstract

Los nanohilos son estructuras con un tamaño lateral del orden del nanometro. Podemos encontrar nanohilos de distintos materiales, entre los cuales destacan los semiconductores III-V, los cuales se remarcan por sus aplicaciones en dispositivos ópticos como fotodetectores, diodos emisores de luz (LEDs) y lassers. Los primeros nanohilos se crearon con el método Vapor Líquido Sólido (VLS), el cuál utiliza oro como catalizador, los nanohilos III-V se crean actualmente utilizando métodos como el " Molecular Beam Epitaxy" (MBE) o el " Metal organic chemical vapeur depositon" (MOCVD), que pueden hacer crecer nanohilos sin catalizador. Los primeros sistemas similares a un modelo teórico simple como un potencial unidimensional, es decir, un pozo cuántico, se han creado utilizando heteroestructuras de nanohilos, las cuales crecen de manera epitaxial. Es posible crear heteroestructuras de dos tipos, axiales y radiales también llamados " core-shell" Uno de los aspectos interesantes de los nanofils comparado al material masivo es que la pequeña sección transversal permite una relajación lateral, permitiendo la combinación de los materiales con distintos parámetros de malla. Por otra parte esta diferencia en las parametradas de malla crea un estres cerca de la unión de dos materiales, donde el material con un mayor parámetro de malla está bajo compresión y el material con un más pequeño parámetro de malla está bajo tensión. Los sistemas, que son el tema principal de esta tesis, son las heteroestructuras de nanofils constituidas de GaN y AlN. Estos materiales cristalizan en la estructura wurtzita, y ellos formando enlaces ionocovalentes formando una estructura hexagonal. El estres presente en la heteroestructura se modelizaa utilizando el campo de fuerza de Valencia de Keating. En cuál la energía elástica por átomo se forma por dos términos cuando los átomos se desplazarán de su posición de equilibrio, el primero considera los cambios de distancia entre los primeros vecinos (bond stretching), el en segundo lugar considera el cambio en los ángulos formados entre los primeros vecinos (bond bending). En este modelo aparecen un par de constantes alfa y beta para bond stretching y bond bending respectivamente, estos constantes son ajustadas a cada material. La energía elástica obtenida con el modelo de Keating se compara a la energía elástica del modelo macroscópico donde aparecen el constante C11, C12 y C44, y las constantes apha y la beta son ajustada de manera que puedan reproducir las constantes macroscópicas. Este modelo inicialmente se creó para la estructura zicblenda y a continuación se adaptó a la estructura wurzita, nosotros la adaptamos a la estructura wurzite no ideal, la cual considera que la distancia entre primeros vecinos que son paralelos al eje c es mayor que las otras tres distancias entre vecinos, produciendo el tetrahedre formado por las enlaces no tenga en su centro un átomo. En ese caso la energía elástica por átomo se forma por dos términos bond stretching y dos términos bond bending, el para cada tipo de conexión, (los enlaces paralelos al eje c, y los enlaces no paralelos al eje c), y dos para cada tipo d' ángulo. Este modelo simple de dos constantes reproduce de manera razonable todas las constantes elásticas para GaN, AlN e InN wurtzita. Puesto que el modelo de Keating VFF considera solamente la relajación elástica (sin dislocaciones), la comparación entre las posiciones atómicas obtenidas por las simulaciones y las posiciones obtenidos por un método experimental como TEM puede sugerir la presencia o la ausencia de las dislocaciones en

un sistema. En el capítulo 2 presentamos la aplicación de modelo de Keating en los dos casos. Primero lugar discutimos de las inserciones de GaN en nanocolumnas de AlN, donde la diferencia entre las imágenes de TEM y las simulaciones indican la presencia de las dislocaciones. En segundo lugar, discutimos unas superredes de nanohilos de GaN/AlN con un radio más pequeño donde el acuerdo entre la simulación y la difracción de los rayos X así como las imágenes de TEM sugieren una relajación elástica perfecta del sistema. En el capítulo 3 examinamos la estructura electrónica del GaN y AlN, comenzando con la aproximacon más simple, la masa efectiva. Puede emplearse para que se modele la proximidad del minimo de la banda de conducción que se describe como una parábola, y el tiempo de cálculo es independiente del número d' átomos. Este modelo es eficaz, simple y preciso para el tratamiento de la banda de conducción en grandes sistemas. Con todo él falla en los sistemas muy confinados como nanocristales porque la aproximación parabólica no reproduce las bandas a alta energía. Mientras que el modelo de electrones casi libres es una representación razonablemente buena de la estructura elctronica de los metales simples, el método de enlaces fuertes proporciona una representación más fiel de los sistemas donde los iones se localizan en lps enlaces químicos de diferente grado de covalencia. La idea principal de este método es considerar una base de orbitales de atómicos y la interacción del uno con el otro que forma las órbitas moleculares. En le enfoque semiempirico de enlaces fuertes se hacen algunas aproximaciones habitualmente. Las interacciones se limitan a los primeros, segundos o en tercero vecinos más cercanos. Esto es justificado por el hecho de que las orbitales distantes tienen el translape despreciable. En este trabajo empleamos los modelos a primeros vecinos más cercanos. Las orbitales se asumen ortogonales. Los términos en a tres centros se desprecian en los Hopping términos. En el capítulo 3 se muestra la estructura de bandas para GaN y AlN para la estructura zicblend y wurtzita, utilizando el método de enlaces fuertes. Si hacemos un zoom de la estructura zicblende de GaN alrededor del punto gamma, podemos distinguir una banda de conducción y tres bandas de Valencia que se llaman los huecos pesados, huecos ligeros y banda de split off. El gap de GaN en esta estructura es directo mientras que le gap de AlN es indirecto. En la fase de wurtzita le gap de los dos materiales es directo. En wurtzita GaN y AlN, el fondo de la banda de conducción y la parte superior de las bandas de Valencia se encuentran en el punto gamma. La banda de conducción más baja es una combinación lineal d' orbital s mientras que la banda de valencia más alta es un comination lineal de orbitales p. Al final del capítulo 3 describen l' efecto del estres sobre la estructura de bandas y sel exemplifica con la modelización de estres en nanohilos de InAs e InP, utilizando el método de enlaces fuertes. En el capítulo 4 hacen una descripción detallada del sistema de GaN/AlN. Como tenemos la intención de incluir las propiedades electrónicas de las inserciones de GaN en nanohilos de AlN, discutimos primero el confinamiento cuántico en dos situaciones límite: Pozos cuánticos de GaN/AlN (t/R « 1) e hilos puros de GaN (t/R»1) , t siendo el grosor de la capa de GaN y el R el radio del hilo). GaN y AlN en la fase de wurtzita son propensos a la polarización eléctrica espontánea, ya que el distancia entre primeros vecinos más cercanos no son equivalentes, el baricentro de los aniones y los cationes no coinciden en la célula unidad. Esto conducen a l' existencia de una diferente densidad de cero de dipolo en el cristal (piroelectricidad). Le

estres desplaza los aniones con respecto a los cationes y redistribuirán la carga entre ellos, aumentando o disminuyendo por lo tanto esta densidad de dipolo (piezoelectricidad). Esta distribución de densidad de dipolo puede ser responsable de grandes campos eléctricos en heteroestructuras y dispositivos de GaN/AlN. Le efecto Stark es un fenómeno encontrado en las heteroestructuras bajo la presencia de un campo eléctrico. En este caso el campo es creado por los potenciales piroeléctrico y piezoeléctricos. La estructura electrónica de una heteroestructura es modificada debida al campo eléctrico. De esta forma obtendremos gaps ópticos más pequeños en presencia de este campo eléctrico, y disminuiremos el gap óptico de la heterosturctura cuando aumentamos la longitud de la inserción de GaN. Esto se manifiesta por un desplazamiento hacia el rojo en las medidas de fotoluminiscencia. Al final del capítulo 4 se muestran como le efecto Stark es muy sensible a la geometría del sistema, en elemplicifando con cálculos en hijos de AlN con inserciones de GaN. Se observó experimentalmente un fuerte desplasamiento hacia el rojo (debajo del gap en GaN masivo) para un mayor grosor de disco, una firma de l' efecto Stark cuántico confinado. Este desfase hacia el rojo es sin embargo más pequeño que el esperado en comparación con pozos de quantum de GaN/AlN. En el capitulo 5 se modelan las propiedades electroincas de las heterostructuras de nanohilos de GaN/AlN en un marco atomisctico de enlaces fuertes. Calculamos primero el estres con un método de campo de fuerza de valencia de Keating y luego calculamos el campo pyro y piezoeléctrico Explicamos el doblameinto de la banda con un enfoque semiclassique de Debye-Huckel, no haciendo ninguna pretensión con respecto al pining del nivel de Fermi, pero incluyendo una distribución de los estados de superficie que actúan como trampas o fuente de carreras. Probamos que el componente piezolectrico del campo puede ser reducido significativamente por la relajación eficaz de estres en la geometría del nanohilo, que la polarización espontánea y piezoeléctrica crean un gas d' electrones a la interface inferior de GaN/AlN y son probablemente bastante grande para crear un gas de huecos en la barrera superior d' AlN. Estos gases de electrón y de huecos reducen el campo eléctrico en los puntos cuánticos de GaN y reducen el desfase hacia el rojo. que para grosores cuidadosamente elegidos de punto cuántico y barrera el punto cuántico de GaN esta vacío al equilibrio, compatible con l' observación de transitan d' exciton y de biexiton.

Chapter 1

Introduction

1.1 The nanowires

The nanowires are structures with a lateral size of the order of few nanometers. Different kinds of nanowires have been designed; there are metallic nanowires (Ni, Au, Pt, ...), insulator nanowires (SiO, TiO, ...), and semiconductor nanowires. The semiconductors can be formed with elements of column IV, like Si, Ge, C, and with compounds of the III-V group. Here we can find nanowires of nitrides, like GaN, AlN, InN, nanowires of arsenides like InAs, AlAs, or nanowires of phosphides like InP, GaP, and AlP, for example. Ternary solid solutions have also been used for alloys like GaInN, GaAlN, etc...

In this work, we study the properties of semiconductor nanowires – mainly III-V semiconductors – with a special focus on GaN/AlN systems. This latter system crystallizes in the wurtzite structure, which exhibits, in particular, spontaneous (pyroelectric) polarization. When a stress is applied, it also shows piezoelectricity. Spontaneous polarization and piezoelectricity generate large internal electric fields which modify the electronic and optical properties of the system.

The nanowires can be homogeneous or heterogeneous (commonly known as heterostructures) with, in this latter case, a radial structure (figure 1.1) or an axial structure (figure 1.2). The work presented in this thesis is focused on such heterostructures.

1.2 Application of nanowires

The nanowires have become structures of great interest due to their multiple applications in:

Electronic devices (1), for instance field-effect transistors.
Bioelectronic, **bio-chemical sensors** (2) like gas or humidity sensors (3).
Solar cells (4).
Thermoelectricity (5).
Optoelectronic devices (6) like photodetectors, and light-emitting diodes (7) and lasers.
Let us now discuss some examples of these applications.

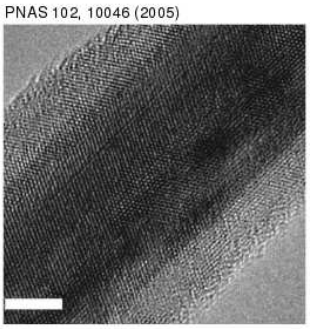

Figure 1.1: Radial heterostructure - Transmission electron microscopy (TEM) image of an "core-shell" Si-Ge nanowire [from reference (8)].

The efficient radiative recombination in III-V semiconductors has permitted the development of light-emitting devices that efficiently convert electrical energy into incoherent light. This has a growing number of rather diversified applications, like displays, lighting, traffic signs and signals, light surfaces for accelerated photosynthesis and medicine for diagnosis (10).

Much research has been done to develop high brightness blue-light-emitting diodes to be used in full colour displays and indicators. For these purposes, II-VI materials (such as ZnSe and SiC) and III-V nitride semiconductors have recently been investigated.

In 1993, Nakamura showed that it is possible to create blue light-emitting diodes from InGaN/AlGaN heterostructures (7). The high crystallographic quality of III-V nanowires is of particular interest since it potentially provides a solution for overcoming the problems inherent to the high density of dislocations usually found in bi-dimensional (2D) layers of this material. As a matter of fact nitride nanowires can be viewed as a juxtaposition of non-coalescent grains, which leads to the suppression of threading edge dislocations formed due to the coalescence of adjacent grains in the usual growth conditions of 2D layer.

It has been shown by various groups that GaN nanowires, grown without catalyst by molecular beam epitaxy, are high quality materials exhibiting remarkable optical properties as compared to those made of standard 2D layers. As a practical consequence of these excellent optical properties, it has been shown that nitride wire-like heterostructures present a potential interest for the realization of efficient light emitting devices (LED's) in the visible and UV ranges.

1.3 Growth of nanowires

The first wires were developed in the first half of the 60's at the Bell telephone laboratories, using the VLS (vapor-liquid-solid) technique (11).

In this technique, droplets of liquid gold are deposited on a substrate, for instance Si, and they are heated until they turn into small droplets of Au-Si. Next, these droplets are exposed

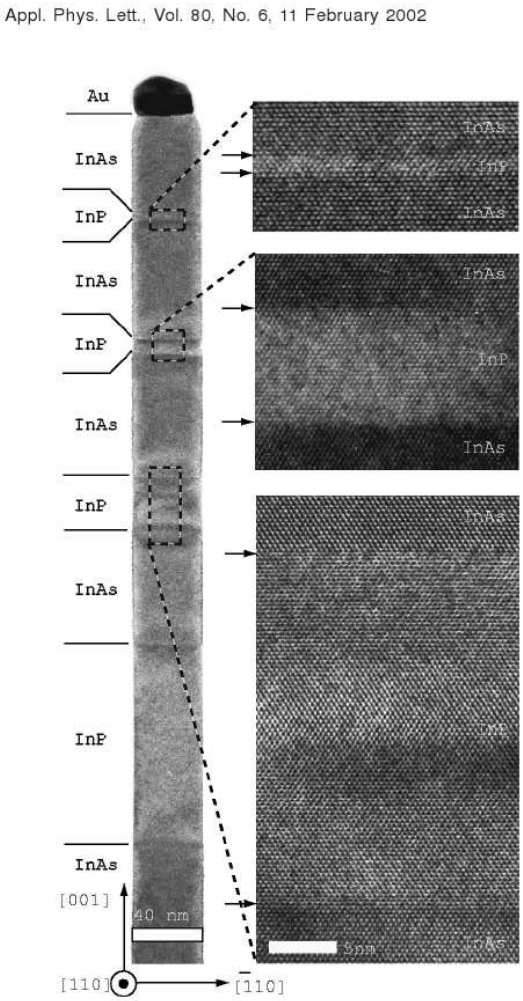

Figure 1.2: Axial heterostructure - Transmission electron microscopy (TEM) image of an InAs nanowire of 40 nm diameter containing four InP barriers [from reference (9)].

to an atmosphere of $SiCl_4$ and H_2 (vapor). The droplets act as (liquid) chemical catalysts adsorbing the silicon from the gas until supersaturation occurs. At that point, the Si atoms condense and crystallize (solid) between the substrate and the droplets. The final diameter of the wires is mainly determined by the initial diameter of the droplets, while the length of the nanowires increases until the growth is stopped.

This technique has been improved in 1998 with a reduction of the size of the droplets by using the Laser Ablation Method (12). This technique leads to nanowires of homogeneous diameter in the nanometric scale.

As for III-V nanowires, they can be grown with or without catalysts. There are two main techniques, which will be described below: the Molecular-Beam Epitaxy (MBE) and the Metal-Organic Chemical Vapour Deposition (MOCVD).

1.3.1 Molecular Beam Epitaxy (MBE)

In this technique, performed under ultra high vacuum conditions, pure elements are evaporated from source cells onto a heated substrate, where they condensate. At low deposition rates, the growth process can be monitored and a crystal may be built one atomic layer at a time (13). In favorable cases (small lattice mismatch), the resultant layer is epitaxial to the substrate. Nitride semiconductors are usually grown with "plasma-assisted" MBE where active nitrogen is produced by a plasma source.

Nitride nanowires can be grown with MBE without catalysts (14). The nanowires nucleate from small GaN islands spontaneously formed on the substrate by Stranski-Krastanov or Volmer-Weber growth. As the "vertical" growth along $[0001]$ is much faster than the "lateral" growth perpendicular to $[0001]$, these islands indeed turn into elongated, nanowire-like structures.

1.3.2 Metal-Organic Chemical Vapor Deposition (MOCVD)

In the MOCVD, gazeous precursors of the semiconductor elements are mixed with transport gases and injected into a reactor. These precursors are pyrolysed onto a heated substrate and react with the surface. At variance with MBE, which is mostly a physical deposition in ultra-high vacuum conditions, MOCVD involves complex gas phase and surface chemical reactions (10), and is performed at higher gas pressures (typically 800 mbar for GaN). Metal-organic molecules such as trimethyl-gallium or trimethyl-aluminum are used as precursors for Gallium and Aluminium, while ammonia (NH_3) is used as a source for nitrogen.

Catalyst-free GaN nanowires have been grown with MOCVD on a sapphire substrate covered with a thin dielectric layer (15). Holes opened in the dielectric layer served as a mask for the growth of the nanowires.

1.4 Heterostructures

1.4.1 Definition

A heterojunction is formed when a layer of material “A” is deposited onto a layer of material “B”. A heterostructure is an ensemble of such heterojunctions. If a narrow bandgap material “A” is sandwiched between two layers of a wider bandgap material “B”, as illustrated in fig 1.3, it forms a quantum well (17). The carriers (electrons, holes) injected in the structure tend to be collected by the quantum well where they can, for example, recombine by emitting photons. If, on the opposite, a large bandgap material “A” is sandwiched between two layers of a narrow bandgap material “B”, it forms a tunneling barrier, which can be used to control the flow of carriers.

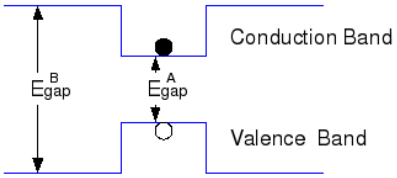

Figure 1.3: Heterostructure - Band structure of a heterostructure.

The design of heterostructures is limited by the lattice mismatch between the different materials. A layer “A” deposited on a thick layer “B” with a different lattice parameter will be strained and accumulate elastic energy. When the thickness of layer “A” reaches a critical thickness h_c, the strains are relieved by the formation of misfit dislocations or by a transition to a Stranski-Krastanov growth mode (20).

1.4.2 Axial and radial nanowire heterostructures

In nanowires, it is possible to grow two kinds of heterostructures: axial heterostructures (18), where the layers are stacked along the growth axis, as in figure 1.2, and radial heterostructures (19), also known as “core-shell” structures (see figure 1.1).

To create axial heterostructures, the reactants are switched once a given layer reaches the expected thickness. Changes in reactants are repeated to generate the desired heterostructure, as illustrated in figure 1.4. The sharpness of the interfaces depends on the actual growth mechanism (e.g., the catalyst might need to be purged in the VLS growth). Axial nanowire heterostructures resemble planar heterostructures, but with finite lateral size. As discussed in the next paragraph, this enhances strain relaxation and increases the critical thickness. If the radius of the nanowire and thickness of the layers can be made small enough, quantum dot-like structures, confined in all three directions of space, can be inserted in the nanowire.

The possibility to control the number and position of the quantum dots embedded in axial heterostructures is one important advantage of nanowires with respect to quantum dots obtained by Stranski-Krastanow growth (20).

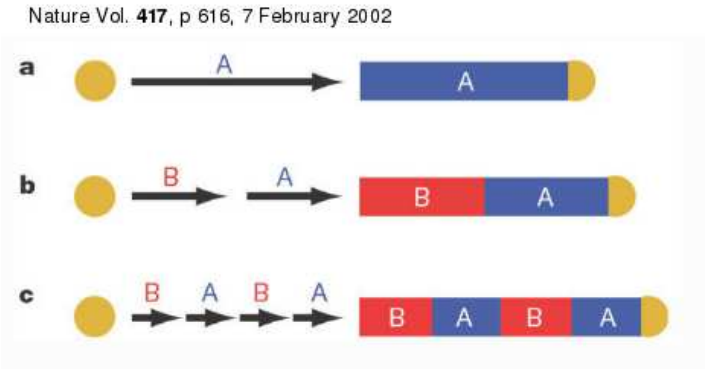

Figure 1.4: Axial heterostructure - **a)** Nanowire growth using reactant A. **b)** Switch from reactant A to reactant B and formation of the heterostructure. **c)** Formation of a sequence of crystalline layers by changing the reactants.

To create core-shell heterostructures, a complete homogeneous nanowire is grown first. The growth conditions are then changed so that the growth does not selectively takes place in the catalyst or in specific directions, and the reactants are switched. If this switch of reactants is repeated, it is even possible to grow a multi-shell structure, as shown in figure 1.5.

1.4.3 Strains in heterostructures

One of the interesting aspects of nanowire compared to conventional planar heterostructures is their ability to relax strains. Indeed, the nanowires can distort their free surface to relieve internal misift strains at the interfaces between heterolayers. As a consequence, the nanowires can accomodate much larger lattice mismatches than 2D heterostructures (21).

As explained above, strain relaxation in 2D heterostructures occurs by the formation of dislocations beyond a critical thickness h_c which depends on the lattice mismatch between the materials. These dislocations are extended defects which degrade the electrical and optical properties of the heterostructures, and should therefore be avoided as far as possible. In nanowire heterostructures, the critical thickness increases with decreasing wire radius as the free surfaces allow more efficient elastic strain relaxation. For a given lattice mismatch, it has even been predicted that the critical thickness becomes infinite below a critical radius R_c (22; 23), allowing the growth of arbitrary coherent heterostructures with can not be achieved with planar technologies, such as the heterostructure of figure 1.2.

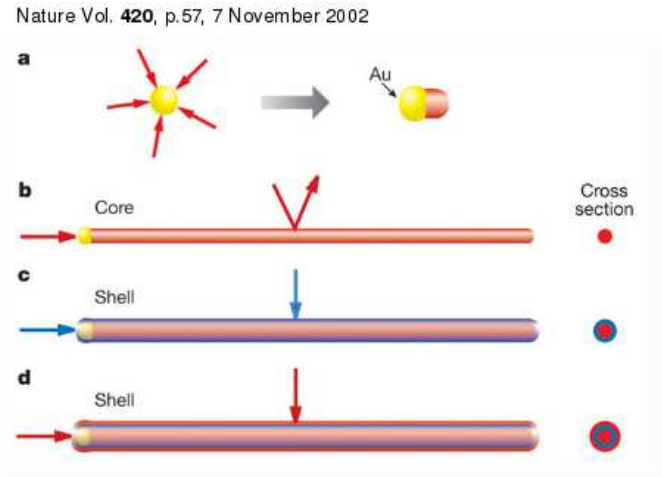

Figure 1.5: Core-shell heterostructure. - **a)** Nanowire grown using reactant A. **b)** Switch form reactant A to reactant B, formation of a shell around the initial wire. **c)** Formation of a multi-shell structure.

1.5 Nitride nanowires

The systems, which are the main subject matter of this thesis, are the nanowire heterostructures made of GaN and AlN. Both materials form ionocovalent bonds and crystallize in the wurtzite structure. We will describe this hexagonal structure in detail in chapter 2.

One of the specifics of wurtzite materials is the existence of large internal electric fields. These built-in electric fields are due to the existence of a spontaneous polarization in the system (pyroelectricity). The bonds between anions and cations are not, indeed, equivalent in the wurtzite structure, so that the unit cell exhibits a non-zero electric dipole. This dipole is further affected by strains (piezoelectricity). We will investigate the polarization and electric field in nitride nanowires in detail in chapters 4 and 5. For now, we discuss experimental data clearly showing the existence of a large electric field in GaN/AlN nanowire heterostructures (24). The detailed interpretation of these experimental results will be the focus of chapter 5.

The system consists of GaN quantum disks between two AlN barriers, on top of 30 nm diameter GaN pillars (see figure 1.6). These wires were grown by plasma-assisted MBE under nitrogen-rich conditions (24). The thickness of the quantum disks ranges from 1 to 4 nm. J. Renard *et al.* (24) have measured the photoluminescence spectra obtained by exciting the samples with a doubled argon laser emitting at 244 nm (see figure 1.7). In such a photoluminescence experiment, electrons are transferred by the laser from the valence band to the conduction band, leaving holes in the former, *i.e.* electron-hole pairs are generated. The electrons and holes thermalize to the lowest conduction band and higher valence band states, where they can recombine by emitting photons. The energy of the emitted photons is therefore comparable to the bandgap of the material (up to a so called *excitonic* correction

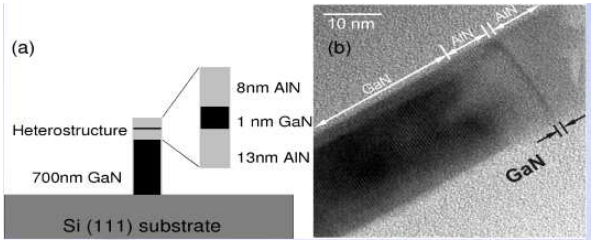

Figure 1.6: The system - a) GaN quantum disks embedded in AlN nanowires, b) HRTEM image from reference (24).

due to the attractive Coulomb interaction between the electron and the hole). The intensity of the luminescence depends on the overlap between the electron and hole wave functions, and on the competition with non-radiative recombination channels such as impurities.

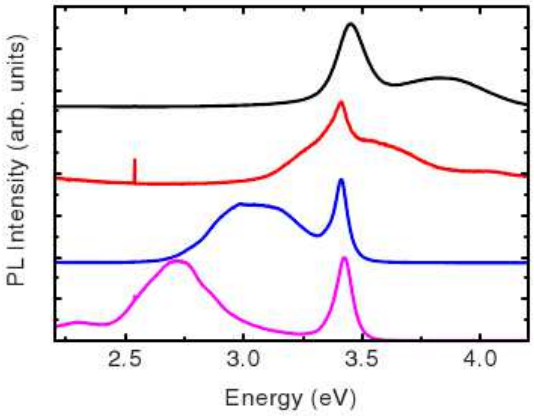

Figure 1.7: Photoluminescence spectra - Room-temperature macrophotoluminescence spectra of ensembles of GaN/AlN axial nanowire heterostructures containing single GaN quantum dots. The different curves correspond to increasing GaN insertion thickness from $\sim$ 1 nm to $\sim$ 4 nm.

The signal around 3.4-3.45 eV comes from electron-hole pairs recombining in the GaN base of the nanowires. The other peak is attributed to the GaN insertions. It is broadened by the dispersion of the size of the disks. The position of this peak monotonously decreases as a function of the disk thickness. In particular, in the thickest insertions, the photoluminescence occurs around 2.7 eV, hence at energies well below the band gap of bulk GaN. This redshift is due to the electric field in the insertion, which separates the electrons from the holes ("Stark effect"). This experiment will be analyzed in detail in chapters 4 and 5.

1.6 Conclusion and outline of this thesis

As shown in this introduction, nanowires can be grown with various shapes and compositions, and provide new opportunities to explore the physics of one-dimensional systems. GaN/AlN nanowire heterostructures show, in particular, interesting optical properties such as a strong Stark effect.

In this thesis, we model the structural and electronic properties of nitride nanowires, with a particular focus on the Stark effect experiments of Ref. (24). We use, for that purpose, atomistic methods, which provide a description of the nanowires at the atomic scale. In chapter 2, we discuss the structural properties of GaN/AlN nanowire heterostructures. We introduce the zinc-blende and wurtzite crystal structures encountered in these materials, and derive a valence force field model for the wurtzite phase. This valence force field allows the calculation of the atomic positions in strained nanowire heterostructures, assuming coherent growth (no dislocations). We compare the predictions of this model with various TEM and X-Ray experiments. In chapter 3, we introduce the tight-binding method for the electronic structure. We discuss, in particular, the effects of strains on the band structure of nitrides. In chapter 4, we review the properties of GaN/AlN heterostructures. We discuss the spontaneous polarization, piezoelectricity and built-in electric fields. We attempt simple calculations of the Stark effect in GaN/AlN nanowire heterostructures, which do not, however, match the experiments. These calculations actually point to the importance of the screening of the electric field by, e.g., charged surface defects. Finally, in chapter 5, we make a complete simulation of the electrostatics of these nanowires, including such complex screening effects. We get a much better agreement with the experiment, and are able to provide a detailed interpretation of the physics of these heterostructures.

Chapter 2

Structural properties of nitride nanostructures

2.1 Introduction

Strains have significant effects on the electronic and optical properties of lattice mismatched semi-conductor heterostructures such as quantum dots or nanowires. They indeed shift the conduction and valence band edges (26) and might give rise to piezoelectric fields (27) which tend to separate the electrons from the holes (28; 29). In inhomogeneous systems, the strains $\varepsilon_{\alpha\beta}$ can be conveniently computed with continuum elasticity theory (30), which is believed to hold down to nanometer-size systems (31). These strains can then be used directly as input for electronic structure calculations within the effective mass or $\mathbf{k}\cdot\mathbf{p}$ approximations (32; 33), which are also continuous medium theories. The strains $\varepsilon_{\alpha\beta}$ do not, however, provide enough information for atomistic electronic structure methods such as tight-binding (34; 35) or pseudopotentials (36; 37), which need atomic positions as input. Indeed, the atomic positions can hardly be reconstructed from the strains, whose analytic structure is very complex around, e.g., surfaces and interfaces, and which do not characterize the internal strains (38) within the unit cell (i.e., the displacement of one sublattice with respect to an other). Therefore, the atomic positions used as input for such methods are usually computed with semi-empirical force fields such as Keating's Valence Force Field (VFF) (39), Tersoff (40), or Stillinger-Weber potentials (41).

There is a a clear trade-off between the range and complexity of these force fields and their transferability. In the elastic limit (no plastic relaxation), Keating's VFF model provides a good balance between accuracy and efficiency. This first nearest neighbor force field has originally been developed for diamond and zinc-blende materials (39). It gives an excellent account of the elastic properties of silicon and germanium, and a reasonable description of those of III-V materials. The latter can be improved with the introduction of long range interactions arising from the charge transfer between anions and cations (42), at the expense of a larger computational cost. In principle, Keating's model can also be applied to wurtzite materials. To our knowledge, the relations between the macroscopic elastic constants c_{ij} and Keating's bond-bending and bond-stretching constants have only been established for ideal wurtzite materials with equal bond lengths and angles (43; 44).

In this chapter we introduce the two main polytypes encountered in III-V materials, the zinc-blende (ZB) and the wurtzite (WZ) structures. We then present the application of Keating's Valence Force Field (VFF) model to arbitrary wurtzite materials. We finally discus the application of the model to GaN/AlN core-shell and axial nanowire heterostructures.

2.2 The III-V semiconductor structures

The III-V semiconductor crystals form ionocovalent bindings, being tretravalent with a sp^3 hybridisation. These tetrahedrons can be organized in two types of lattice structures: the zinc-blende and the wurtzite.

In the case of the zinc-blende there are two sublattices one for cations and another one for anions. In the case of the wurtzite structure there are four sublattices which can also be considered as two hexagonal compact sublattices. In both cases, one cation of one sublattice is surrounded by four anions of the another sublattice, and one anion is surrounded by four cations forming such tetrahedrons.

2.2.1 The Zinc-Blende structure

The arrangement of atoms in the Zinc-Blende structure can be described as two cubic face centered structures shifted one with respect to the other by a distance of $a\sqrt{3}/4$ in the [111] direction. One sublattice is occupied by anions and the other one by cations. It can also be considered as a cubic diamond structure but alternating two different ions.

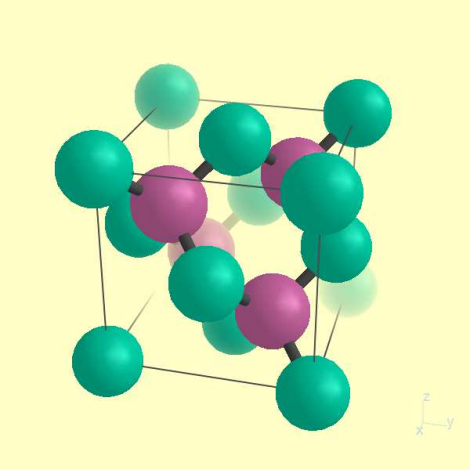

Figure 2.1: The Zinc-Blende cubic cell. The atoms of one sublattice are in red, the atoms of the other in green. -

We show the conventional cubic cell in the figure. 2.1, where the [111] direction goes along the diagonal of the cube from the bottom left corner to the top right corner. The

primitive cell is formed by one cation and one anion, and the primitive translation vectors are:

$$\begin{aligned} \mathbf{a} &= \frac{1}{2}a(0,1,1) \\ \mathbf{b} &= \frac{1}{2}a(1,0,1) \\ \mathbf{c} &= \frac{1}{2}a(1,1,0) \end{aligned} \tag{2.1}$$

The unit-cell positions are

$$\begin{aligned} \mathbf{R}_1 &= \mathbf{0} \\ \mathbf{R}_2 &= \frac{1}{2}\mathbf{a}+\frac{1}{2}\mathbf{b}+\frac{1}{2}\mathbf{c}, \end{aligned} \tag{2.2}$$

where a is the lattice constant.

2.2.2 The Wurtzite structure

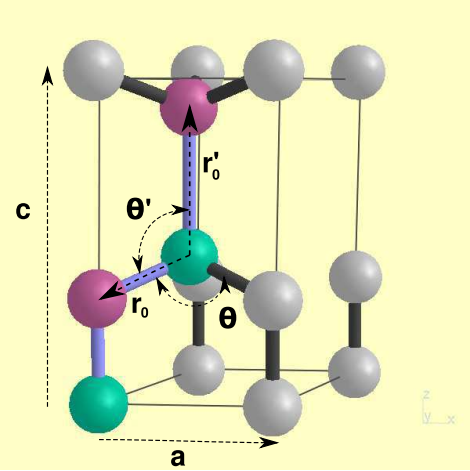

Figure 2.2: The Wurtzite unit cell - Three unit cells form an hexagon. The atoms of one sublattice are in red, the atoms of the other in green.

The wurtzite structure can be described as two identical hexagonal close-packed sublattices, shifted along the c axis by cu. The wurtzite unit cell is shown in figure 2.2.

The lattice vectors are:

$$\begin{aligned} \mathbf{a} &= a(1,0,0) \\ \mathbf{b} &= a(1,\sqrt{3},0)/2 \\ \mathbf{c} &= c(0,0,1), \end{aligned} \tag{2.3}$$

and the unit-cell positions are

$$\begin{aligned}\mathbf{R}_1 &= \mathbf{0}\\ \mathbf{R}_2 &= u\mathbf{c}\\ \mathbf{R}_3 &= \frac{1}{3}\mathbf{a}+\frac{1}{3}\mathbf{b}+\frac{1}{2}\mathbf{c}\\ \mathbf{R}_4 &= \frac{1}{3}\mathbf{a}+\frac{1}{3}\mathbf{b}+\left(u+\frac{1}{2}\right)\mathbf{c}\,.\end{aligned} \tag{2.4}$$

Sublattice 1 and 3 are occupied by the cations while sublatice 2 and 4 are occupied by anions. At variance with the zinc-blende structure, the four nearest neighbors bonds are not equivalent in the wurtzite structure. The bonds oriented along c indeed have a different length (r_0') than the other bonds (r_0) and make different bond angles. We will see in chapter 4 that this is responsible for the spontaneous polarization of the material and the existence of large internal electric fields. Only in the particular case $u=\frac{3}{8}$ and $c=a\sqrt{\frac{8}{3}}$ are the bonds equivalent ("ideal wurtzite material")

2.3 The Valence Force Field model of Keating

The VFF Model has been introduced by P. N. Keating in 1966 (39). It gives the forces induced on neighboring atoms when one atom moves from its equilibrium position in a tetrahedrally-bonded solid. These forces gives to the solids their rigidity against compressive, tensile, and shear stresses.

2.3.1 Keating's model for the Zinc-Blende structure

The valence force field model (VFF) of Keating has originally been introduced for diamond and zinc-blende materials. The elastic energy per atom reads in this approximation:

$$U_i=\frac{3\alpha}{16r_0^2}\sum_{j=1}^{4}\left(\mathbf{r}_{ij}^2-r_0^2\right)^2+\frac{3\beta}{8r_0^2}\sum_{j=1}^{4}\sum_{k>j}^{4}\left(\mathbf{r}_{ij}\cdot\mathbf{r}_{ik}+\frac{r_0^2}{3}\right)^2, \tag{2.5}$$

where $\mathbf{r}_{ij}$ is the vector from a given atom i to one of its four nearest neighbors j. The first term accounts for the changes in bond lengths, while the second term mostly accounts for the changes in bond angles. The macroscopic elastic constants c_{11}, c_{12} and c_{44} are related to the "bond-stretching" constant α, "bond-bending" constant β and equilibrium bond length $r_0=a\sqrt{3}/4$ by comparing equation 2.5 with the energy in the continuous elasticity theory

for a cubic structure (45);

$$c_{11} = \frac{\alpha+3\beta}{a} \tag{2.6a}$$

$$c_{12} = \frac{\alpha-\beta}{a} \tag{2.6b}$$

$$c_{44} = \frac{4\alpha\beta}{a(\alpha+\beta)}. \tag{2.6c}$$

Note that the c_{ij}'s are not independent and fulfill the relation $2c_{44}(c_{11}+c_{12}) = (c_{11}-c_{12})(c_{11}+3c_{12})$. This relation is much better satisfied in group IV diamond like materials than in III-V or II-VI ion-covalent materials where interactions are longer-ranged (42). It is nonetheless possible to achieve a reasonable description of the elasticity of most semiconductor materials in the above approximation.

2.3.2 Keating's model for the non-ideal Wurtzite structure

We can therefore generalize Keating's first nearest neighbor valence force field model to the wurtzite materials in the following way:

$$\begin{aligned} U_i &= \frac{3\alpha}{16r_0^2}\sum_{j=1}^{3}\left(\mathbf{r}_{ij}^2 - r_0^2\right)^2 + \frac{3\alpha'}{16r_0'^2}\left(\mathbf{r}_{i4}^2 - r_0'^2\right)^2 \\ &+ \frac{3\beta}{8r_0^2}\sum_{j=1}^{3}\sum_{k>j}^{3}\left(\mathbf{r}_{ij}\cdot\mathbf{r}_{ik} - r_0^2\cos\theta_0\right)^2 \\ &+ \frac{3\beta'}{8r_0r_0'}\sum_{k=1}^{3}\left(\mathbf{r}_{i4}\cdot\mathbf{r}_{ik} - r_0r_0'\cos\theta_0'\right)^2 \end{aligned} \tag{2.7}$$

where the b' bond of atom i is assumed to be $j=4$. For the sake of generality, we have introduced two bond stretching constants α and α' for the b and b' bonds, as well as two bond bending constants β and β'. It is easily verified that in the unstained but non-ideal wurtzite lattice, the elastic energy is minimum and zero.

r_0', r_0, $\cos\theta_0'$ and $\cos\theta_0$ (see figure 2.2) can easily be related to the structural parameters a, c and u:

$$r_0' = cu \tag{2.8a}$$

$$r_0 = \frac{\sqrt{3c^2v^2+4a^2}}{2\sqrt{3}} \tag{2.8b}$$

$$\cos\theta_0' = \frac{-\sqrt{3}cv}{\sqrt{3c^2v^2+4a^2}} \tag{2.8c}$$

$$\cos\theta_0 = \frac{3c^2v^2-2a^2}{3c^2v^2+4a^2} = \frac{3\cos^2\theta_0'-1}{2}, \tag{2.8d}$$

where $v = 1-2u$. Note that $\cos\theta_0' = \cos\theta_0 = -1/3$ in an ideal wurtzite material.

We shall now relate the macroscopic elastic constants c_{ij} of the material to the microscopic constants α, α', β and β'. To this end (39), we will identify the second-order development of equation (2.7) as a function of strains to the macroscopic elastic energy of the unit cell. Under homogeneous strain, the lattice vectors and unit-cell positions transform as:

$$\begin{aligned} \mathbf{a}' &= \hat{T}\mathbf{a}; \mathbf{b}' = \hat{T}\mathbf{b}; \mathbf{c}' = \hat{T}\mathbf{c} && \text{(2.9a)} \\ \mathbf{R}'_1 &= \hat{T}\mathbf{R}_1 \\ \mathbf{R}'_2 &= \hat{T}\mathbf{R}_2 + \mathbf{t}' \\ \mathbf{R}'_3 &= \hat{T}\mathbf{R}_3 + \mathbf{t} \\ \mathbf{R}'_4 &= \hat{T}\mathbf{R}_4 + \mathbf{t} + \mathbf{t}', && \text{(2.9b)} \end{aligned}$$

where $\hat{T} = \hat{1} + \hat{\varepsilon}$ and:

$$\hat{\varepsilon} = \begin{bmatrix} \varepsilon_{xx} & \varepsilon_{xy} & \varepsilon_{xz} \\ \varepsilon_{xy} & \varepsilon_{yy} & \varepsilon_{yz} \\ \varepsilon_{xz} & \varepsilon_{yz} & \varepsilon_{zz} \end{bmatrix} \tag{2.10}$$

is the strain tensor. $\mathbf{t} = (t_1, t_2, t_3)$ and $\mathbf{t}' = (t'_1, t'_2, t'_3)$ define rigid translations of the different sublattices (internal strains) that might be allowed by the reduced symmetry. We next introduce Eqs. (2.9) into equation (2.7), sum U_i over the four unit cell positions, expand the VFF energy to second order in ε_{ij}, t_i, and t'_i, then minimize the resulting expression with respect to the t_i and t'_i. We finally identify the VFF energy of the unit cell with the macroscopic elastic energy:

$$\begin{aligned} U &= \Omega \Big\{ \frac{1}{2} C_{11} \left(\varepsilon_{xx}^2 + \varepsilon_{yy}^2\right) + \frac{1}{2} C_{33} \left(\varepsilon_{zz}^2\right) + C_{12} \left(\varepsilon_{xx}\varepsilon_{yy}\right) + \\ & \quad C_{13} \left(\varepsilon_{xx}\varepsilon_{zz} + \varepsilon_{yy}\varepsilon_{zz}\right) + 2C_{44} \left(\varepsilon_{xz}^2 + \varepsilon_{yz}^2\right) + \left(C_{11} - C_{12}\right) \left(\varepsilon_{xy}^2\right) \Big\} \end{aligned} \tag{2.11}$$

where Ω is the volume of the unit cell. We get:

$$c_{11} = \frac{a^2}{2\sqrt{3}c} \frac{\left(4A^2 + 13AB + B^2\right)\left(8A'u^2 + 3B'w^2\right) + 162AB\left(A+B\right)v^2}{\left(2A+B\right)\left[6\left(A+2B\right)v^2 + 8A'u^2 + 3B'\left(1-8uv\right)\right]} \tag{2.12a}$$

$$c_{33} = \frac{3\sqrt{3}c^3}{4a^2} \frac{\left[\left(A+2B\right)\left(8A'u^2v^2 + 3B'v^4\right) + 16A'B'u^2\right]}{6\left(A+2B\right)v^2 + 8A'u^2 + 3B'\left(1-8uv\right)} \tag{2.12b}$$

$$c_{12} = \frac{a^2}{2\sqrt{3}c} \frac{\left(A-B\right)\left[\left(4A-B\right)\left(8A'u^2 + 3B'w^2\right) + 54ABv^2\right]}{\left(2A+B\right)\left[6\left(A+2B\right)v^2 + 8A'u^2 + 3B'\left(1-8uv\right)\right]} \tag{2.12c}$$

$$c_{13} = \frac{\sqrt{3}c}{2} \frac{\left(A-B\right)\left(8A'u^2 + 3B'vw\right)v}{6\left(A+2B\right)v^2 + 8A'u^2 + 3B'\left(1-8uv\right)} \tag{2.12d}$$

$$c_{44} = \frac{\sqrt{3}c}{4} \frac{\left(2A+B\right)B'}{\left(2A+B+B'\right)} \tag{2.12e}$$

$$c_{66} = \frac{c_{11} - c_{12}}{2}, \tag{2.12f}$$

where $A = \alpha/r_0^2$, $A' = \alpha'/r_0'^2$, $B = \beta/r_0^2$, $B' = \beta'/(r_0 r'_0)$, and $w = 1 - 4u$. The internal

translations which minimize the elastic energy moreover read:

$$\mathbf{t} = -a\xi\left(\varepsilon_{xy}, \frac{\varepsilon_{xx}-\varepsilon_{yy}}{2}, 0\right) \tag{2.13a}$$

$$\mathbf{t}' = c\left(\zeta_1\varepsilon_{xz}, \zeta_1\varepsilon_{yz}, \zeta_2\left(\varepsilon_{xx}+\varepsilon_{yy}\right)-\zeta_2'\varepsilon_{zz}\right), \tag{2.13b}$$

with internal strain parameters:

$$\xi = \frac{-2}{\sqrt{3}}\frac{A-B}{2A+B} \tag{2.14a}$$

$$\zeta_1 = \frac{Aw+Bv-2B'u}{2A+B+B'} \tag{2.14b}$$

$$\zeta_2 = \frac{2a^2}{c^2}\frac{(A-B)v}{6Av^2+8A'u^2+12Bv^2+3B'w^2} \tag{2.14c}$$

$$\zeta_2' = \frac{-3Av^3+8A'u^3-6v\left(Bv^2+B'wu\right)}{6Av^2+8A'u^2+12Bv^2+3B'w^2}. \tag{2.14d}$$

Note that we could have introduced two different sets of bond-bending constants for the anions and cations but that only the average would have appeared in the above expressions.

2.3.3 Keating's model for the ideal Wurtzite structure

Keating's VFF model can be readily applied to *ideal* wurtzite materials (with lattice parameters $c = a\sqrt{8/3}$ and $u = 3/8$) where all nearest neighbor bond lengths and angles are equal. As we use a first nearest neighbor model the expression for the Keating VFF is the same as the zinc-blende structure.

The elastic constants c_{11}, c_{33}, c_{12}, c_{44} and c_{66}, and internal strain parameters then read (43; 44):

$$c_{11} = \frac{\sqrt{3}}{12r_0}\frac{1}{2\alpha+\beta}\frac{1}{\alpha+\beta}\left(6\alpha^3+\beta^3+37\alpha^2\beta+28\alpha\beta^2\right) \tag{2.15a}$$

$$c_{33} = \frac{\sqrt{3}}{4r_0}\frac{1}{\alpha+\beta}\left(3\alpha^2+\beta^2+20\alpha\beta\right) \tag{2.15b}$$

$$c_{12} = \frac{\sqrt{3}}{12r_0}\frac{1}{2\alpha+\beta}\frac{\alpha-\beta}{\alpha+\beta}\left(6\alpha^2-\beta^2+7\alpha\beta\right) \tag{2.15c}$$

$$c_{13} = \frac{\sqrt{3}}{12r_0}\frac{\alpha-\beta}{\alpha+\beta}\left(3\alpha-\beta\right) \tag{2.15d}$$

$$c_{44} = \frac{\sqrt{3}}{3r_0}\frac{\beta}{\alpha+\beta}\left(2\alpha+\beta\right) \tag{2.15e}$$

$$c_{66} = \frac{c_{11}-c_{12}}{2} \tag{2.15f}$$

$$\tag{2.15g}$$

$$\xi = \frac{2}{\sqrt{3}}\frac{\alpha-\beta}{2\alpha+\beta} \tag{2.15h}$$

$$\zeta = \frac{\alpha-\beta}{4(\alpha+\beta)} \tag{2.15i}$$

where $r_0 = 3c/8 = a\sqrt{3/8}$ is the equilibrium bond length.

2.3.4 GaN, AlN and InN elastic constants

As an illustration, bond-stretching and bond-bending constants for wurtzite GaN, AlN and InN are given in Table 2.1. We have assumed $\alpha = \alpha'$ and $\beta = \beta'$, which were fitted to $c_{11} + c_{33}/2 + c_{12} + 2c_{13}$ and c_{13}/c_{33}. This simple, two constants model yields a reasonable account (within 7% for c_{44}) of all the elastic constant of wurtzite GaN, AlN and InN.

The bulk modulus

$$B = \frac{C_{33}(C_{11}+C_{12}) - 2C_{13}^2}{C_{11}+C_{12}+2C_{33}-4C_{13}}, \tag{2.16}$$

and the ratio

$$R = \frac{\varepsilon_\perp}{\varepsilon_\parallel} = 2\frac{C_{13}}{C_{33}}, \tag{2.17}$$

of the perpendicular to parallel bi-axial [0001] strain are compared with the data of reference (46). The internal strain parameters ζ_2 and ζ_3 of GaN and AlN are also compared with the ab *initio* values deduced from reference (47).

At the interface between, e.g. GaN and AlN, we take the average of $cos\theta_0$, $cos\theta_0'$ and β on Al-N-Al and Ga-N-Ga bond pairs for the Al-N-Ga bond pair.

Finally, we would like to emphasize that this model provides a local description of the elasticity of wurtzite materials similar to continuum elasticity theory. It misses, in particular, the long range electro-mechanical couplings due to pyro- and piezo-electricity. Although these couplings are actually often neglected ("semi-coupled" approach), they can be significant in some III-V devices (48; 49). If needed, electro-mechanical couplings might be taken into account in this model by introducing transverse or piezo-electric charges on the atoms that couple the macroscopic pyro- and piezo-electric fields (50).

2.4 Applications

Since the Keating VFF model only accounts for elastic relaxation (no dislocations), the comparison between the atomic postions obtained by the simulation and the positions obtained by an experimental method like TEM can suggest the presence or absence of dislocations in a system.

Next we will present the application of the Keating's VFF to the two cases. First we discuss GaN insertions in AlN nanocolumns, where the differences between the TEM images and the simulation actually points to the presence of dislocations. Second we discus

	GaN	AlN	InN	
a	3.189	3.112	3.545	Å
c	5.185	4.982	5.703	Å
u	0.3768	0.3819	0.3790	
α	88.35	83.79	67.38	N/m
β	20.92	19.83	10.01	N/m
c_{11}	389.9	391.6	226.6	GPa
	(390.0)	(396.0)	(223.0)	
c_{33}	404.9	373.6	223.4	GPa
	(398.0)	(373.0)	(224.0)	
c_{12}	138.9	141.1	112.6	GPa
	(145.0)	(137.0)	(115.0)	
c_{13}	110.6	105.4	93.3	GPa
	(106.0)	(108.0)	(92.0)	
c_{44}	111.6	107.6	49.5	GPa
	(105.0)	(116.0)	(48.0)	
B	2116	206.0	141.4	GPa
	(210.0)	(207.2)	(140.6)	
R	0.547	0.564	0.835	
	(0.533)	(0.579)	(0.821)	
ζ_2	0.08	0.08	0.09	
	(0.09)	(0.09)		
ζ_3	0.16	0.17	0.20	
	(0.17)	(0.19)		

Table 2.1: AlN GaN elastic constants -Lattice parameters, bond-stretching and bond-bending constants for wurtzite GaN, AlN and InN. The elastic constants c_{ij} computed from equations (2.12) and (2.13) are given and compared to experimental and ab-*initio* data (between parenthesis).

GaN/AlN nanowire superlattices with smaller radius where the agreement between the simulation and the X-Ray diffraction as well as the TEM suggests a perfect elastic relaxation of the system.

2.4.1 Structural properties of GaN insertions in AlN nanocolumns

The crystallographic perfection of III-V nitride nanowires (NWs), is of particular interest as it potentially provides a solution to overcome the problems inherent to the high density of dislocations usually found in bi-dimensional (2D) layers of this material family. As a matter of fact, nitride NWs can be viewed as a juxtaposition of non-coalesced grains, which leads to the suppression of threading edge dislocations formed at the coalescence of adjacent grains in usual conditions for 2D layer growth. As a further characteristics of NWs, it is now admitted that the large height/diameter aspect ratio and the large surface/volume ratio favors an elastic relaxation of the strain induced by the heteroepitaxy of these objects on various substrates (23).

Restricting ourselves to the case of GaN NWs grown without catalyst by molecular beam epitaxy, it has been shown by various groups that it results in high quality material exhibiting remarkable optical properties when compared to those of standard 2D layers (52) (53) (54) (55) (56). As a practical consequence of these excellent optical properties, it has been shown that nitride wire-like heterostructures present a potential interest for the realization of efficient light emitting devices (LEDs) in the visible (57; 58) and UV range (59).

It has been proposed that the growth of nitride nanowires is governed by the diffusion of metallic species along the side of the nanowires before incorporation on their top. This leads to a very large vertical to lateral growth rate ratio of about 32 in the case of GaN. However due to the reduced diffusion length of Al compared to Ga and to its enhanced probability of incorporation on the nanowires sides, the formation of AlN/GaN wire-like heterostructures is often accompanied by the growth of a thin AlN shell around the GaN insertion. This experimental feature raises the issue of strain relaxation in GaN/AlN core-shell heterostructures through dislocation formation beyond a given critical thickness.

As a matter of fact, the full understanding of the optical properties of GaN insertions in GaN/AlN nanowires heterostructures requires a careful determination of their strain sate and of the way the AlN shell affects it.

The investigated sample consisted of successive GaN inclusions, 30 nm in diameter and 2.5 nm in height, separated by 12 nm thick AlN regions, as shown in figure 2.3a. The sample was grown by PA-MBE under N-rich atmosphere The presence of a thin AlN shell around the wire can be noticed.

We will show that the 2.5 nm thick GaN insertions are partially relaxed, due to the presence of dislocations in the external AlN capping layer, in close relationship with the morphology of GaN insertions and with the AlN capping mechanism. The observed plastic relaxation in AlN is consistent with the small critical thickness expected for GaN/AlN radial heterostructures (22; 60).

The microstructure of the sample was analyzed by high resolution transmission electron microscopy (HRTEM). The strain component along the nanowire axis, ε_{zz}, was obtained with the Geometrical Phase Analysis (GPA) method. To perform the analysis, the 002 reflexion was selected in the Fourier transform of the HRTEM image, which enables to get the variation of the (002) lattice plane spacing with respecto to a reference region chosen as the AlN side part and taken as fully relaxed (61). ε_{zz} was calculated as $\varepsilon_{zz} = (d_{002} - d_{002,\text{ref}})/d_{002,\text{ref}}$ with $d_{002,\text{ref}} = \frac{1}{2}c_{\text{AlN,bulk}}$, (irrespective of the material) and is given in figure 2.3b. Concerning AlN, we note an in-plane tensile strain in the central part with respect to the reference side one, leading to a decrease of the AlN c-lattice spacing $(\approx -1\%)$ with respect to the reference region. Concerning the GaN inclusions, we notice that ε_{zz} is maximal in the central part, where it reaches about 6% and that it remains almost constant along the growth direction (Fig 2.3b). On the other hand, a lateral gradient is observed, with a decrease from the central part to the side one where it reaches about 4% , a value close to the GaN relaxed one.

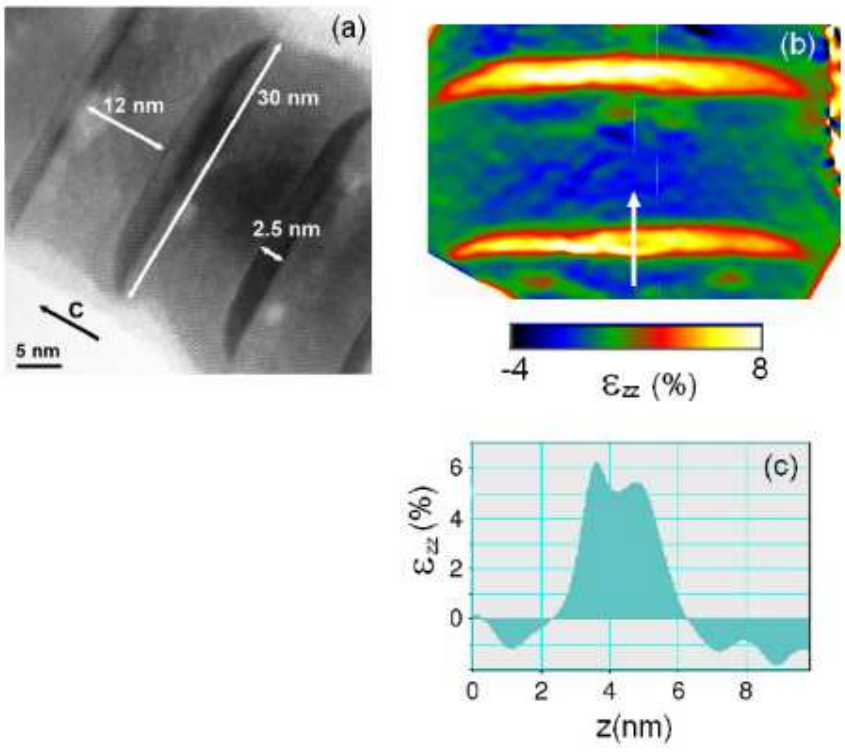

Figure 2.3: The GaN/AlN sample HRTEM image - (a) HRTEM showing the GaN insertions in AlN (b) Mapping of strain component ε_{zz} obtained from GPA. The reference region was taken in the AlN side part (c) ε_{zz} profile taken along the white arrow shown in (b).

These experimental results were compared with our results computed using the Keating's VFF model for the nonideal WZ . We considered [0001] oriented AlN nanowires with hexagonal cross section (radius R $\sim$ 15) nm and $\{1\bar{1}00\}$ facets. The GaN insertion was modelled as a slice of a sphere. Periodic boundary conditions were applied along the c axis on a supercell of length L = 14.5 nm. The dangling bonds were saturated with hydrogen atoms which have however little influence on the relaxation. The conjugate gradients algorithm was used to minimize the elastic energy with respect to the atomic positions and the period of the superlattice (62).

To make the calculation easily comparable to HRTEM results, the atomic columns were then projected in a $(1\bar{1}00)$ plane. The deformation ε_{zz} was computed from the average column positions using a finite difference scheme. Relaxed AlN was taken as reference for both materials. The ε_{zz} map in a 2.5 nm thick GaN insertion with radius R=15 nm is plotted in 2.4. As expected, the GaN layer mostly undergoes bi-axial compressive strain from the AlN nanowire and therefore tends to be dilated along the c axis ($\varepsilon_{zz} > 4\%$) despite the AlN shell (63). The strain appears to be maximal at the basis of the GaN layer where it peaks in the corners. The decrease of ε_{zz} towards the upper edge results from strain relaxation and from the increase of the AlN content in each projected atomic column. As a whole, this feature markedly departs from the GPA results, especially in the vicinity of the corners of GaN insertions.

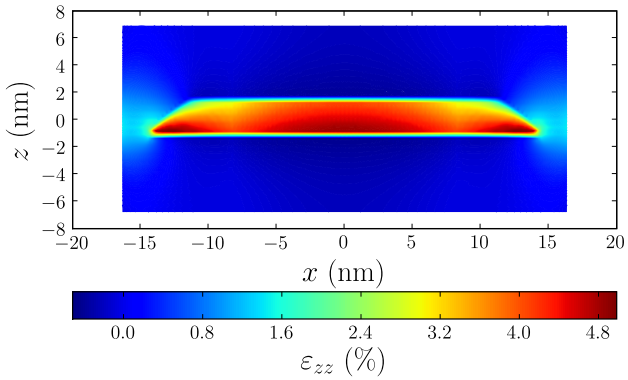

Figure 2.4: Calculated mapping of ε_{zz} - in a 2.5 nm thick GaN insertion with radius R=15 nm.

These discrepancies can be explained by the presence of a relaxation mechanism not taken into account in the calculations, such as the presence of dislocations. In fact, the appearance of dislocations in nanowires has been theoretically predicted in either axial (22) or coaxial heterostructures (60). The prediction depended on the lattice mismatch and wire radius, or core radius and shell thickness, respectively. A closer look at the HRTEM images

indeed reveals the insertion of an extra (0002) plane at the GaN/AlN interface as illustrated in figure 2.6 for three successive inclusions. Furthermore, from this image, one can point out that the dislocations occur at the same position along the oblique side of the three inclusions, corresponding to the same AlN shell thickness, namely about 3 nm. This is in qualitative agreement with what has been predicted [7] for coaxial nanowire heterostructures.

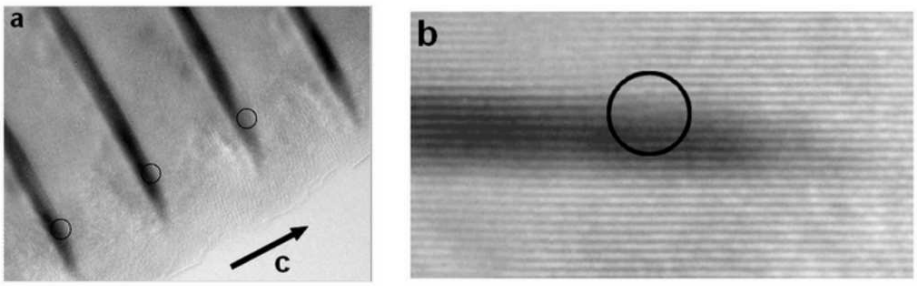

Figure 2.5: HRTEM image showing the presence of dislocations - (a) HRTEM image showing a dislocation at the AlN/GaN interface for three successive inclusions. (b) Enlargement showing the insertion of an extra (0002) plane in AlN.

In summary, we have shown that for thick GaN insertions which we found to be partially relaxed, strains release occured throught the formation of mistfit dislocations during the capping process. The location of dislocations in AlN further suggests that the rounded shape of GaN insertions is a determining feature, leading to a local radial thickening of the AlN capping layer beyond the critical thickness.

2.4.2 In-situ X-Ray diffraction in the growth of GaN/AlN superlattices

Whereas the above heterostructure did relax plastically upon the growth of the AlN shell, the GaN/AlN superlattices discussed in this paragraph show a completely different (elastic) behavior. The diameter ($\sim$ 25 nm) and period ($\sim$ 5nm) of these superlattices is indeed smaller than in the previous case, with no noticeable shell. The small diameter is expected to favor elastic strain relaxation, making them virtually free of dislocations. It is the goal of this section to address this issue by a combination of in-situ X-ray diffraction experiments, high resolution transmission electron microscopy (HRTEM) and theoretical calculations on GaN/AlN NW superlattices.

In-situ grazing incidence X-ray diffraction experiments were performed at the BM32 beamline of the European Synchrotron Radiation Facility (ESRF) in Grenoble (France). The substrate consisted of (111) Si. A thin AlN buffer layer (about 2-3 nm thick) was deposited onto the (111) Si substrate in order to ensure optimal vertical alignment of the GaN NWs which were used as a base for the AlN/GaN superlattice. Standard conditions were used for NW growth, namely a metal/N ratio of about 0.3 and a growth temperature in the 800-850°C

range (64) The growth of the AlN buffer layer, of the GaN NW base and of the GaN/AlN superlattice subsequently deposited was studied by performing h-scans along the $[10\bar{1}0]$ direction in the reciprocal space near the in-plane AlN $(30\bar{3}0)$ reflexion (radial scans are sensitive to strain. Note that in the following the reciprocal lattice unit h refers to the Si reciprocal space. The latter is obtained for Si described in a hexagonal cell whose [0001] direction is parallel to the cubic [111] axis. The hexagonal cell parameters are therefore $a_{h,Si} = \frac{\sqrt{2}}{2} a_{c,\mathrm{Si}}$, $c_{h,Si} = \sqrt{3} a_{c,\mathrm{Si}}$, where $a_{c,\mathrm{Si}}$ is the lattice parameter of the Si cubic cell. This means that the room temperature h value corresponding to the (30-30) reflection of bulk AlN and bulk GaN are equal to 3.706 and 3.62, respectively. On line monitoring of the GaN/AlN superlattice growth is shown in figure 2.6 The diffraction peak at $h = 3.605$ corresponds to the GaN NW base. The peak shift with respect to room temperature value (at $h = 3.62$) is consistent with the expected thermal expansion of GaN (65; 66) as the NW growth was performed in the 800-900 °Ctemperature range. The diffraction peaks near $h = 3.65$ correspond to the step-by step deposition of the GaN/AlN NW superlattice.

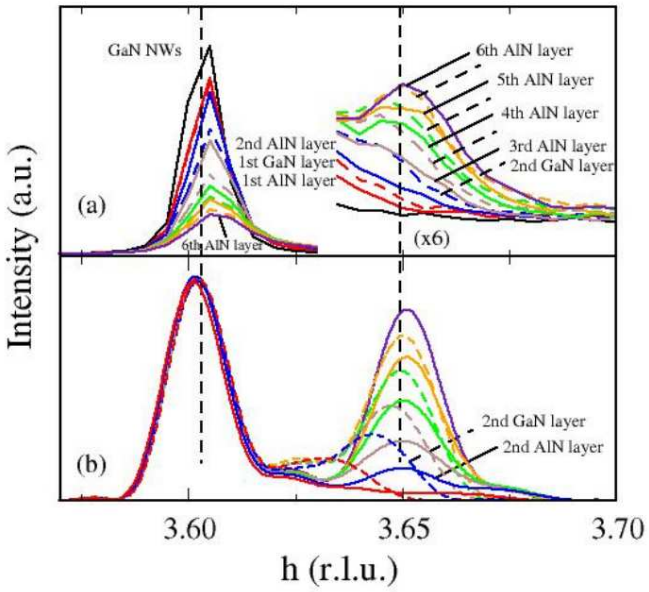

Figure 2.6: Superlattice X-Ray spectra - a) Sets of h-scans (radial scans) near the in-plane GaN $(30\hbar30)$ reflection, indexed in the Si hexagonal cell, taken at different steps of the AlN/GaN NW superlattice deposition. The X-ray beam incidence angle is 0.2° and the energy 10260 eV. The vertical dashed line at $h = 3.605$ represents bulk (relaxed) GaN h-position at 1100K. b) X-Ray diffraction peaks computed from atomic positions calculated in a purely elastic model (valence force field approach).

The strains in the GaN/AlN nanocolumns were computed with Keating's Valence Force Field (VFF). The lattice parameters a and c of GaN and AlN at the growth temperature T =

1100 K are taken from Refs. (65) and (66). The bond-stretching and bond-bending constants of the VFF were fitted to the macroscopic elastic constants c_{ij} extrapolated at T = 1100 K (67).

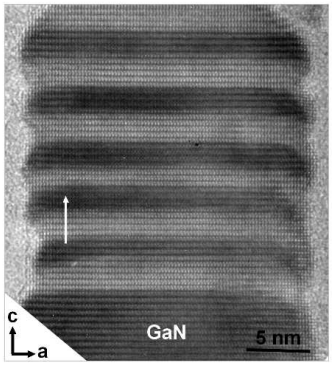

Figure 2.7: HRTEM image of the GaN/AlN NW superlattice - Five AlN/GaN bi-layers grown on a GaN basis are visible. The arrow indicates growth direction.

The nanocolumns are modeled as 23 nm diameter and 100 nm long GaN pillars with the heterostructure on top. These dimensions were measured in HRTEM images to be discussed below. At variance with the previous case no significant shell could be observed around the superlattice. Up to six 2.3 nm thick AlN and five 2 nm thick GaN layers were added one at a time. For each layer, the structure was relaxed with the VFF. The scattered X-Ray amplitude was computed from the atomic positions using a kinematical approximation around the GaN (300) reflection. For each h value, the intensity was integrated over the outgoing angle between 0 and 2.5° corresponding to the actual detector aperture.

The calculated in-plane strains $\varepsilon_{xx} + \varepsilon_{yy}$ are ploted in figure 2.8. The calculated X-Ray spectra are given in figure 2.6b. Both the GaN pillar and the superlattice diffraction peaks are slightly shifted towards small h values with respect to the experimental data, due to the uncertainty in determining the real growth temperature. However, despite this shift indicating that the actual growth temperature was lower than expected, calculations exhibit an excellent agreement with the experimental data reported in figure 2.6 a. In particular, the diffraction peak computed after the addition of a new GaN layer progressively shifts to the right while the diffraction peak computed after the addition of a new AlN layer emerges almost straight at $h = 3.655$. The position of the peaks rapidly stabilizes as the inner layers of the superlattice almost end in elastic equilibrium with the average alloy (45% GaN-55% AlN) suggested by the nominal thicknesses of GaN and AlN layers, thanks to the efficient strain relaxation allowed by the free surfaces. These trends are very well reproduced by the experimental data, as a first clue that the GaN/AlN NW superlattice is in elastic equilibrium with the GaN base.

At this stage, it has to be emphasized that, due to the reduced NW diameter, the presence of a single misfit dislocation at an AlN/GaN interface would lead to a significant relaxation

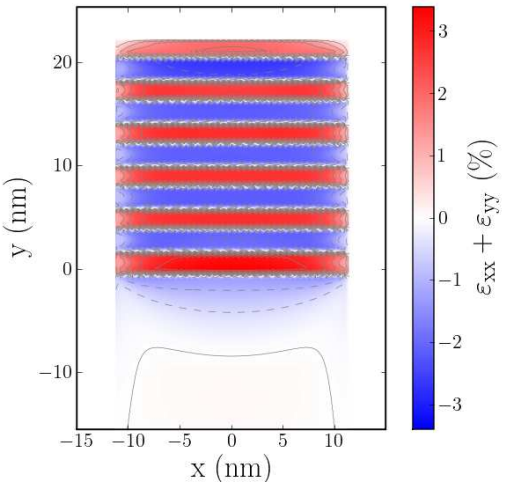

Figure 2.8: Superlattice in plane strain simulation - Mapping of the in plane strain $\varepsilon_{xx} + \varepsilon_{yy}$ using Keating's VFF for the nonideal WZ cell.

of the 2.4% in-plane lattice mismatch between AlN and GaN. If this was repeated for each AlN and GaN layer of the superlattice, as in the 2D case (68), one would not expect a single diffraction peak at the average alloy position, in contradiction with the actual experimental observations.

This statement was further confirmed by HRTEM experiments on the same sample as described above using a Jeol 4000EX microscope operated at 400 kV. For that purpose a cross-sectional specimen was prepared by sandwiching a slice of the NW sample together with a Si one using epoxy, and mechanically thinning the region of interest. The HRTEM image taken along the [11-20] zone axis and given in figure 2.7 shows the top part of a typical NW (23 nm in diameter), consisting in a GaN pillar (dark contrast), followed by five 2 nm thick GaN inclusions separated by 2.3 nm thick AlN spacers (light contrast).

A profile of *c* along the growth axis obtained with the GPA method and integrated over a 7 nm wide region in the central part of the NW is given in figure 2.9a. In order to make a comparison with HRTEM results, the local *c* parameter was computed with Keating's VFF from the average projections of the atomic columns perpendicular to the wire (see reference (61)) using room temperature GaN and AlN lattice parameters. The result, shown in figure 2.9b, puts in evidence an increase of *c* in the GaN insertions with respect to the relaxed material, which is in satisfactory agreement with the HRTEM profile. It can be noticed that this *c* value (0.522 nm), if introduced in the Poisson formula, leads to an in-plane parameter *a* = 0.315 nm, corresponding to 55% AlN-45% GaN alloy, i.e. also consistent with the nominal composition expected from the thickness of the AlN and GaN layers in the NW superlattice.

The agreement between the experiments reported above and the calculation performed in the framework of a purely elastic model is consistent with the fact that no dislocations could

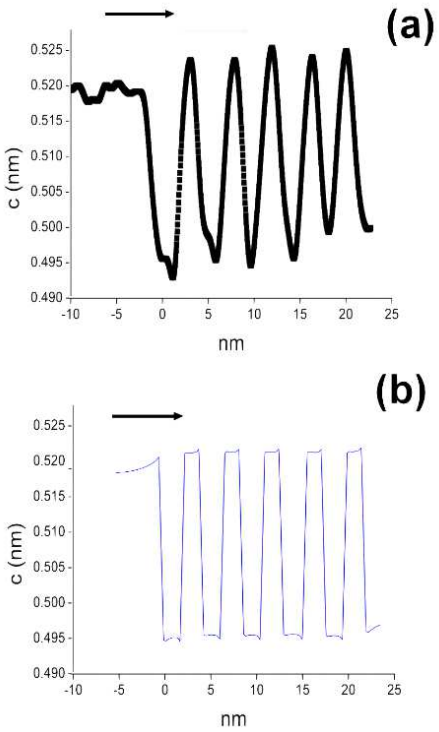

Figure 2.9: Profile of the c parameter - along the growth axis and taken in the central part of a NW, a) obtained from the Geometrical Phase Analysis of the HRTEM image. The arrows indicate growth direction. For convenience, the x-axis origin has been taken as the top of GaN pillar basis before the growth of the first AlN layer. b) Computed with Keating's valence force field.

be identified in figure 2.7 at the interface between AlN and GaN. This further supports the conclusion that the GaN/AlN NW superlattice is in elastic equilibrium with the GaN base. More generally, the issue of the critical thickness in axial NW heterostructures has been theoretically adressed by Ertekin *et al.* (22) and by Glas (23). These authors have used a thermodynamical approach based on the classical model of Matthews for the determination of the critical thickness in 2D heterolayers (51). They find that the critical thickness is far larger in nanowires than in 2D heterostructures thanks to the additional relaxation allowed by the NW free surfaces. In particular, they both predict the existence of a critical radius below which an infinitely long circular section can be grown on a mismatched basis. The value of the critical radius was found to depend on the lattice mismatch between the two segments as well as on the type and the Burgers'vector value of the dislocations introduced to minimize the total elastic energy. Although a precise determination of the critical thickness of axial NW heterostructures should take into account their exact hexagonally-faceted shape and consider the kinetical aspects of dislocation formation, the above mentionned theoretical approach was found to realistically predict the critical radius for various experimental systems (23). In the present case, an extrapolation of the theoretical data to GaN/AlN, assuming the formation of misfit dislocations with a Burgers' vector in the 0.1-0.3 nm range, leads to a critical radius of about 10 to 30 nm, respectively (reference (22)). Although the radius (11 nm) of the heterostructures considered here lays in the lower limit of this range, the experimental data are clearly consistent with a purely elastic strain relaxation mechanism. This further emphasizes the potential of NWs for the growth of dislocation-free superlattices. Whereas it is now well established that the diameter of catalyst-free GaN NWs grown by plasma-assisted MBE is typically in the 20-50 nm range, it has been recently demonstrated that this also holds in the case of AlN NWs (69). Therefore it can be safely concluded that the results reported here for the 2.4 % lattice mismatched AlN/GaN model system should also hold a fortiori for AlGaN/GaN or AlGaN/AlN heterostructures in the whole composition range, opening the path to the control of their growth and to the understanding of their optical properties.

Chapter 3

Electronic properties of nanostructures

3.1 Introduction

Recent breakthroughs made in the catalytic growth of semiconductor nanowires have allowed the synthesis of high-quality heterostructures with outstanding optical and transport properties. The composition of the nanowires can actually be modulated along the growth axis (axial heterostructures), as well as radially (core-shell structures). Strains are present in these devices and have an influence on the optical and electrical properties. Therefore modeling the electrical properties of such devices requires a detailed description of the effects of strains on the band structure. Over the past decades, *ab initio* methods such as density functional theory (DFT) have provided comprehensive information about the deformation potential of semiconductors. However, such *ab initio* methods require heavy computational resources and are not, therefore, suitable for the calculation of the electronic properties of large systems, of up to 10 million atoms. For that reason, the physics and electronics community is actively developing more efficient semiempical approaches, such as the $\mathbf{k}\cdot\mathbf{p}$, the empirical pseudopotential, or the tight-binding (TB) methods which can work out the electronic structure of strained semiconductor devices with a large number of atoms

In this chapter we discuss the effective mass, $\mathbf{k}\cdot\mathbf{p}$ and tight binding (TB) methods pointing out their strenghts and weaknesses. We present the band structure of the bulk materials studied during this work (GaN and AlN). We describe the effect of strains on the electronic structure using TB. Finally we present an application of the TB method to InP/InAs heterostuctures under strain.

3.2 The effective mass approximation

The effective mass approximation (EMA) is the simplest and the most widely used $\mathbf{k}\cdot\mathbf{p}$ method. It can be used to model the vicinity of the conduction band minimun which is described as a parabola:

$$E(\mathbf{k}) = \frac{\hbar^2\mathbf{k}^2}{2m^*} \tag{3.1}$$

where $\mathbf{k}$ is the wave vector and m^* is the effective mass taken as an empirical constant.

In an external, slowly variating potential $v(\mathbf{r})$, the wave functions of the electrons are written:

$$\varphi(\mathbf{r}) = \psi(\mathbf{r})u_c(\mathbf{r}) \tag{3.2}$$

where $u_c(\mathbf{r})$ is the conduction band Bloch function at $\mathbf{k} = \mathbf{0}$ and $\psi(\mathbf{r})$ is the so called "envelope function". The latter fulfills the equation

$$-\frac{\hbar^2}{2m^*}\Delta\psi + V\psi = E\psi\,, \tag{3.3}$$

In this method the atomic network is replaced by a continuous medium characterized by the confinement potentials for the electrons. The calculation time is thus independent of the number N of atoms.

The $\mathbf{k}\cdot\mathbf{p}$ models reproduce the principal bands of a bulk material around one $\mathbf{k}$ point in the first Brillouin zone. The model with four and six bands are employed to describe the maxima of the valence bands, while the models with eight bands can describe the maxima of the valence bands and the minimum of the conduction band simultaneously for direct gap semiconductors.

3.2.1 The quantum cubic box

Here we show an example of the use of the EMA. We consider an electron moving in a cubic box with dimensions (l_x, l_y, l_z) and "hard wall" boundaries. The potential $V(\mathbf{r})$ is therefore:

$$V(x,y,z) = V_x(x) + V_y(y) + V_z(z)\,, \tag{3.4}$$

where:

$$\begin{aligned}
V_x(x) = 0 \quad &\text{if} \quad |\,x\,| \leq \frac{l_x}{2} \;\text{ and }\; V_x(x) = +\infty \;\text{ otherwise} \\
V_y(y) = 0 \quad &\text{if} \quad |\,y\,| \leq \frac{l_y}{2} \;\text{ and }\; V_y(y) = +\infty \;\text{ otherwise} \\
V_z(z) = 0 \quad &\text{if} \quad |\,z\,| \leq \frac{l_z}{2} \;\text{ and }\; V_z(z) = +\infty \;\text{ otherwise}\,.
\end{aligned} \tag{3.5}$$

The x, y and z variables can be separated and the eigenvalues and wavefunctions split in three parts:

$$\psi(x,y,z) = \psi_x(x)\psi_y(y)\psi_z(z)\,, \tag{3.6}$$

$$E = E_x + E_y + E_z\,, \tag{3.7}$$

where:

$$\left[-\frac{\hbar^2}{2m^*}\frac{d^2}{dx^2} + V_x(x)\right]\psi_x(x) = E_x\psi_x(x)\,. \tag{3.8}$$

Similar equations hold along y and z.

The general solution of equation 3.8 for $x \leq \frac{l_x}{2}$ is:

$$\psi_x(x) = A\sin(k_x x) + B\cos(k_x x)\,. \tag{3.9}$$

Outside the box the potential is infinite and the only possible solution is $\psi = 0$. Taking the origin at the center of the cubic box, we must therefore fulfill the continuity condition:

$$\psi_x\left(\pm\frac{l_x}{2}\right) = 0\,, \tag{3.10}$$

This implies:

$$A = 0 \quad \text{and} \quad k_x = \frac{\pi}{l_x} + \frac{2n\pi}{l_x}\,, \quad n \in \mathbb{N}^* \tag{3.11}$$

or:

$$B = 0 \quad \text{and} \quad k_x = \frac{2n\pi}{l_x}\,, \quad n \in \mathbb{N}^*\,. \tag{3.12}$$

Therefore, $k_x = \dfrac{\pi n_x}{l_x}$, n_x strictly positive integer and:

$$E_x = \frac{\hbar^2 k_x^2}{2m^*} = \frac{\hbar^2\pi^2}{2m^*}\frac{n_x^2}{l_x^2}\,. \tag{3.13}$$

Summing over x, y and z, we finally get:

$$E(n_x, n_y, n_z) = \frac{\hbar^2\pi^2}{2m^*}\left(\frac{n_x^2}{l_x^2} + \frac{n_y^2}{l_y^2} + \frac{n_z^2}{l_z^2}\right)\,. \tag{3.14}$$

We notice that the energy is inversely proportional to the square of the box dimensions.

In figure 3.1 we show the results for a cubic box with $l_x = l_y = l_z$. We can observe that the density of states increases when the energy increases. Also, we can compare the eigenstates of the cubic box case with hydrogen-like orbitals. In particular the eigenstate corresponding to $(1,1,1)$ (in blue on the figure 3.1) is not degenerate and is comparable to the *s* orbital of an H atom. In the same way, the eigenstates corresponding to $(1,1,2), (1,2,1)$ and $(2,1,1)$ (in pink on the figure 3.1) are triple degenerate and are comparable with the *p* orbitals. Higher lying eigenstates lack this correspondence with atomic orbitals due to the cubic instead of spherical symmetry of the problem.

3.2.2 EMA Limitations

In principle the effective mas approximation is only valid for a weak and slowly varying potential. This model is effective, simple and accurate for the treatment of the conduction band in large systems. Yet it fails in highly confined systems such as small nanocystals because the parabolic approximation does not reproduce the conduction bands at high enough energy.

The 4 and 6 bands $\mathbf{k}\cdot\mathbf{p}$ model for the valence band are much more difficult to solve, but suffer for the same deficiencies in highly confined systems.

In the EMA and $\mathbf{k}\cdot\mathbf{p}$method only a few bands are explicitly accounted and these models are only valid in regions of the Brillouin zone close to the Γ point. However, In many applications one also needs to describe states away from the Γ point. The far (deep or high) bands can play a significant role in the confined states energy (70). This effect is more

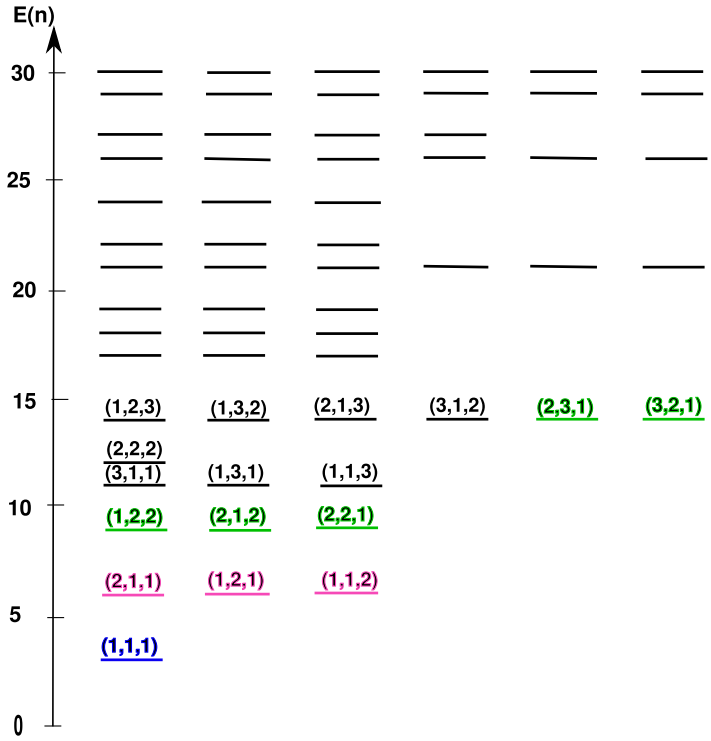

Figure 3.1: Cubic quantum box - Eigenvalues for a cubic potential box with $l_x = l_y = l_z$. The energy is given in units of $\frac{\hbar^2\pi^2}{2m^*l^2}$. The values of (n_x, n_y, n_z) are given in parenthesis.

evident in the case of strained systems, because the strains are known to couple bands of different symmetries.

3.3 The Tight Binding method

While the nearly free electron model is a reasonably good representation of the electronic structure of simple metals, the tight binding (TB) method provides a more faithful representation of systems where the electrons are localized in chemical bonds of different degrees of co-valency. The main idea of this method is to consider a basis set of atomic orbitals, and the interaction between them forming molecular orbitals.

We consider a single particle Hamiltonian H:

$$H = -\frac{\hbar^2}{2m}\nabla^2 + v_{\text{eff}}\,, \tag{3.15}$$

where the effective potential v_{eff} describes both, the ionic and average electron-electron interactions and is written as a sum of atomic potentials:

$$v_{\text{eff}}(\mathbf{r}) = \sum_k v_k(\mathbf{r}-\mathbf{R}_k)\,, \tag{3.16}$$

where v_k is a spherical atomic potential, centered on the atom at position $\mathbf{R}_k$. In the TB approach the single particle wave functions are written as linear combinations of atomic orbitals:

$$\psi(\mathbf{r}) = \sum_{i,\alpha} C_{i\alpha}\varphi_\alpha(\mathbf{r}-\mathbf{R}_i)\,, \tag{3.17}$$

where $\varphi_\alpha(\mathbf{r}-\mathbf{R}_i)$ is on orbital of type α (s, p_x, p_y, ...) centered on an atom i and $C_{i\alpha}$ is an expansion coefficient. At this point we can write the Schrödinger equation $H\psi = E\psi$ as:

$$\sum_{i,\alpha} C_{i\alpha} H \mid \varphi_\alpha(\mathbf{r}-\mathbf{R}_i)\rangle = E\sum_{i,\alpha} C_{i\alpha} \mid \varphi_\alpha(\mathbf{r}-\mathbf{R}_i)\rangle\,, \tag{3.18}$$

and then project onto an orbital $\varphi_\beta(\mathbf{r}-\mathbf{R}_j)$:

$$\sum_{i,\alpha} C_{i\alpha} \left\langle \varphi_\beta(\mathbf{r}-\mathbf{R}_j) \mid H \mid \varphi_\alpha(\mathbf{r}-\mathbf{R}_i)\right\rangle = E\sum_{i,\alpha} C_{i\alpha} \left\langle \varphi_\beta(\mathbf{r}-\mathbf{R}_j) \mid \varphi_\alpha(\mathbf{r}-\mathbf{R}_i)\right\rangle\,. \tag{3.19}$$

We define:

$$H_{j\beta,i\alpha} = \left\langle \varphi_\beta(\mathbf{r}-\mathbf{R}_j) \mid H \mid \varphi_\alpha(\mathbf{r}-\mathbf{R}_i)\right\rangle \quad \text{(Hamiltonian matrix elements)} \tag{3.20}$$

$$S_{j\beta,i\alpha} = \left\langle \varphi_\beta(\mathbf{r}-\mathbf{R}_j) \mid \varphi_\alpha(\mathbf{r}-\mathbf{R}_i)\right\rangle \quad \text{(Overlap matrix elements)}\,. \tag{3.21}$$

Equation 3.19 then reads:

$$\sum_{i,\alpha} H_{j\beta,i\alpha} C_{i\alpha} = E\sum_{i,\alpha} S_{j\beta,i\alpha} C_{i\alpha}\,. \tag{3.22}$$

In order to simplify the notation we introduce an index I which labels each orbital of each atom ($I = i,\alpha$):

$$\sum_I H_{J,I} C_I = E\sum_I S_{J,I} C_I \quad \forall J\,. \tag{3.23}$$

Using matrix notation, this can be written:

$$\widehat{H}\widehat{C} = E\widehat{S}\widehat{C}\,, \tag{3.24}$$

where $\widehat{H}$ is the Hamiltonian operator, $\widehat{S}$ the overlap matrix, and $\widehat{C}$ the vector of expansion coefficients.

The diagonal elements $H_{I,I}$ have the form:

$$H_{I,I} = \int \varphi_\alpha^*(\mathbf{r}-\mathbf{R}_i)\left[-\frac{\hbar^2}{2m}\nabla^2 + v_i(\mathbf{r}-\mathbf{R}_i)\right]\varphi_\alpha(\mathbf{r}-\mathbf{R}_i)d^3\mathbf{r} = \varepsilon_0\,, \tag{3.25}$$

and they are called the on-site energies. The off-diagonal elements $H_{J,I}$ are called the hopping terms.

In the semi-empirical tight binding approach further approximations are usually made:

- The interactions are limited to first, second or third nearest neighbors. This is justified by the fact that distant orbitals have negligible overlap. In this work we have used first nearest neighbor models. As a consequence the $\widehat{H}$ and $\widehat{S}$ matrices are "sparse" (mostly contain zeros), so that equation 3.23 can be solved with fast iterative methods for sparse matrices.

- The orbital are assumed orthogonal ($\widehat{S} = \widehat{I}$). This can in principle be achieved trough a so called Löwdin transformation, though at the expense of longer range interactions.

- The so called three center terms $\sum_{k\neq i,j} v_k(\mathbf{r}-\mathbf{R}_k)$ are neglected in the hopping terms $H_{J,I}$:

$$H_{J,I} = \int \varphi_\beta^*(\mathbf{r}-\mathbf{R}_j)\left[-\frac{\hbar^2}{2m}\nabla^2 + v_i(\mathbf{r}-\mathbf{R}_i) + v_j(\mathbf{r}-\mathbf{R}_j) + \sum_{k\neq i,j} v_k(\mathbf{r}-\mathbf{R}_k)\right]\varphi_\alpha(\mathbf{r}-\mathbf{R}_i)d^3\mathbf{r}\,. \tag{3.26}$$

This two center approximation allows for a convenient separation between the bond length and angular dependence of the TB matrix elements (Slater-Koster relations (34)). For example the interaction between two p orbitals can always be splitted into a $pp\sigma$ interactio (for p components aligned along the bond), and a $pp\pi$ interaction (for p components perpendicular to the bond, see figure 3.2).

The independent TB matrix elements of the Hamiltonian are finally considered as adjustable parameters fitted to reproduce the bulk band structures, then transferred to the nanostructures.

The quality of the TB band structure depends on the basis set used in the model. The minimal sp^3 model (one s orbital and tree p orbitals) is quite accurate for the valence band of usual semiconductors, but less for the conduction bands, especially at high energy. The sp^3d^5 model (with 5 more d orbitals) improves the description of the conduction bands. The most accurate results are however obtained with the $sp^3d^5s^*$ model which includes an extra s orbital. This is the model we have used in this work.

The TB method provides a faithful description of the band structure over the whole first Brillouin zone, at variance with $\mathbf{k}\cdot\mathbf{p}$ methods. It therefore expected to be more accurate in highly confined systems, at the expense of a larger numerical cost.

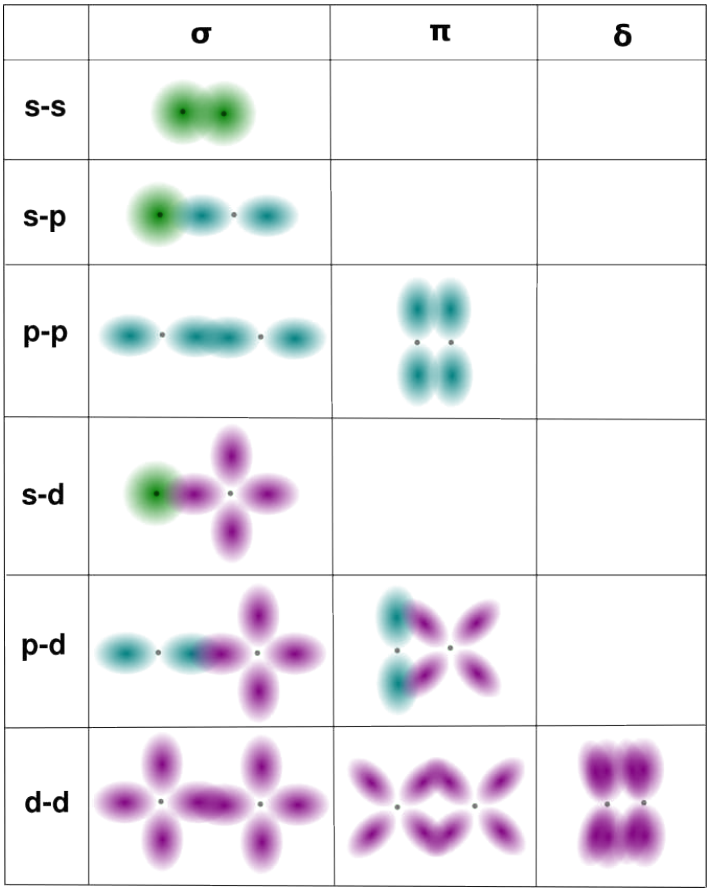

Figure 3.2: Linear Combination of Atomic Orbitals - The different two-center interactions involved in the Slater-Koster relations.

During this work we have mostly used the first nearest neighbors, two-center orthogonal tight binding model of Jancu *et al.* (78). This set of parameters is transferable from the zinc-blende to the wurtzite phase. Since the bond lengths are different in the two phases, the dependence of the hopping two-center integrals $V_{\mu\nu}$ on the interatomic distances $d_{\mu\nu}$ (μ and ν being tow orbitals on different atoms) is modeled by a power law ("Harrison law"):

$$V_{\mu\nu}(d_{\mu\nu}) = V_{\mu\nu}(d_0)\left(\frac{d^0_{\mu\nu}}{d_{\mu\nu}}\right)^{\eta}, \tag{3.27}$$

where $d^0_{\mu\nu}$is the equilibrium distance and η an exponent. The on-site energies, nearest neighbors two-center integrals and exponents are given in tables 3.1, 3.2 and 3.3. Note that the p and d orbitals are not degenerate in the wurtzite phase, as expected from the lower symmetry of the crystal.

On-site energy	Ga	N (in GaN)	Al	N (in AlN)
E_s	4.75010	-8.93790	6.07280	-8.97170
E_{p_x}	11.45010	2.06260	11.53680	2.16790
E_{p_y}	11.45010	2.06260	11.53680	2.16790
E_{p_z}	11.45010	2.06260	11.53680	2.16790
$E_{d_{yz}}$	27.93580	28.43213	29.49800	29.85100
$E_{d_{xz}}$	27.93580	28.43213	29.49800	29.85100
$E_{d_{xy}}$	27.46280	28.92097	29.09210	30.14210
$E_{d_{x^2-y^2}}$	27.46280	28.92097	29.09210	30.14210
$E_{d_{3z^2-r^2}}$	28.40880	27.94330	29.90390	29.55990
E_{s^*}	35.05070	28.82530	35.00410	28.82530

Table 3.1: On-site parameters $E_I = H_{I,I}$ for the wurtzite phase - Parameters from Jancu *et al.* (78), in eV.

3.4 GaN and AlN band structures

In this section, we describe the band structure of the bulk materials studied in this work, GaN and AlN, using the tight binding models.

3.4.1 Band structure of GaN and AlN in the zinc-blende structure

The electronic band structure of GaN and AlN in the zinc-blende structure are shown in figures 3.3 and 3.4. It is known that the band gap of GaN in the zinc-blend structure is 4.59 eV and the band gap of AlN in the zinc-blende structure is 4.90 eV (46).

If we do a zoom of the band structure of GaN around the Γ point (see figure 3.5) we can distinguish one conduction band (CB) and three valence bands (VB) which are called the heavy holes (HH), light holes (LH), and the split off (SO) bands.

Hopping term	Energy	Hopping term	Energy
$s_{\mathrm{Ga}}s_{\mathrm{N}}\sigma$	-2.5495	$s_{\mathrm{Al}}s_{\mathrm{N}}\sigma$	-2.6261
$s^*_{\mathrm{Ga}}s^*_{\mathrm{N}}\sigma$	-3.9997	$s^*_{\mathrm{Al}}s^*_{\mathrm{N}}\sigma$	-4.4940
$s_{\mathrm{Ga}}s^*_{\mathrm{N}}\sigma$	-3.7569	$s_{\mathrm{Al}}s^*_{\mathrm{N}}\sigma$	-2.9127
$s^*_{\mathrm{Ga}}s_{\mathrm{N}}\sigma$	-2.0860	$s^*_{\mathrm{Al}}s_{\mathrm{N}}\sigma$	-1.8773
$p_{\mathrm{Ga}}s_{\mathrm{N}}\sigma$	3.9210	$p_{\mathrm{Al}}s_{\mathrm{N}}\sigma$	3.7546
$s_{\mathrm{Ga}}p_{\mathrm{N}}\sigma$	4.0489	$s_{\mathrm{Al}}p_{\mathrm{N}}\sigma$	3.9269
$p_{\mathrm{Ga}}s^*_{\mathrm{N}}\sigma$	-4.2911	$p_{\mathrm{Al}}s^*_{\mathrm{N}}\sigma$	-4.0680
$s^*_{\mathrm{Ga}}p_{\mathrm{N}}\sigma$	-2.0861	$s^*_{\mathrm{Al}}p_{\mathrm{N}}\sigma$	-1.8328
$p_{\mathrm{Ga}}p_{\mathrm{N}}\sigma$	4.7429	$p_{\mathrm{Al}}p_{\mathrm{N}}\sigma$	4.3117
$p_{\mathrm{Ga}}p_{\mathrm{N}}\pi$	-1.4302	$p_{\mathrm{Al}}p_{\mathrm{N}}\pi$	-1.2842
$d_{\mathrm{Ga}}s_{\mathrm{N}}\sigma$	-3.9072	$d_{\mathrm{Al}}s_{\mathrm{N}}\sigma$	-3.8483
$s_{\mathrm{Ga}}d_{\mathrm{N}}\sigma$	-1.2252	$s_{\mathrm{Al}}d_{\mathrm{N}}\sigma$	-1.0331
$d_{\mathrm{Ga}}s^*_{\mathrm{N}}\sigma$	-2.0963	$d_{\mathrm{Al}}s^*_{\mathrm{N}}\sigma$	-2.1897
$s^*_{\mathrm{Ga}}d_{\mathrm{N}}\sigma$	-1.7553	$s^*_{\mathrm{Al}}d_{\mathrm{N}}\sigma$	-1.5559
$d_{\mathrm{Ga}}p_{\mathrm{N}}\sigma$	-1.9007	$d_{\mathrm{Al}}p_{\mathrm{N}}\sigma$	-2.1306
$p_{\mathrm{Ga}}d_{\mathrm{N}}\sigma$	-1.3286	$p_{\mathrm{Al}}d_{\mathrm{N}}\sigma$	-1.2470
$d_{\mathrm{Ga}}p_{\mathrm{N}}\pi$	2.2761	$d_{\mathrm{Al}}p_{\mathrm{N}}\pi$	2.5342
$p_{\mathrm{Ga}}d_{\mathrm{N}}\pi$	3.2195	$p_{\mathrm{Al}}d_{\mathrm{N}}\pi$	3.1629
$d_{\mathrm{Ga}}d_{\mathrm{N}}\sigma$	-1.2016	$d_{\mathrm{Al}}d_{\mathrm{N}}\sigma$	-1.0791
$d_{\mathrm{Ga}}d_{\mathrm{N}}\pi$	6.0757	$d_{\mathrm{Al}}d_{\mathrm{N}}\pi$	6.4201
$d_{\mathrm{Ga}}d_{\mathrm{N}}\delta$	-4.4436	$d_{\mathrm{Al}}d_{\mathrm{N}}\delta$	-4.5012

Table 3.2: Hopping terms - Parameters from Jancu *et al.* (78), in eV.

Power law	GaN	AlN
$\eta_{ss\sigma}$	3.65	3.55
$\eta_{s*s\sigma}$	1.98	1.05
$\eta_{sp\sigma}$	4.91	4.71
$\eta_{s*p\sigma}$	1.05	1.36
$\eta_{sd\sigma}$	1.02	1.12
$\eta_{s*d\sigma}$	4.32	4.70
$\eta_{pp\sigma}$	4.09	3.56
$\eta_{pp\pi}$	3.35	2.25
$\eta_{pd\sigma}$	1.24	2.02
$\eta_{pd\pi}$	1.02	1.05

Table 3.3: Power law parameters - Parameters from Jancu *et al.* (78).

As can be seen in the figures 3.3 and 3.4 the band gap of GaN in this structure is direct while the bandgap of AlN is indirect.

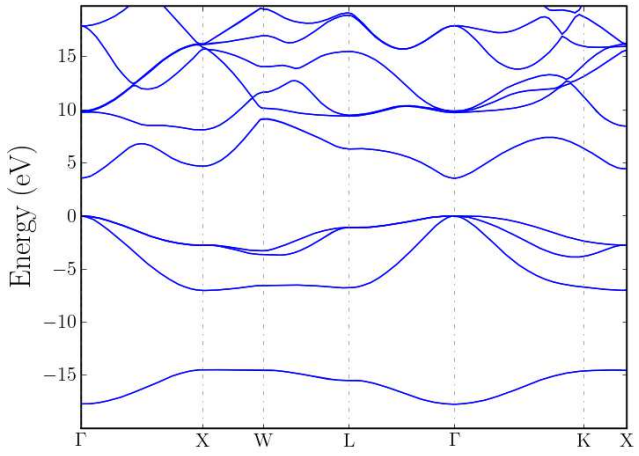

Figure 3.3: Electronic band structure of ZB GaN - Tight-binding band structure of bulk zinc-blende GaN.

3.4.2 Band structure of GaN and AlN in the wurtzite structure

The band structure of GaN and AlN in the wurtzite phase are shown in figures 3.6 and 3.7. We can see that in the WZ structure the band gap of both materials is direct. This phase is more interesting because the band gap difference is bigger than in the zinc-blende materials; the band gap of GaN is 3.51 eV while the gap of AlN is 6.25 eV

In wurtzite GaN and AlN, the bottom of the conduction band and the top of the valence bands are found at the Γ point in the BZ. The lowest conduction band is a linear combination of *s* orbitals while the highest valence band is a linear combination of p orbitals. The three valence bands originating from these three orbitals are split by the crystal field and spin-orbit couplings into "A", "B" and "C" bands (see figure 3.8) with different symmetries

In figures 3.9 and 3.10 we notice that the order of the A B and C bands is different for GaN and AlN. In GaN the fundamental band gap is between the conduction and the A band, while in AlN the fundamental bandgap is between the conduction and the C band. The crystal field splitting is indeed negative in AlN, while it is positive in GaN.

3.5 Effect of strain on the band structure

In this subsection we discus the effects of strains on the conduction and valence bands. When a stress is applied to the system, the band structure is indeed modified (33; 71). We

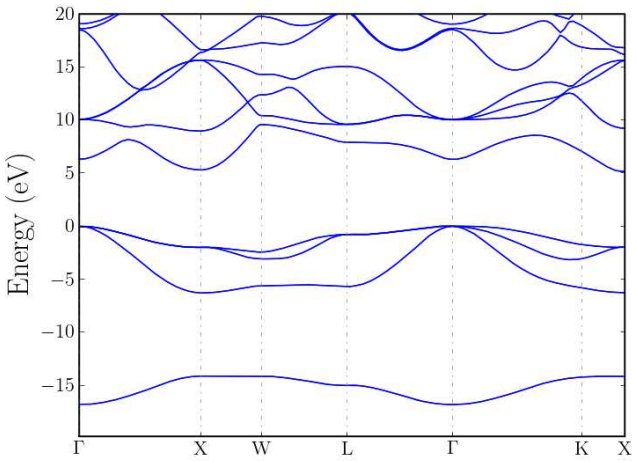

Figure 3.4: Electronic band structure of ZB AlN - Tight-binding band structure of bulk zinc-blende AlN.

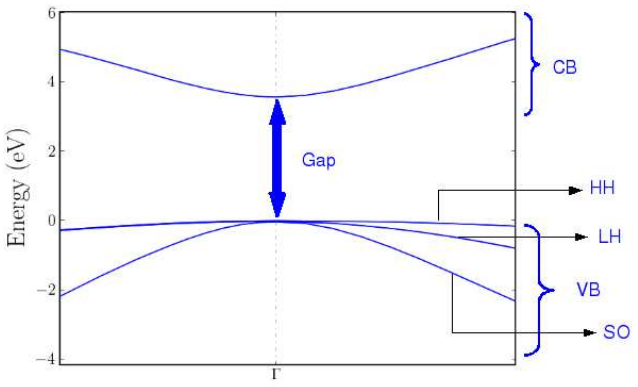

Figure 3.5: Band structure of bulk zinc-blende GaN - around the Γ point.

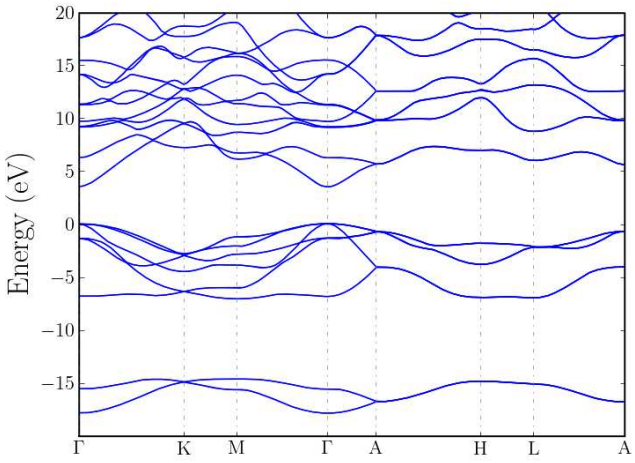

Figure 3.6: Electronic band structure of WZ GaN - Tight-binding band structure of bulk wurtzite GaN.

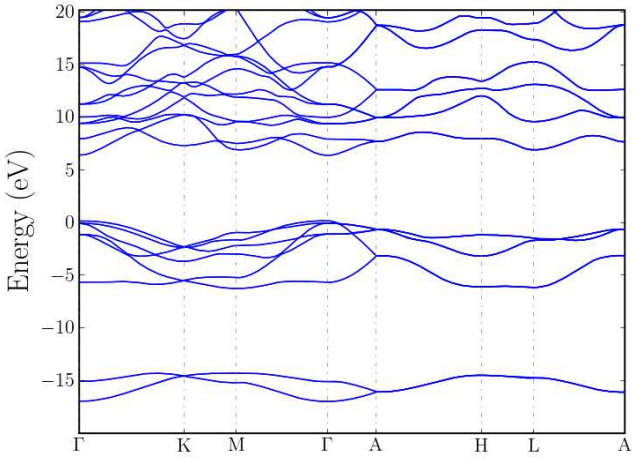

Figure 3.7: Electronic band structure of WZ AlN - Tight-binding band structure of bulk wurtzite AlN.

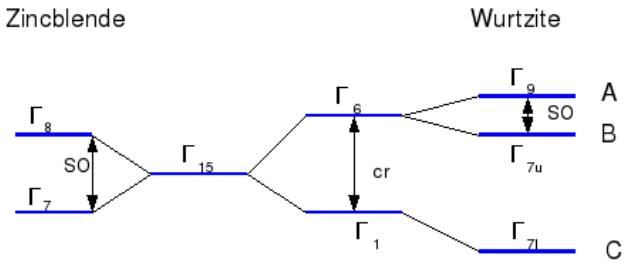

Figure 3.8: Valence bands in the zinc-blende and wurtzite crystal structures. -

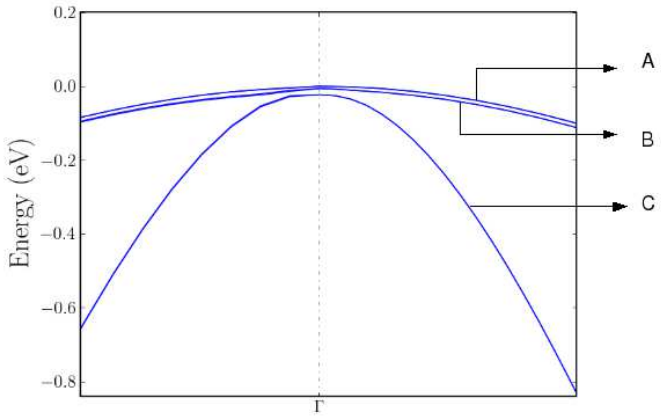

Figure 3.9: Valence band structure of bulk wurtzite GaN - around the Γ point.

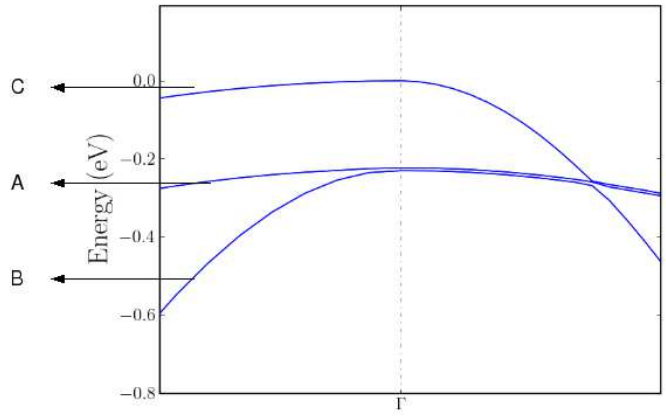

Figure 3.10: Valence band structure of bulk wurtzite AlN - around the Γ point.

focus here on the wurtzite structure, which is the main interest of this thesis.

3.5.1 Deformation potentials

The effect of an *arbitrary* stress on the conduction band, *CB*, can be described by a simple shift of the bands, which is given by:

$$CB = CB(0) + a_{cz}\varepsilon_{zz} + a_{cx}(\varepsilon_{xx} + \varepsilon_{yy}), \tag{3.28}$$

where a_{cz} and a_{cx} are the deformation potentials of the conduction band and ε_{ij} are the components of the strain tensor. $CB(0)$ denotes the energy of the first conduction band in the absence of applied stress.

For the sake of simplicity we neglect spin-orbit coupling in the following. The valence bands A and B are then degenerate.

Let us now consider the effect of an applied *bi-axial* (0001) stress on the valence bands. An applied bi-axial (0001) stress is characterized by a strain tensor whose components satisfy $\varepsilon_{xx} = \varepsilon_{yy} = \varepsilon_{\|}$ and $\varepsilon_{zz} = \varepsilon_{\perp}$. The resulting shift of the A/B and C bands are given by:

$$A/B = A/B(0) + 2D_2\varepsilon_{\|} + 2D_4\varepsilon_{\|} + D_1\varepsilon_{\perp} + D_3\varepsilon_{\perp}, \tag{3.29}$$

and:

$$C = C(0) + 2D_2\varepsilon_{\|} + D_1\varepsilon_{\perp}. \tag{3.30}$$

Here D_i, $i = 1,\ldots,4$ are the valence bands deformations potentials. Note that under a bi-axial strain the A and B valence bands remain degenerate.

Additionally, we can consider the effect of a deformation given by $\varepsilon_{xx} = -\varepsilon_{yy}$ and $\varepsilon_{ij} = 0$ otherwise. In this case the A and B bands will split and the difference in energy between them is proportional to the deformation potentials, D_5, according to (33):

$$A = A(0) - 2D5\varepsilon_{xx}, \tag{3.31}$$

and:

$$B = B(0) + 2D5\varepsilon_{xx}\,, \tag{3.32}$$

We see that the splitting between the A and B valence bands is just given by $4D_5\varepsilon_{xx}$. Under these conditions the C valence band is unaffected by the applied strain, i.e.,

$$C = C(0)\,. \tag{3.33}$$

Finally we can consider a shear deformation given by $\varepsilon_{yz} \neq 0$ or $\varepsilon_{xz} \neq 0$ (while $\varepsilon_{ij} = 0$ otherwise). Again the degeneracy between the A and B bands is lifted under the influence of such a shear deformation. The splitting is proportional, in this case, to the deformation potential D_6:

$$A = \frac{1}{2}\left(A(0) + \sqrt{A(0)^2 + 8D_6^2\varepsilon_{yz}^2}\right)\,, \tag{3.34}$$

and:

$$B = \frac{1}{2}\left(B(0) - \sqrt{B(0)^2 + 8D_6^2\varepsilon_{yz}^2}\right)\,, \tag{3.35}$$

while, again, the C valence band energy remains unchanged:

$$C = C(0)\,. \tag{3.36}$$

The deformation potentials of GaN and AlN are not all well characterized (in particular D_5 and D_6). We report in table 3.4 a set of deformation potentials proposed by Vurgaftman and Meyer[1] (see reference (46)). The deformation potentials of the TB model of Jancu *et al.* are reported in table 3.6 for GaN. Jancu *et al.* did not attempt to reproduce these deformation potentials which are not actually very well given. We have therefore tried to improve this description as described in the next paragraph.

Potential	**GaN**	**AlN**	
a_{cx}	-4.5	0.6[1]	eV
a_{cz}	-6.8	-20.1[1]	eV
D_1	-3.7	-17.1[1]	eV
D_2	4.5	7.9	eV
D_3	8.2	8.8	eV
D_4	-4.1	-3.9	eV
D_5	-4.0	-3.4	eV
D_6	-5.5	-3.4	eV

Table 3.4: Deformation potentials for GaN and AlN, adapted from reference (46). The deformation potentials control band-structure effects associated with applied strains.

[1]The value of D_1, and the values of a_{cx} and a_{cz} for AlN deduced from Ref. (46) seem, however, highly doubtful.

3.5.2 GaN and AlN TB parameters including the effect of strains

The modeling of the electrical properties of semiconductor heterostructures for optoelectronic applications requires a detailed description of the effects of strains on the band structure. The TB method can work out the electronic structure of strained semiconductor devices and has proved to be successful in predicting the electronic properties of semiconductor nanostructures such as nanocrystals or nanowires. The use of an atomic-orbital basis set with interactions limited to a few nearest neighbors (so the resulting matrices are sparse) allows the calculation of the wave function of million atom systems (72; 73). In this respect, the first nearest neighbor $sp^3d^5s^*$ model is one of the most accurate and efficient TB description of semiconductor materials.

The effects of strains are accounted for in TB models through the bond-length dependence of the nearest-neighbor parameters $V_{\mu\nu}$ (where μ and ν are indices associated with two orbitals on different atoms), which is usually fitted to a power law as we saw in equation (3.27). Although some hydrostatic and uniaxial deformation potentials can be reproduced that way (74), much better accuracy can be achieved with the introduction of strain-dependent on-site parameters (See Refs. (75), (76) and (77)). In their original $sp^3d^5s^*$ parametrization, Jancu *et al.* (78) introduced a term that lifts the degeneracy among the d_{yz}, d_{xz}, and d_{xy} orbitals as a function of the applied uniaxial strain. This approach was later generalized to arbitrary strains by Boykin (76) and Niquet (77).

Let us illustrate the model of Niquet *et al* (77), for the simplified case of the s orbitals in the zinc-blende structure (see reference (77) for a complete description). The model of Niquet *et al.* is based on a first-order expansion of the on-site matrix elements as a function of the nearest neighbors distances, assuming that the total potential is the sum of central atomic contributions.

Consider the on-site potential of the s-orbital of atom i on sublattice 1 (which we denote V_s) that just interacts with its first nearest neighbors on sublattice 2. This on-site potential contains two contributions, one coming from the effective potential of sublattice 1 (v_1), the other coming from the effective potential of the sublattice 2 (v_2). The latter term depends on the distance between the center of the s-orbital s and its first nearest-neighbours, $d_{ij} = |\mathbf{R}_i - \mathbf{R}_j|$,

$$V_s = V_1 + \sum_j^{NN} V_2(d_{ij}), \tag{3.37}$$

where the sum is over all the first nearest-neighbours, and:

$$V_1 = \langle s_i \mid v_1(\mid \mathbf{r} - \mathbf{R}_i \mid) \mid s_i \rangle, \tag{3.38}$$

$$V_2(d_{ij}) = \langle s_i \mid v_2(\mid \mathbf{r} - \mathbf{R}_j \mid) \mid s_i \rangle \;\; i \neq j, \tag{3.39}$$

where $v_{1/2}$ are the atomic potentials.

This last term V_2 can be developed to first-order in powers of the changes in bond lengths, $d_{ij} - d_0$, where d_0 is the unstrained bond length. This yields a strain independent contribution as well as a term dependent on the bond lengths:

$$V_2(d_{ij}) = V_2(d_0) + \frac{3}{4}\alpha_s \frac{d_{ij} - d_0}{d_0} + \ldots, \tag{3.40}$$

where we have introduced a new TB parameter, α_s which is yet to be determined. Hence the expression for the *s*-orbital on-site potential becomes:

$$V_s = V_1 + \sum_j^{NN} V_2(d_0) + \frac{3}{4}\alpha_s \sum_j^{NN} \frac{d_{ij} - d_0}{d_0}, \tag{3.41}$$

The third term on the right-hand side can be related to the hydrostatic deformation $\frac{\delta\Omega}{\Omega_0} = \varepsilon_{xx} + \varepsilon_{yy} + \varepsilon_{zz}$. The quantity $\frac{\delta\Omega}{\Omega_0}$ gives the first-order variation of the volume of the material under an applied strain, with respect to the volume of the unstrained material, Ω_0, and can approximated as:

$$\frac{\delta\Omega}{\Omega_0} \approx \frac{3}{4} \sum_j^{NN} \frac{d_{ij} - d_{ij}^0}{d_{ij}^0}. \tag{3.42}$$

Then to first-order in the $\varepsilon_{\alpha\beta}$'s we obtain:

$$V_s = V_1 + \sum_j^{NN} V_2(d_0) + \alpha_s \left(\frac{\delta\Omega}{\Omega_0}\right). \tag{3.43}$$

The on site energy of the *s*-orbital is given therefore by the unstrained on-site energy plus a term proportional to the fractional change of volume associated with the strain:

$$E_s = E_s^0 + \alpha_d \frac{\Delta\Omega}{\Omega_0}. \tag{3.44}$$

Similar arguments apply for the on-site, *p*-orbital terms. For the particular case of the p_x orbitals we get:

$$E_x = E_p^0 + \alpha_p \frac{\Delta\Omega}{\Omega_0} + \sum_j^{NN} \beta_p(d_{ij}) \left[l_{ij}^2 - 1/3\right], \tag{3.45}$$

where new TB parameters, α_p and β_p have been introduced. A similar equation holds for p_y and p_z. An important feature of this model is the inclusion of couplings between different *p*-orbitals. These are obtained from Slater-Koster relations and, together with the diagonal terms yield an on-site *p*-orbital block matrix given by:

$$\widehat{H}_p = \left(E_p^0 + \alpha_p \frac{\Delta}{\Omega_0}\right)\widehat{I} + \sum_j^{NN} \beta_p(d) \begin{bmatrix} l^2 - \frac{1}{3} & lm & ln \\ ml & m^2 - \frac{1}{3} & mn \\ nl & nm & n^2 - \frac{1}{3} \end{bmatrix}. \tag{3.46}$$

Note that a non-zero value of β_p lifts the *p*-orbital degeneracy, which is what we physically expect to happen under an applied strain. Similar parameters with similar effects are used

for the d orbitals.

$$\widehat{H}_d = \left(E_d^0 + \alpha_d \frac{\Delta}{\Omega_0}\right)\widehat{I} + \sum_j^{NN} \beta_d(d) \begin{bmatrix} l^2-\frac{1}{3} & -lm & -ln & mn & -\frac{1}{\sqrt{3}}mn \\ -ml & m^2-\frac{1}{3} & -mn & -ln & -\frac{1}{\sqrt{3}}ln \\ -nl & -nm & n^2-\frac{1}{3} & 0 & \frac{2}{\sqrt{3}lm} \\ mn & -ln & 0 & n^2-\frac{1}{3} & \frac{1}{\sqrt{3}u} \\ -\frac{1}{\sqrt{3}}mn & -\frac{1}{\sqrt{3}}ln & \frac{2}{\sqrt{3}}lm & \frac{1}{\sqrt{3}}u & -n^2+\frac{1}{3} \end{bmatrix} . \quad (3.47)$$

This model can be applied to wurtzite materials. In that case the angular terms will not be non zero even in the untrained latice. The degeneracy petween the *p* orbitals and between the *d* orbitals will therefore be lifted, as expected from the lower symmetry of the wurtzite.

The TB parameters α and $\beta_{p/d}$ are obtained from a fit to the experimental/*ab-initio* band-structure *under applied strain*. As discussed in the previous Section the changes in the band structure associated with the applied strain can be understood in terms of the deformation potentials D_1, ..., D_6. The unstrained parameters used for the fit are as given by Jancu *et al.* (78).

However our treatment of strains is very different from the one in reference (78), which only uses a Harrison-type parametrization and does not take into account the strain-induced splitting of the p orbitals.

In Table 3.5 we show the values of the TB parameters obtained from the above-mentioned fit, in GaN. In Table 3.6 we compare the experimental/*ab-initio* deformation potentials with those given by Jancu's parameters without our one-site corrections.

We see that the latter definitely improve the deformation potentials of GaN. The value of β_d however seems unusually large (more than twice the value found in other III-V). We have therefore used this set of parameters with caution in practice. We have mostly used Jancu's original parametrization and checked the critical results against our corrected set. We did not usually find significant differences for the key quantities (band gap energies). To clarify these parametrization issues we should reattempt a complete fit of the GaN and AlN band structures (including the on-site, two center integrals and power law exponents) to get a really consistent set of parameters, as has been done in reference (77) for Si and Ge. This is left as a possible option for future work.

Parameter	Ga	N (in GaN)
α_s	-5.13373	-0.57284
β_p	-1.28041	-1.28041
β_d	15.48319	15.48319

Table 3.5: Gallium and Nitrogen tight-binding parameters (in eV) obtained from fits to strained band-structures.

Parameter	Ref. (46)	Jancu *et al.* Ref. (78)	This work
a_{cx}	-4.5	-4.26	-6.87
a_{cz}	-6.8	-4.33	-6.89
$D1$	-3.7	0.67	-3.07
$D2$	4.5	4.30	4.54
$D3$	8.2	3.56	7.59
$D4$	-4.1	-1.86	-3.78
$D5$	-4.0	- 2.89	-4.27
$D6$	-5.5	-2.28	-3.03

Table 3.6: Comparison between the deformation potentials of GaN as given: by the experiment/ab-*initio* (Ref. (46), second column); as obtained by Jancu *et al.* (Ref. (78), third column); as obtained in this work (fourth column).

We do hope that this Section serve its purpose of illustrating how the TB method can be used to describe the effect of strains on the band-structure of realistic, atomistic, models of materials of technological relevance.

3.6 Application: Tight-binding modeling of strains in InP and InAs nanowires

As a first illustrative application of the tight-binding methodology used in this work we would like to take a small detour from GaN and AlN –the main material building blocks of the nanostructures considered in this Thesis– and address the effect of strains in other III-V materials, in this case InP and InAs nanowire heterostructures. The calculations presented in this Section were performed in the initial stages of my Thesis work.

Nanowires heterostructures are very attractive because of their potential advantages over quantum well heterostructures: because of the large surface/volume ratio nanowire heterostructures are able to relax strains very efficiently by distorting the surface and thus can be built from materials with very different lattice constants. The InAs/InP system has, in particular, attracted much attention (79): Resonant tunneling diodes, field effect transistor, Coulomb blockade devices, quantum memories, have all been realized with InAs nanowires splitted by InP tunnel barriers. Light has also been emitted from single InAsP quantum dots embedded in doped InP nanowires.

The residual strains in nanowire heterostures might, however, have a significant impact on their electronic and optical properties and this is the subject we investigate in this Section.

3.6.1 Electronic structure of InP barrieres in InAs nanowires

In this section, we discuss the properties of InP and InAsP barriers embedded in InAs nanowires. Their heights indeed determine the tunneling and thermionic currents through,

e.g., nanowire resonant tunneling diodes (80), or the retention time of nanowire memories (81; 82). The actual shape of these barriers depends on the piezoelectric and self-consistent electronic potentials, hence on the bias voltage and on the details of the tunneling device (doping profile, ...) (83). These potentials will be neglected in the present work,which focus on the effect of strains on the height of In(As)P conduction band barriers.

The conduction band offset between bulk, untrained InAs and InP is $\Delta_c^{\text{bulk}} \simeq 0.60$ eV (84). In an InAs/InP heterostructure, the InP barriers are put under tensile strain by the InAs layers, which tends to lower the conduction band energy E_c. The first-order shift δE_c is actually proportional to the hydrostatic strain (26; 84):

$$\delta E_c = a_c \left(\varepsilon_{xx} + \varepsilon_{yy} + \varepsilon_{zz}\right), \tag{3.48}$$

where $a_c = -5.2$ eV is the conduction band deformation potential of InP. In an InAs/InP planar (2D) heterostructure bi-axially strained to InAs ($\varepsilon_{xx} = \varepsilon_{yy} = \varepsilon_{\parallel} = 3.23\%$, $\varepsilon_{zz} = \varepsilon_{\perp} = -2.04\%$), the conduction band barrier height would therefore be:

$$\Delta_c^{\text{2D}} = \Delta_c^{\text{bulk}} + a_c \left(2\varepsilon_{\parallel} + \varepsilon_{\perp}\right) = 0.38 \text{ eV}., \tag{3.49}$$

The tight-binding model, which includes non-linear effects beyond equation (3.48), yields $\Delta_c^{\text{2D}} = 0.40$ eV. This is significantly smaller than the unstrained band offset Δ_c^{bulk}.

The conduction band barrier height in InAs/InP nanowires heterostrucuture (NWHETs) is expected to range between the 2D ($\Delta_c^{\text{2D}} = 0.4$ eV) and bulk ($\Delta_c^{\text{bulk}} = 0.6$ eV) limits. The strains are, however, much more inhomogeneous in nanowire heterostructures, especially in thin InP layers. As an illustration, the local conduction band energy $E_c(\mathbf{r})$ in an InAs/InP NWHET with $R = 10$ nm and $t_{\text{InP}} = 4$ nm is plotted in figure 3.11. $E_c(\mathbf{r})$ has been computed as the TB conduction band energy of the underlying bulk material with the same strains as in the nanowire. It is measured with respect to the conduction band edge of bulk, unstrained InAs, and therefore tends to zero far away from the InP layer. The latter is almost completely relaxed at the surface of the nanowire, but is still significantly dilated deeper inside. As a consequence, the barrier is lower along the axis of the nanowire than at its surface. In thick InP layers, which are almost free of strains, the conduction band energy is close to the unstrained value $E_c(\mathbf{r}) \simeq 0.6$ eV everywhere except around the interfaces.

To get a better understanding of tunneling in NWHETs, we can define an *effective* one-dimensional potential profile $V_c(z)$ in the spirit of the effective mass approximation (32). Let $\varepsilon_c(k_z)$ and $\Psi_{c,k_z}(\mathbf{r}) = e^{ik_z z} u_{c,k_z}(\mathbf{r})$ be the confinement energy and wavefunction for the lowest conduction subband of a *homogeneous* InAs or InP nanowire, where k_z is the longitudinal wave vector and $u_{c,k_z}(\mathbf{r})$ is periodic along the nanowire. The subband minimum at $k_z = 0$ can be characterized by its effective mass $m^*(R)$:

$$\varepsilon_c\left(k_z\right) \sim \varepsilon_c^0\left(R\right) + \frac{\hbar^2 k_z^2}{2m^*\left(R\right)}. \tag{3.50}$$

Analytical expressions for the confinement energy $\varepsilon_c^0(R)$ and effective mass $m^*(R)$ in InAs and InP nanowires have been given in reference (85). Neglecting inter-subband couplings in an effective mass-like approximation, the wavefunctions of the NWHET can be

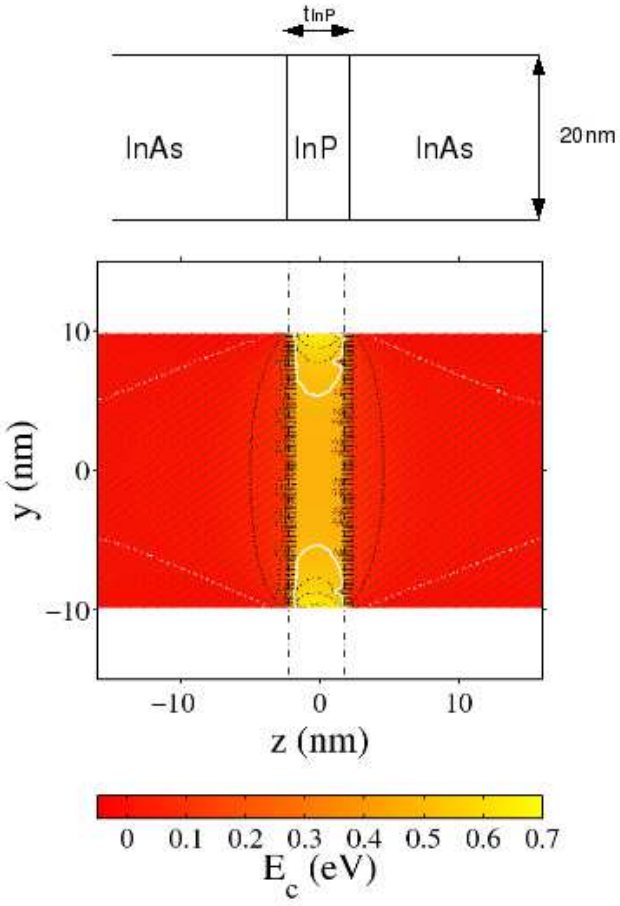

Figure 3.11: Conduction band energy $E_c(\mathbf{r})$ in an InAs/InP nanowire heterostructure - with $R = 10$ nm and $t_{\text{InP}} = 4$ nm. E_c is measured with respect to the conduction band edge of bulk, untrained InAs. The dots are the As/P atoms in the (yz) plane of the plot. The vertical, dash-dotted lines delimit the InP layer. The spacing between isolevel curves is 50 meV, the white dashed line being $E_c = 0$ and the white solid line $E_c = 0.5$ eV.

written as $\Psi(\mathbf{r}) = \varphi(z)u_{c,0}(\mathbf{r})$, where the envelope function $\varphi(z)$ satisfies the equation:

$$-\frac{d}{dz}\frac{\hbar^2}{2m^*(z)}\frac{d}{dz}\varphi(z) + \left[\varepsilon_c^0(z) + \Delta(z) + \delta V_c(z)\right]\varphi(z) = \varepsilon\varphi(z)\,, \tag{3.51}$$

$\varepsilon_c^0(z)$ and $m^*(z)$ are the conduction band edge energy and effective mass of an homogeneous InAs or InP nanowire, $\Delta(z) = 0$ in InAs, $\Delta(z) = \Delta_c^{\text{bulk}}$ in InP is the unstrained conduction band profile in the heterostructure, and $\delta V_c(z) \sim \langle u_{c,0}|\delta E_c(\mathbf{r})|u_{c,0}\rangle$ is the strain potential, the expectation value of $\delta E_c(\mathbf{r})$ being computed in an unit cell centered around z. Inter-subband couplings (that would mix $u_{c,0}$ with higher-lying modes) are expected to be small for energies ε close to the conduction band edge of the InAs nanowire.

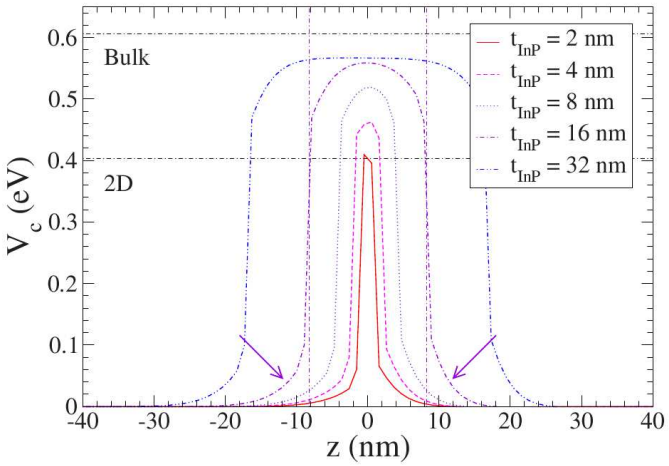

Figure 3.12: Effective potential of an InP barrier in a InAs nanowire - with radius $R = 10$ nm.

The effective potential $V_c(z) = \varepsilon_c^0(z) + \Delta(z) + \delta V_c(z)$ is plotted in figure 3.12 for InAs/InP NWHETs with radius $R = 10$ nm and various t_{InP}. The reference of energies is the conduction band edge $\varepsilon^0_{c,\text{InAs}}(R)$ of a homogeneous InAs nanowire, so that $V_c(z) \to 0$ when $z \to \pm\infty$. As expected, the barrier height is close to the 2D limit (0.4 eV) in thin layers, and tends to (but does not reach) the bulk value (0.6 eV) in thick ones. The barrier is, moreover, rounded by strain relaxation around the interfaces. There is, interestingly, a small barrier on the InAs side of the interfaces due to the transfer of (compressive) strains from the InP layer (arrows in figure 3.13). This additional barrier might hinder the transport of low-energy electrons at small bias in tunneling devices.

As pointed out before, $V_c(z)$ never reaches the bulk limit in thick layers (and actually falls below the 2D limit in the thinnest ones). Indeed, lateral confinement raises the conduction band energy $\varepsilon_c^0(R)$ faster in InAs than in InP, which lowers the effective barrier. We might therefore split the barrier height Δ_c [computed as the maximum of $V_c(z)$] in two parts:

$$\Delta_c = \left[\varepsilon^0_{c,\text{InP}}(R) - \varepsilon^0_{c,\text{InAs}}(R)\right] + \Delta_c^{\text{str}}\,, \tag{3.52}$$

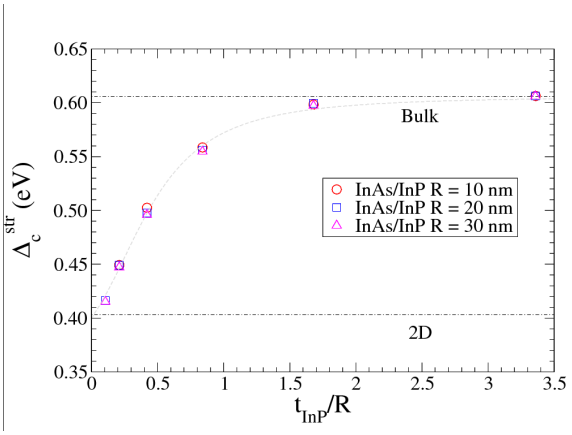

Figure 3.13: Conduction band barrier height Δ_c^{str} in InAs/InP nanowire heterostructures - as a function of t_{InP}/R. The bulk and 2D barrier heights are reported on the figure. The dashed line is equation (3.53).

where Δ_c^{str} accounts for the strained band offset and is free of quantum confinement effects. The maximum barrier height is thus $\Delta_c^{\text{max}} \simeq \varepsilon_{c,\text{InP}}^0(R) - \varepsilon_{c,\text{InAs}}^0(R) + \Delta_c^{\text{bulk}}$, i.e. about 0.57 eV for $R = 10$ nm and about 0.59 eV for $R = 20$ nm. This value lies in the experimental range (0.57–0.60 eV) deduced from the temperature dependence of the thermionic current through InAs/InP nanowire heterostructures (79; 86).

Δ_c^{str} is finally plotted in figure. 3.13 for InAs/InP NWHETs with different radius. It shows a clear dependence on t_{InP}/R, and can be fitted for $0 \leq t_{\text{InP}}/R \leq 3.5$ by:

$$\frac{\Delta_c^{\text{str}}}{\Delta_c^{\text{bulk}}} = f\left(t_{\text{InP}}/R\right) = 1 - \frac{0.34}{1 + 0.92\left(t_{\text{InP}}/R\right) + 4.15\left(t_{\text{InP}}/R\right)^{2.41}}, \tag{3.53}$$

which is plotted as a dashed line in figure. 3.13. The effects of the residual strains on the conduction band barrier are negligible when $t_{\text{InP}} \gtrsim 1.5R$. However, most tunneling devices are in the $t_{\text{InP}} \ll R$ range where the height of the barrier can be reduced by $\simeq 30\%$. This should be taken into account in the assessment and optimization of the performances of these devices (80; 81; 82).

Alloying InP with InAs provides further control over the barrier height. Thin InP barriers might, moreover, be non intentionally alloyed with the InAs nanowire. We have, therefore, also computed the conduction band height of $\text{InAs}_x\text{P}_{1-x}$ tunnel barriers embedded in InAs nanowires, as a function of their thickness t_{InAsP}, and as a function of the As concentration x. As evidenced in figure. 3.14, Δ_c^{str} nicely scales with the conduction band offset $\Delta_c^{\text{bulk}}(x) \simeq 0.6(1-x)$ eV between bulk, unstrained InAs and $\text{InAs}_x\text{P}_{1-x}$. As a matter of fact, the bowing parameters of the alloy are small, and the conduction band deformation potentials a_c of InAs and InP close enough to limit non-linear effects:

$$\Delta_c^{\text{str}} \simeq \Delta_c^{\text{bulk}}(x)\, f\left(t_{\text{InAsP}}/R\right), \tag{3.54}$$

where $f(x)$ is defined by equation. (3.53). As discussed previously around equation. (3.52),

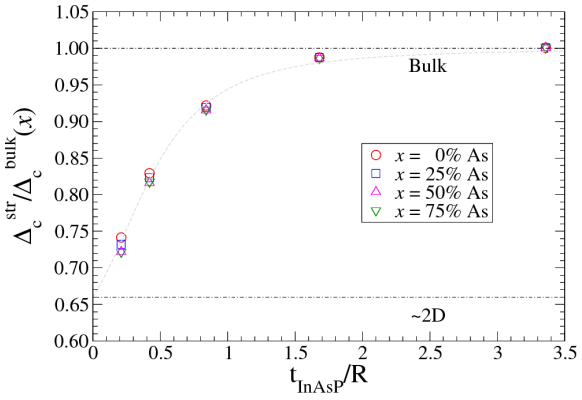

Figure 3.14: Normalized conduction band barrier InP/InAs - Normalized conduction band barrier height $\Delta_c^{\rm str}/\Delta_c^{\rm bulk}(x)$ in InAs/InAs$_x$P$_{1-x}$ nanowire heterostructures as a function of $t_{\rm InAsP}/R$, for various As concentrations x ($R = 10$ nm). The bulk and 2D ($x = 1$) barrier heights are reported on the figure. The dashed line is equation (3.53).

the actual barrier height Δ_c will be slightly lower than $\Delta_c^{\rm str}$ due to the imbalance between lateral confinement in the InAs and InAs$_x$P$_{1-x}$ segments. A linear interpolation between the confinement energies of pure InAs and InP nanowires (85), $\Delta_c \simeq (1-x)[\varepsilon^0_{c,\rm InP}(R) - \varepsilon^0_{c,\rm InAs}(R)] + \Delta_c^{\rm str}$, though crude, is nonetheless a reasonable approximation in the $R \gtrsim 10$ nm range.

Chapter 4

The GaN/AlN system

4.1 Introduction

Wide band gap nitride semiconductor are now widely used for light emission in the blue and ultraviolet range. Thanks to large band offsets, GaN/AlN heterostructures have also become promising candidates for fast telecommunication devices based on inter-subband transitions. One of the specifics of nitride heterostructures is the existence of large internal electric fields due to spontaneous polarization or strains (piezoelectricity). They might separate the electrons from the holes in Stranski-Krastanov GaN quantum dots, consequently reducing the band gap and oscillator strength (quantum confined Stark effect). It is therefore essential to understand and tailor the electric field in nitride heterostructures to suit a particular application.

In this chapter, we make a detailed description of the GaN/AlN system. As we intend to understand the electronic properties of GaN insertions in AlN nanowires, we first discuss quantum confinement in two limiting situations : GaN/AlN quantum wells ($t/R \ll 1$), and pure GaN wires ($t/R \gg 1$, t being the thickness of the GaN layer and R the radius of the wire). We then discuss the spontaneous and piezoelectric polarizations in these materials and the associated built-in electric fields, focusing again on GaN/AlN as an example. We last review the experiments on the Stark shift in GaN/AlN nanowire heterostructures. We show that simple calculations can not explain the magnitude of the experimental electric field, and that complex screening mechanisms must be introduced (Chapter 5).

4.2 Quantum confinement in GaN quantum wells and wires

4.2.1 Quantum confinement in GaN/AlN quantum wells

When the width of a quantum well is close to or smaller than the exciton Bohr radius, the band gap becomes higher than in the bulk material due to quantum confinement.

As an example we consider the quantum well formed by a GaN layer embedded in AlN as shown in figure 4.1.

We can easily solve the conduction band problem in the effective mass approximation (EMA). Taking the conduction band of GaN as the origin of energy, the EMA read:

$$-\frac{\hbar^2}{2m^*}\frac{d^2}{dz^2}\psi(z)+V\psi(z) = E\psi(z), \quad z<-\frac{t}{2} \tag{4.1}$$

$$-\frac{\hbar^2}{2m^*}\frac{d^2}{dz^2}\psi(z) = E\psi(z), \quad -\frac{t}{2}\leq z\leq\frac{t}{2} \tag{4.2}$$

$$-\frac{\hbar^2}{2m^*}\frac{d^2}{dz^2}\psi(z)+V\psi(z) = E\psi(z), \quad \frac{t}{2}<z, \tag{4.3}$$

where $V = 1.93$ eV is the conduction band offset between GaN and AlN.

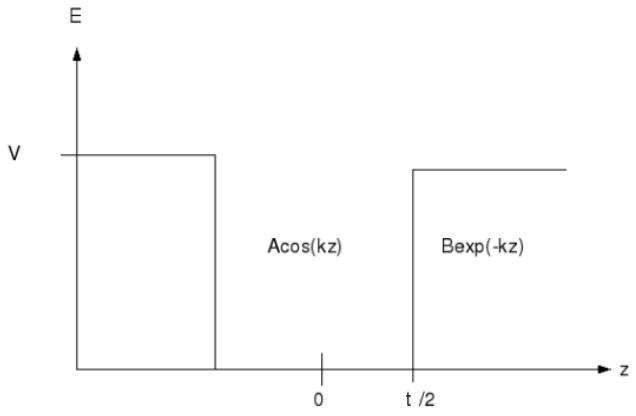

Figure 4.1: Finite well in the effective mass approximation -

The bound solutions of these equations are then in each region (for even wave functions):

$$\psi(z) = B\exp(\alpha z), \quad z<-\frac{t}{2} \tag{4.4}$$

$$\psi(z) = A\cos(kz), \quad -\frac{t}{2}\leq z\leq\frac{t}{2} \tag{4.5}$$

$$\psi(z) = B\exp(-\alpha z), \quad \frac{t}{2}<z, \tag{4.6}$$

where:

$$k = \frac{\sqrt{2m^*E}}{\hbar} \tag{4.7}$$

$$\alpha = \frac{\sqrt{2m^*(V-E)}}{\hbar} = \sqrt{k_0^2-k^2}, \tag{4.8}$$

and $k_0 = \dfrac{\sqrt{2m^*V}}{\hbar}$.

In order to proceed it is necessary to enforce appropriate boundary conditions: $\psi(z)$ and

$\frac{d}{dz}\psi(z)$ must be continuous at each interface. At the interface $z = -t/2$, the continuity of the wave function implies:

$$A\cos\left(\frac{kt}{2}\right) = B\exp\left(-\frac{\alpha t}{2}\right), \tag{4.9}$$

while the continuity of its derivative implies:

$$-kA\sin\left(\frac{kt}{2}\right) = -\alpha B\exp(\frac{-\alpha t}{2}). \tag{4.10}$$

Dividing equation 4.10 by equation 4.9, we finally get:

$$k\ \tan\left(\frac{kt}{2}\right) - \sqrt{k_0^2 - k^2} = 0. \tag{4.11}$$

The ground-state values of k and E can be obtained with a simple iterative method.

The GaN quantum well will moreover be strained by AlN. We assume for simplicity that the GaN is biaxially strained by thick AlN barriers, although this approximation can in principle only hold below the critical thickness. As discussed in chapter 3, such a strain results in a rigid shift of the conduction band by:

$$\Delta CB = ac_z\varepsilon_{zz} + ac_x(\varepsilon_{xx} + \varepsilon_{yy}), \tag{4.12}$$

where $\varepsilon_{xx} = \varepsilon_{yy} = -2.415\%$ and $\varepsilon_{zz} = 1.273\%$ were obtained with Keating's valence force field for a comparison with tight-binding calculations.

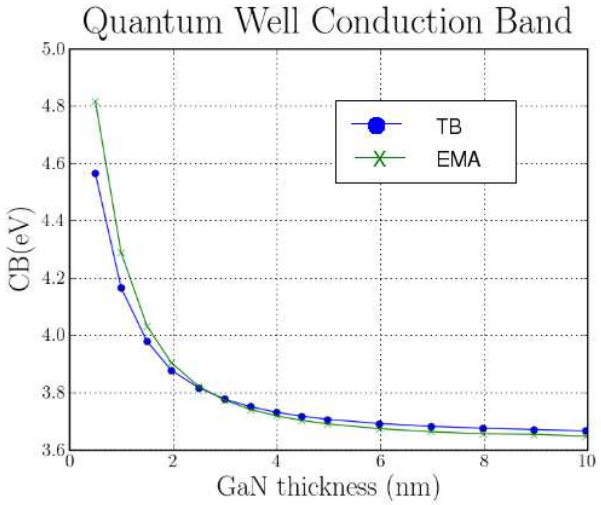

Figure 4.2: EMA and TB conduction band edge of a GaN/AlN quantum well - as a function of its thickness.

In figure 4.2 we show (blue dots) the conduction band edge calculated with the tight-binding model (Jancu's parameters). The green line (X symbols) is the conduction band

energy calculated with the EMA using the TB effective mass $m^* = 0.1976$ ($m^* = 0.2$ experimentally). As expected, the conduction band energy increases with decreasing thickness due to quantum confinement. The EMA is slightly overestimating the conduction band energy (with respect to TB) in insertions with thickness smaller than two nanometers. This results from the non-parabolicity of the conduction band at high energy, as discussed in Chapter 2. The EMA is however close to the TB result in thicker GaN insertions. The small shift between the EMA and TB energies in thick GaN insertions comes from non-linear effects beyond equation 4.12 in tight-binding.

The TB valence band edge and band gap energy of the quantum wells is plotted in figures 4.3 and 4.4. Quantum confinement is much weaker on the valence band than on the conduction band side due to the larger hole effective masses, and due to the mixing between the A, B and C bands. From figure 4.4, we conclude that quantum confinement is significant only in GaN/AlN quantum wells with thickness below 4 nm.

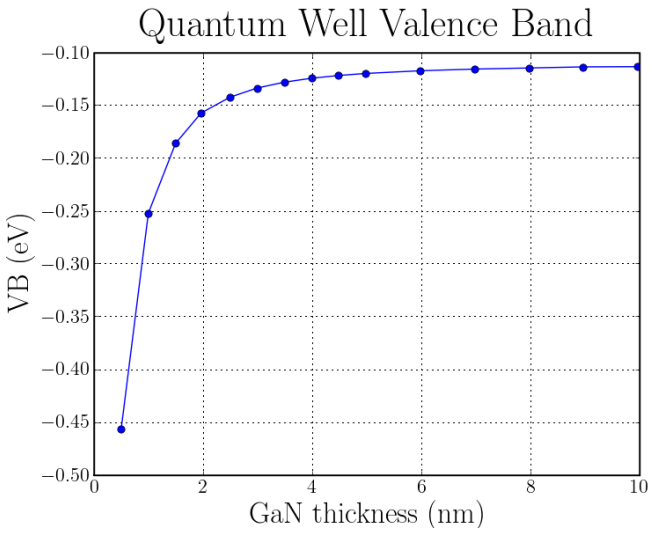

Figure 4.3: TB valence band edge of a GaN/AlN quantum well - as a function of its thickness.

4.2.2 Quantum confinement in GaN nanowires

We now study quantum confinement in GaN nanowires. The conduction band edge, valence band edge and band gap energies of homogeneous GaN nanowires are plotted as a function of their diameter in figures 4.5, 4.6 and 4.7. As in quantum wells, confinement is much stronger on the conduction than on the valence band side. It is significant for diameters below 10 nm. Most experimental GaN nanowires, whose diameter is in the 20-50 nm range, will not, therefore, show much sign of lateral quantum confinement. In particular, we expect the electronic properties of GaN/AlN nanowire heterostructures to be dominated by the "vertical" confinement along the heterostructure.

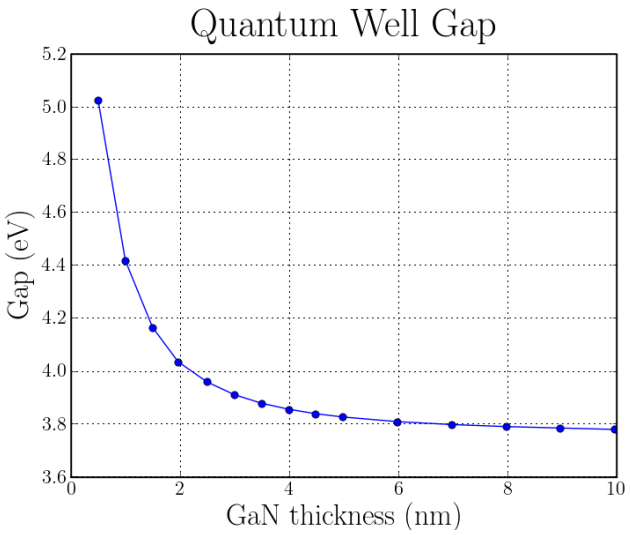

Figure 4.4: TB band gap energy of a GaN/AlN quantum well - as a function of its thickness.

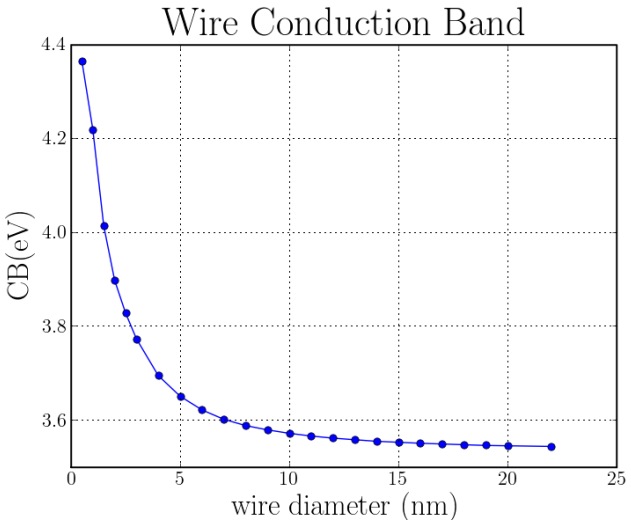

Figure 4.5: TB conduction band edge of a GaN nanowire - as a function of its diameter.

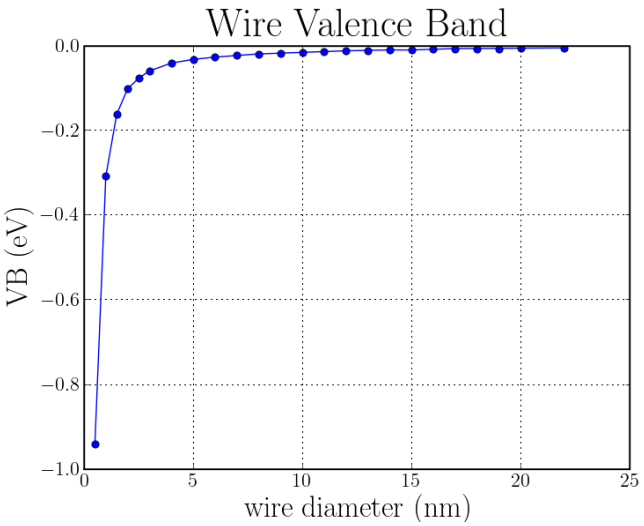

Figure 4.6: TB valence band edge of a GaN nanowire - as a function of its diameter.

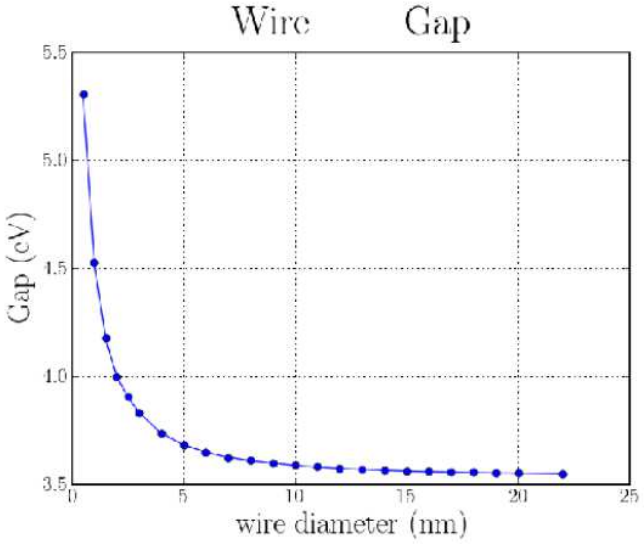

Figure 4.7: TB band gap energy of a GaN nanowire - as a function of its diameter.

4.3 The spontaneous polarization and piezoelectricty

GaN and AlN in the wurtzite phase are subject to spontaneous electric polarization. Indeed, as the first nearest neighbor bonds are not equivalent (one bond being longer than the three others), the barycentre of anions and cations do not coincide in the unit cell. This leads to the existence of a non-zero dipole density in the crystal (pyroelectricity). Strains further move the anions with respect to the cations and redistribute charge among them, thereby increasing or decreasing this dipole density (piezoelectricity). The spontaneous polarization and piezoelectricity can be responsible for large electric fields in GaN/AlN heterostructures and devices, as shown later in this section.

4.3.1 Pyroelectricity description

The symmetry of the wurtzite unit cell allows for the existence of a non-zero spontaneous polarization $\mathbf{P}_{\text{sp}}$ oriented along the c axis. The pyroelectric polarization density therefore reads:

$$\mathbf{P}_{\text{sp}} = \begin{bmatrix} 0 \\ 0 \\ P_0 \end{bmatrix} \tag{4.13}$$

where the z direction corresponds to the c axis. The values of P_0 in GaN and AlN are given in table 4.1.

4.3.2 Piezoelectricity description

The strains move the atoms and change the polarization density. The total polarization density can therefore be written $\mathbf{P} = \mathbf{P}_{\text{sp}} + \mathbf{P}_{\text{piezo}}$, where:

$$\mathbf{P}_{\text{piezo}} = \begin{bmatrix} 2e_{15}\varepsilon_{xz} \\ 2e_{15}\varepsilon_{yz} \\ e_{31}(\varepsilon_{yy} + \varepsilon_{xx}) + e_{33}\varepsilon_{zz} \end{bmatrix} \tag{4.14}$$

and e_{13}, e_{33} and e_{15} are the piezoelectric coefficients. The piezoelectric constants of GaN and AlN are also given in table 4.1.

	GaN	**AlN**	
P_0	-0.034	-0.090	C/m^2
e_{15}	-0.326	-0.418	C/m^2
e_{31}	-0.527	-0.536	C/m^2
e_{33}	0.895	1.536	C/m^2

Table 4.1: Spontaneous polarization and piezo-electric constants - of GaN and AlN (46).

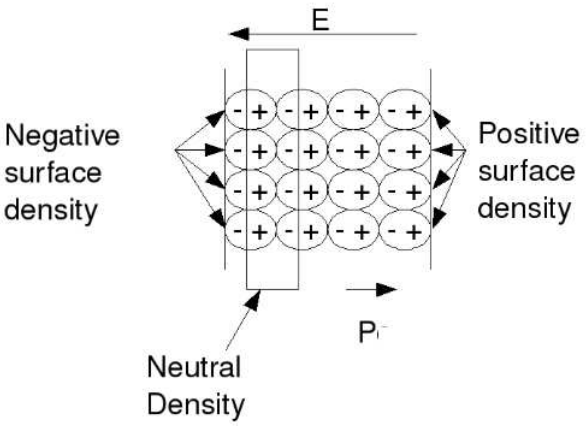

Figure 4.8: Bound charge density - equivalent to an uniform polarization.

4.3.3 Equivalent bound charge density

The distribution of dipole density due to spontaneous polarization and strains is equivalent to a distribution of "bound" charges:

$$\rho_p = -\nabla \cdot \mathbf{P} \tag{4.15}$$

wherever **P** is continuous. At surfaces and interfaces, **P** is discontinuous and must be replaced with a density of surface charges:

$$\sigma_p = (\mathbf{P}_1 - \mathbf{P}_2) \cdot \mathbf{n}_{12} \tag{4.16}$$

where $\mathbf{P}_1$ and $\mathbf{P}_2$ is the polarization density on each side of the interface, and $\mathbf{n}_{12}$ is the unit vector going from side 1 to side 2 (see figures 4.8 and 4.9).

4.4 The internal electric field: Case of GaN/AlN quantum wells

The polarization due to pyroelectricity and piezoelectricity generates an internal electric field, which has important consequences on the electronic and optical properties of GaN/AlN heterostructures.

We have investigated in section 4.2 the electronic structure of a quantum well without electric field. We now discuss the electronic structure of the same quantum well under the influence of the pyro- and piezoelectric fields, as a first illustration.

The effect of an electric field E on a GaN/AlN quantum well is depicted in figure 4.10 The field, which is oriented along the z axis, derives from a potential $V(z) = -eEz$. This potential attracts the electrons on one side of the well, and the holes on the other, effectively

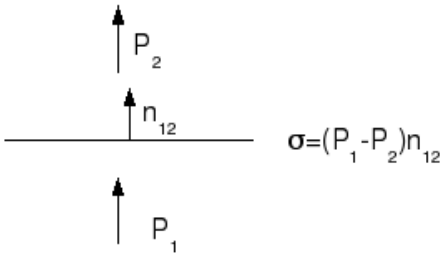

Figure 4.9: Equivalent bound charge density - at an interface between two polarized domains.

separating the two particles and shifting the band gap to lower energy. In the following subsection, we establish the expression of the electric field in the quantum well as a function of the spontaneous and piezoelectric polarizations. We then compute the band gap of the quantum well under this electric field with the tight-binding method.

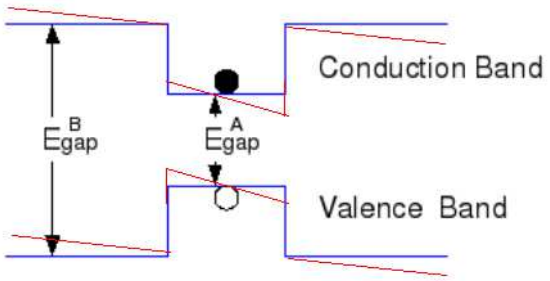

Figure 4.10: Electronic structure of an heterostructure under electric field - in blue without any potential, in red the electronic structure under the influence of a homogeneous electric field.

4.4.1 Analytical solution of Poisson's equation in GaN/AlN quantum wells

We assume that the GaN quantum well is biaxially strained by the AlN barriers. The strains are therefore zero in AlN, while in GaN:

$$\varepsilon_{xx} = \varepsilon_{yy} = \varepsilon_{\parallel} = \frac{a_{\mathrm{AlN}} - a_{\mathrm{GaN}}}{a_{\mathrm{GaN}}} = -0.0241\,, \tag{4.17}$$

$$\varepsilon_{zz} = \varepsilon_{\perp} = -\frac{2C_{13}}{C_{33}}\varepsilon_{\parallel} = 0.0129\,. \tag{4.18}$$

The spontaneous polarization in the AlN barriers is therefore:

$$P_z(\mathrm{AlN}) = P_0(\mathrm{AlN}) = -0.090\ \mathrm{C/m^2}\,, \tag{4.19}$$

while the spontaneous and piezoelectric polarization in the GaN quantum well is:

$$P_z(\mathrm{GaN}) = P_0(\mathrm{GaN}) + 2e_{31}(\mathrm{GaN})\varepsilon_{\parallel} + e_{33}(\mathrm{GaN})\varepsilon_{\perp} = -0.0029\ \mathrm{C/m^2}\,. \tag{4.20}$$

The polarization is discontinous at each GaN/AlN interface. It is thus equivalent to a distribution of surface charges:

$$\sigma = P(\mathrm{GaN}) - P(\mathrm{AlN}) = 0.093\ \mathrm{C/m^2} \tag{4.21}$$

at $z = t/2$ and:

$$\sigma = P(\mathrm{AlN}) - P(\mathrm{GaN}) = -0.093\ \mathrm{C/m^2} \tag{4.22}$$

at $z = -t/2$.

The system hence behaves as a parallel plate capacitor. The electric field $\mathbf{E} = E_z\mathbf{z}$ is therefore uniform in each layer. Using the integral version of Maxwell equation:

$$\nabla \cdot \varepsilon_0 \varepsilon \mathbf{E} = \rho(\mathbf{r})\,, \tag{4.23}$$

on a cylinder crossing the upper interfaces (Gauss theorem), we get:

$$\varepsilon_0 \left(\varepsilon_{\mathrm{AlN}} E_{\mathrm{AlN}} - \varepsilon_{\mathrm{GaN}} E_{\mathrm{GaN}}\right) = \sigma\,. \tag{4.24}$$

where $\varepsilon_{\mathrm{GaN}}$ and $\varepsilon_{\mathrm{AlN}}$ are the dielectric constants of GaN and AlN, and E_{GaN} and E_{AlN} are the electric fields in GaN and AlN. We would get the same relation on the lower interface.

We impose periodic boundary conditions on a superlattice with length L, which implies:

$$E_{\mathrm{AlN}}\,(L-t) + E_{\mathrm{GaN}} t = 0\,. \tag{4.25}$$

This yields:

$$E_{\mathrm{AlN}} = -\frac{t}{L-t} E_{\mathrm{GaN}}\,. \tag{4.26}$$

Enforcing $V\,(z = -L/2) = V(z = L/2) = 0$ instead would lead to the same relation. Finally:

$$E_{\mathrm{GaN}} = -\frac{\sigma}{\varepsilon_0}\frac{L-t}{t\varepsilon_{\mathrm{AlN}} + (L-t)\varepsilon_{\mathrm{GaN}}} \tag{4.27}$$

In the limit of a single quantum well ($L \to \infty$), we get:

$$E_{\mathrm{GaN}} = -\frac{\sigma}{\varepsilon_0 \varepsilon_{\mathrm{GaN}}} = -11.7\ \mathrm{MV/cm}\,. \tag{4.28}$$

which is a really high electric field.

4.4.2 The Stark effect in quantum wells

As explained in the introduction of this section, this large electric field separates the electrons from the holes in the quantum well. If the $[0001]$ direction points upwards, the electrons are attracted to the upper interface, and the holes to the lower one (Stark effect). They will be trapped by the electric field, respectively below the conduction band edge and above the valence band edge of the unpolarized quantum well.

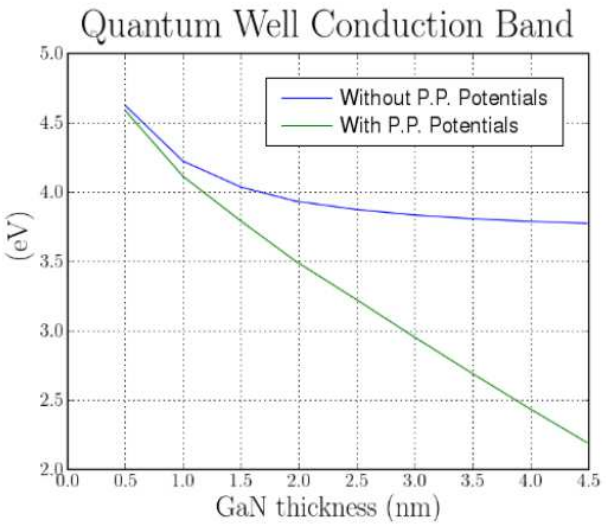

Figure 4.11: Conduction band edge of a GaN/AlN quantum well - in blue, without pyro- and piezoelectric (P.P.) potentials; in green, including the pyro- and piezoelectric potentials.

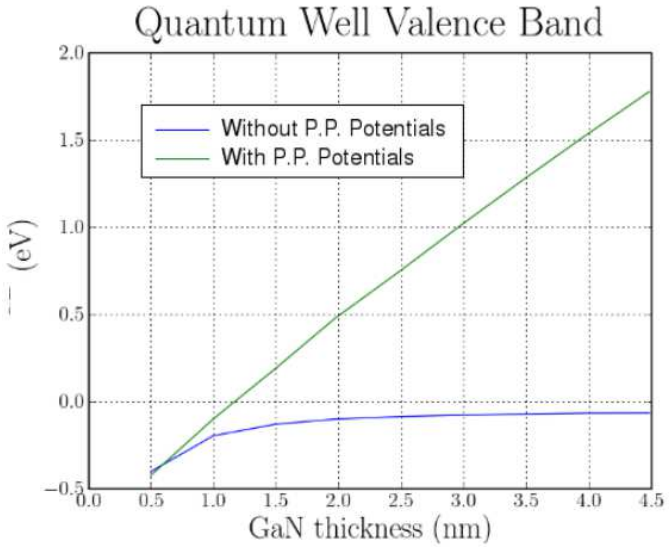

Figure 4.12: Valence band edge of a GaN/AlN quantum well - in blue, without pyro- and piezoelectric (P.P.) potentials; in green, including the pyro- and piezoelectric potentials.

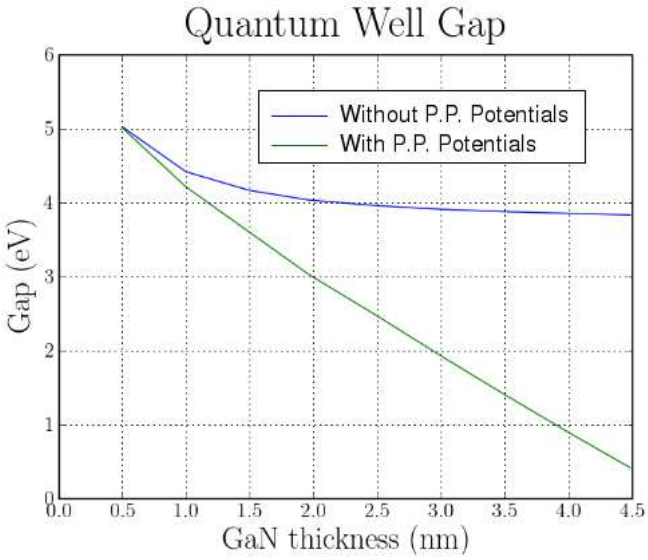

Figure 4.13: Bandgap energy of a GaN/AlN quantum well - in blue, without pyro- and piezoelectric (P.P.) potentials; in green, including the pyro- and piezoelectric potentials.

This is illustrated in figures 4.11, 4.12 and 4.13, which represent the tight-binding conduction band edge, valence band edge and band gap energy in a GaN/AlN quantum well as a function of its thickness. The pyro- and piezoelectric potential was computed with a finite differences method on a real space grid, which, in this simple case, yields the same result as the analytical treatment [equation 4.28]. The potential was then transferred from the finite difference grid to the atoms, and added to the diagonal of the tight-binding hamiltonian[1].

The bandgap energy of the GaN/AlN quantum well decreases almost linearly with the well thickness, as expected for a constant electric field. The bandgap energy is almost zero in $\simeq 4.5$ nm thick GaN layers. Although thick GaN films would practically show plastic relaxation, this calculation shows that the strong built-in electric fields in GaN/AlN heterostructures profoundly affect their electronic properties.

[1]To add this potential $V(\mathbf{r})$ to the tight-binding hamiltonian, we asume that it is varying slowly enough at the atomic scale to consider only on-site corrections:

$$\langle \varphi_{i\alpha} \mid V \mid \varphi_{j\beta} \rangle = \int d^3\mathbf{r} \varphi^*_{i\alpha}(\mathbf{r}) V(\mathbf{r}) \varphi_{j\beta}(\mathbf{r}) \tag{4.29}$$

$$\simeq \delta_{ij} \int d^3\mathbf{r} \varphi^*_{i\alpha}(\mathbf{r}) V(\mathbf{r}) \varphi_{j\beta}(\mathbf{r}) , \tag{4.30}$$

because the atomic orbitals are localized around each atom.

$$\langle \varphi_{i\alpha} \mid V \mid \varphi_{j\beta} \rangle \simeq V(\mathbf{R}_i)\delta_{ij} \int d^3\mathbf{r} \varphi^*_{i\alpha}(\mathbf{r}) \varphi_{j\beta}(\mathbf{r}) \tag{4.31}$$

$$\simeq V(\mathbf{R}_i)\delta_{ij}\delta_{\alpha\beta} , \tag{4.32}$$

4.5 The Stark effect in nanowires

This work is motivated by experimental studies performed at the laboratory of "Nanophysics and Semiconductors" also from INAC. They have measured interesting optical properties in GaN/AlN nanowire heterostructures.

The system consists of GaN quantum disks between two AlN barriers, on top of 30 nm diameter GaN pillars (see figure 4.14). These wires were grown along the c axis ([0001]) by plasma-assisted MBE under nitrogen-rich conditions (24). The thickness of the quantum disks ranges from 1 to 4 nm. As discussed in the previous sections, we expect significant vertical confinement by the heterostructure, but little lateral confinement by the nanowire. Still, as we will see, these nanostructures show features typical of one-dimensional systems, such as strain relaxation and surface effects.

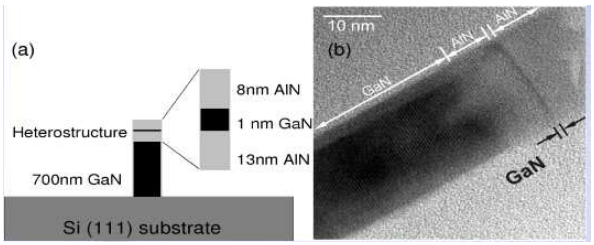

Figure 4.14: The system - a) GaN quantum disks embedded in AlN nanowires, b) HRTEM image from reference (24).

4.5.1 Experimental evidence of the Stark effect

J. Renard *et al.* (24) have measured the macrophotoluminescence spectra obtained by exciting the samples with a continuous wave frequency doubled argon laser emitting at 244 nm, at low power density (see Figure 4.15). The signal around 3.4-3.45 eV comes from the GaN base of the nanowires. The other peak is attributed to the GaN insertions. The position of this peak monotonously decreases as a function of the insertion thickness. In particular, in the thickest insertions, the photoluminescence occurs around 2.7 eV, hence at energies well below the band gap of GaN – a clear sign of the Stark effect.

The height of the GaN insertions has been measured in various samples, in order to correlate the spectral position of the emission with the insertion thickness. For that purpose, high

because the orbitals of a given atom are orthogonal. The matrix elements of the Hamiltonian thus read:

$$H_{i\alpha;j\beta} = \langle \varphi_{i\alpha} \mid H \mid \varphi_{j\beta} \rangle \tag{4.33}$$

$$H_{i\alpha;j\beta} = \langle \varphi_{i\alpha} \mid H_0 + V \mid \varphi_{j\beta} \rangle \tag{4.34}$$

$$H_{i\alpha;j\beta} = \langle \varphi_{i\alpha} \mid H_0 \mid \varphi_{j\beta} \rangle + V(\mathbf{R}_i)\delta_{ij}\delta_{\alpha\beta}\,, \tag{4.35}$$

where H_0 is the unperturbed (no electric field) tight-binding Hamiltonian. The potential V then appears as a diagonal correction.

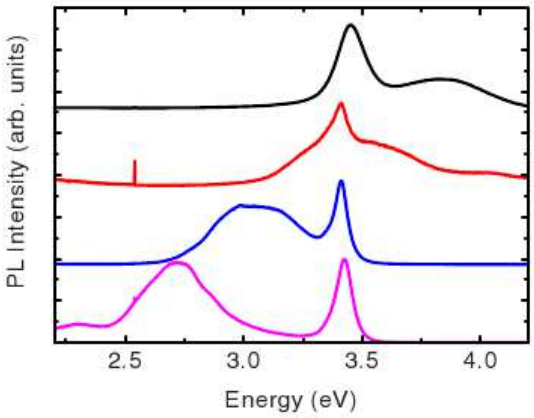

Figure 4.15: Photoluminescence spectra - Room-temperature macrophotoluminescence spectra of ensembles of NWs containing single GaN/AlN axial heterostuctures with different heights [from reference (24)].

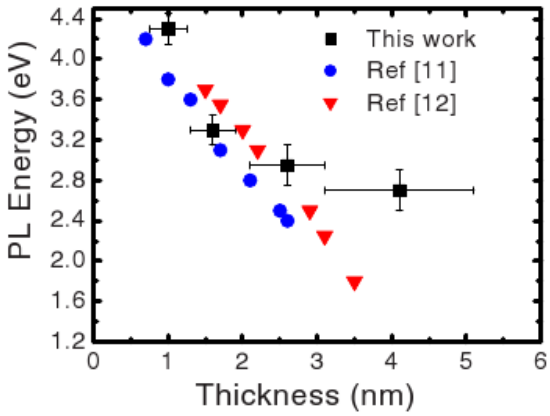

Figure 4.16: PL energy - as a function of the insertion thickness [from reference (24)]. The dots and triangles are previous results obtained on quantum wells [reference (99)] and Stranski-Krastanov quantum dots [reference (100)], respectively.

resolution transmission electron microscopy were performed on several NWs of each sample. The photoluminescence (PL) energy is plotted as a function of the insertion thickness in Figure 4.16 (squares). The dots and triangles are previous results obtained on quantum wells [reference (99)] and Stranski-Krastanov (SK) quantum dots [reference (100)]. The QW data (dots) are in good agreement with the tight-binding results of figure 4.13. The PL energy of the nanowires decreases with increasing insertion thickness, but not as much as in quantum wells and SK dots. This has been tentatively attributed to the strain relaxation in the nanowires, which decreases the piezoelectric field.

4.5.2 First simple calculations

In order to understand the behavior of the GaN/AlN nanowire heterostructures, we have computed, as a first step, the electronic properties of GaN quantum dots in infinite AlN nanowires (see Figure 4.17). The latter are oriented along the c axis and have a diameter of 30 nm. A single GaN quantum dot with a thickness from 1 to 5 nm is inserted in the middle. Periodic boundary conditions are applied on supercell with length $L \sim 80$ nm, to prevent any elastic or electrostatic interaction between the GaN layers.

4.5.2.1 Strain relaxation

The strains in the nanowires were relaxed with the Valence Force Field model introduced in Chapter 2. The elastic energy of the heterostructure was minimized with respect to the atomic positions with a conjugate gradients algorithm. The residual strains were then computed from the final atomic positions.

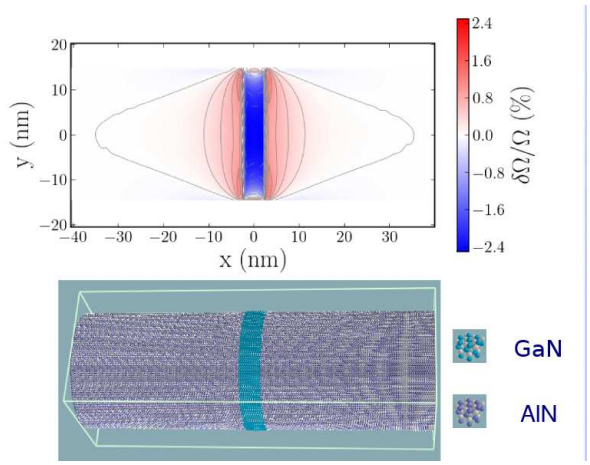

Figure 4.17: Hydrostatic deformation - in an AlN nanowire with a 5 nm thick GaN insertion.

The hydrostatic strain $\frac{\delta\Omega}{\Omega} = \varepsilon_{xx} + \varepsilon_{yy} + \varepsilon_{zz}$ is plotted in a plane containing the axis of the nanowire in figure 4.17, for a 5 nm thick GaN insertion. The hydrostatic strain is the

variation of the volume of the unit cell with respect to the unstrained material. As expected, the GaN layer is compressed by the majority material, AlN. The strains are however very inhomogeneous, being still significant at the center of the GaN layer, but almost completely relaxed at the surface. The GaN layer indeed deforms the surface of the nanowire outwards to relieve the inner strains. This transfers tensile strains to the AlN nanowire, which relax over a few nanometers on each side of the GaN insertion.

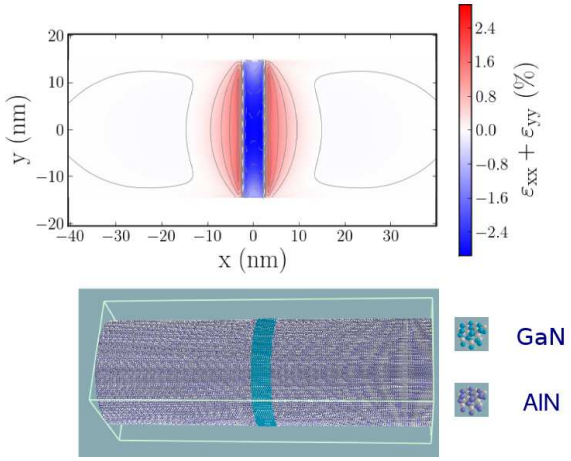

Figure 4.18: In-plane strain - $\varepsilon_{xx} + \varepsilon_{yy}$ in an AlN nanowire with a 5 nm thick GaN insertion.

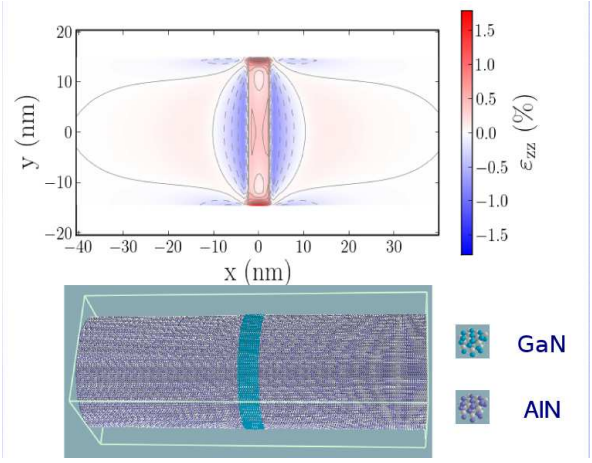

Figure 4.19: Vertical strain - ε_{zz} in an AlN nanowire with a 5 nm thick GaN insertion.

As discussed in this chapter, the built-in fields in [0001] oriented heterostructures are mostly due to the non-zero polarization along the c axis. The piezoelectric component of this polarization depends on $\varepsilon_{xx} + \varepsilon_{yy}$ and ε_{zz} (see equation 4.14). These deformations are plotted in figures 4.18 and 4.19, respectively. The in-plane strain $\varepsilon_{xx} + \varepsilon_{yy}$ shows the same

features as the hydrostatic strain. The "vertical" strain ε_{zz} is opposite to the in-plane strains, as the material compensates the compression along x and y by a dilatation along z to mitigate volume variations (i.e., hydrostatic strains). The residual in-plane strains at the center of the GaN layer, $\varepsilon_{xx} + \varepsilon_{yy} \simeq -2.8\%$, are much smaller than twice the lattice mismatch between GaN and AlN (-4.8%), which shows that strain relaxation is very efficient. We can therefore expect from figures 4.18 and 4.19 a significant reduction of the piezoelectric field due to strain relaxation.

4.5.2.2 Built-in potentials

The electrostatic potential in the nanowires was computed from the spontaneous and piezoelectric polarization with a finite differences method. The electrostatic potential in nanowires with 1 and 5 nm thick GaN insertions is shown in figure 4.20 and figure 4.21, respectively.

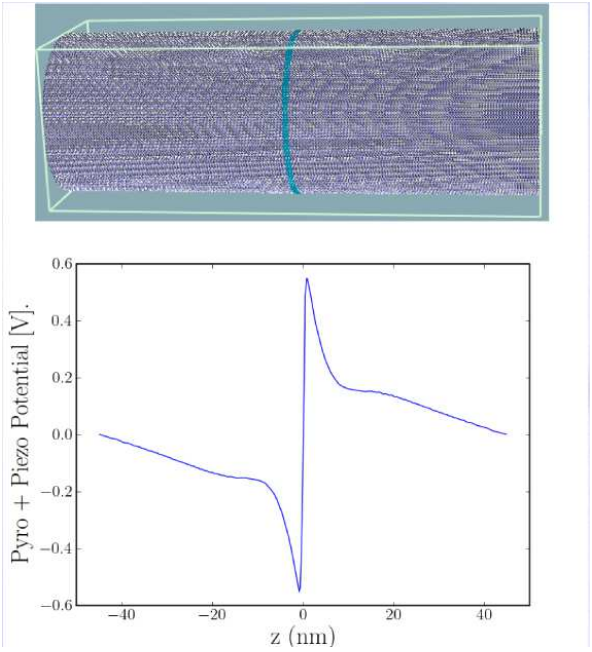

Figure 4.20: Electrostatic potential - along the axis of an AlN nanowire with a 1 nm thick GaN insertion.

The electric field is almost homogeneous in the GaN layer. It reaches ~ 10 MV/cm in 1 nm thick layers, a value very close to the 2D limit (equation 4.28). Thin GaN layers are, indeed, little relaxed and mostly behave as quantum wells. There is no significant reduction of the electric field due to finite size effects (finite cross sectional area). As expected, the electric field decreases with increasing GaN thickness, down to ~ 8 MV/cm in 5 nm thick insertions, due to strain relaxation. The electric field is much more inhomogeneous in the

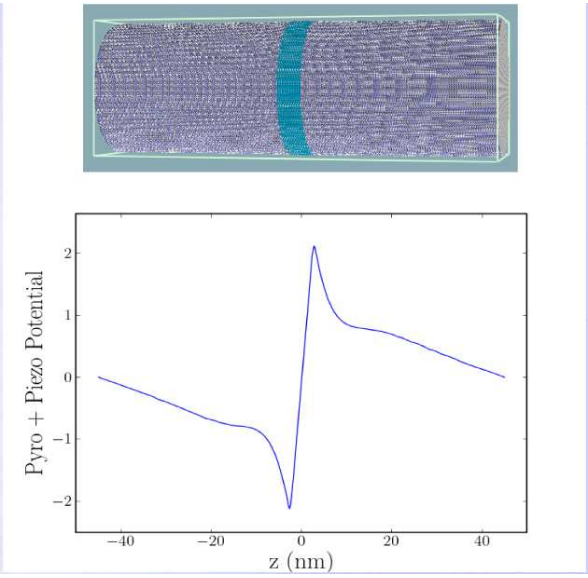

Figure 4.21: Electrostatic potential - along the axis of an AlN nanowire with a 5 nm thick GaN insertion.

AlN nanowire, and rapidly decreases away from the interfaces with the GaN layer. The tensile strains transferred from GaN to AlN indeed generate a piezoelectric polarization which tend to screen the electric field at the interfaces. We will discuss in the next paragraph the electronic structure and Stark effect in these nanowires.

4.5.2.3 Cutting the nanowires

The strains and potentials in the nanowires have been computed in 80 nm long supercells to prevent any electrostatic interaction between the GaN layers. These supercells contain around 10 millions of atoms and are, therefore, too large for tight-binding calculations (which can be routinely performed on 1-2 million atoms systems on single CPUs). Such supercells are, anyway, unnecessary long for electronic structure calculations. Due to the large band offsets between GaN and AlN, the lowest electron and hole states of the heterostructures would indeed be converged with much thinner (< 4 nm) AlN barriers on each side of the GaN layer.

Once the strains and potentials have been calculated, we therefore cut a slice in the nanowire containing the GaN layer and 4 nm thick AlN barriers on each side. The bonds broken by this operation are saturated with hydrogen atoms. The electronic structure of this slice of the nanowire is then computed with the tight-binding method, using the original electrostatic potential. We have carefully checked the convergence of the electron and hole energies with respect to the AlN barriers thickness.

4.5.2.4 Electronic structure

The slice used to compute the electronic properties of the 5 nm thick GaN layer is displayed in figure 4.22, along with the lowest energy electron and hole wave functions. As expected, the electric field separates the electron from the hole, which would decrease the oscillator strength, increase the recombination time and reduce the photoluminescence intensity.

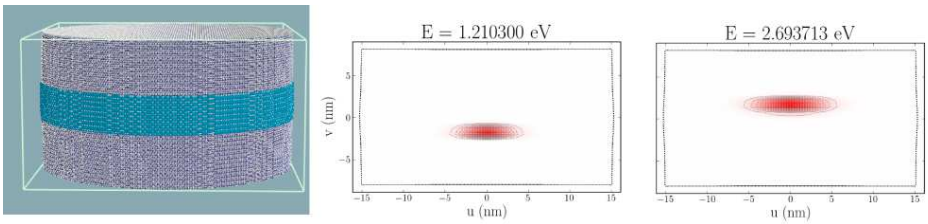

Figure 4.22: The slice of nanowire - used to compute the electronic properties of the 4 nm thick GaN layer, and the lowest hole and electron wavefunctions.

The band gap energy of the GaN layers is plotted as a function of their thickness in figure 4.23 (blue line). The experimental luminescence energies of the GaN/AlN nanowire heterostructures of reference (24) are also reported on this figure for comparison (red dots). The calculated band gap decreases much faster than the experimental band gap, being almost zero in 5 nm thick layers. We are thus strongly overestimating the electric field in the nanowires.

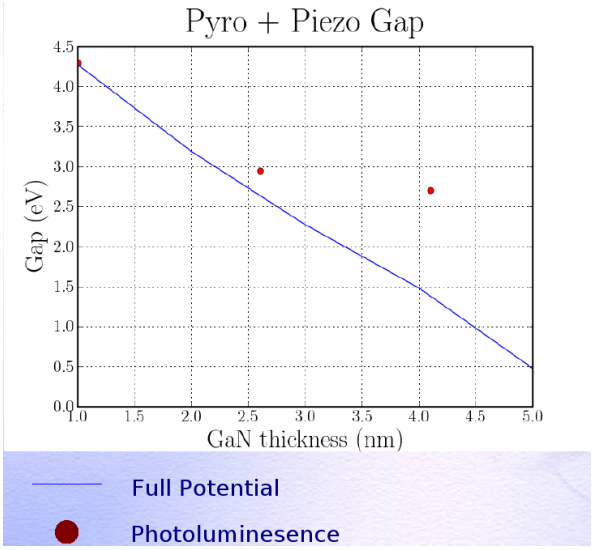

Figure 4.23: The band gap energy - of GaN layers embedded in AlN nanowires as a function of their thickness (blue line). The red dots are the experimental photoluminescence energies of reference (24)

Our present model for the Stark effect clearly misses important effects. First of all, the experimental structures feature finite size AlN barriers grown on top of a GaN pillar. This might strongly influence the electric field, due to the presence of an additional GaN/AlN interface (between the pillar and heterostructure) and of an AlN/air surface a few nanometers away from the quantum dot. Second, the large electric fields encountered in these heterostructures are likely able to transfer charges from one part of the system to an other, which would screen the electric field. In particular, the electric field can pull out electrons from surface states, which might accumulate in the GaN pillar below the heterostructure. We will investigate this scenario in detail in Chapter 5, showing that it indeed provides a clue to the reduction of the Stark effect evidenced experimentally in these nanowires.

4.5.3 GaN/AlN nanowires superlattices

As a side study we have also investigated the electronic properties of short-period GaN/AlN nanowire superlattices (figure 4.24). These superlattices are modeled as above, but with a shorter supercell length L allowing for electrostatic interactions between the GaN layers. At variance with the previous case, the wire is not cut any more, and the electronic structure is computed in the same supercell as the strains and potential.

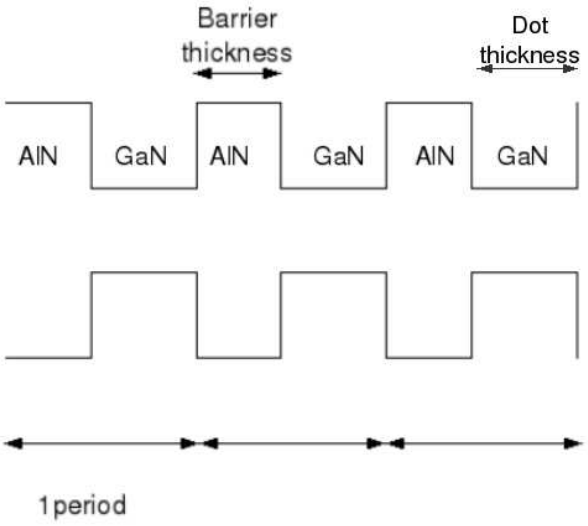

Figure 4.24: A short-period GaN/AlN superlattice - characterized by the thicknes of the GaN quantum dots and AlN barriers.

The bandgap energy of the nanowires is plotted as a function of the thickness of the GaN layers in figure 4.25, for different AlN barriers. It decreases with increasing barrier thickness, due to the electrostatic interactions between the layers. Indeed, the system behaves as a series of parallel plate capacitors (the GaN layers) brought closer and closer to each other. The

charges accumulated on a given interface tend to screen those accumulated on the neighbors, which decrease the electric field as the thickness of the barriers is reduced. This effect can directly be evidenced in equation 4.27, which shows a clear L dependence. As a consequence the Stark effect can be strongly reduced in short-period GaN/AlN nanowire superlattices.

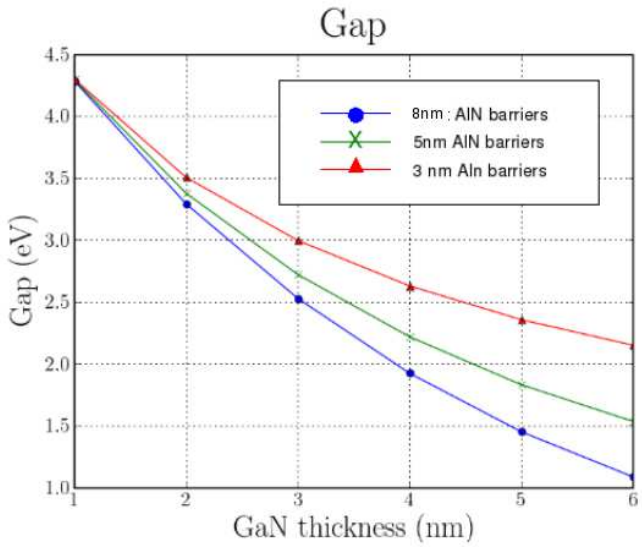

Figure 4.25: Band gap energy in GaN/AlN nanowires superlattices - as a function of the thickness of the GaN layer for different AlN barriers.

4.6 Conclusions

In this chapter, we have discussed the pyro- and piezo-electric fields in nitride materials. We have investigated their effects on GaN/AlN quantum well as an example. We have shown that the built-in electric fields could efficiently separate the electrons from the holes and reduce the band gap (Stark effect), even below the bulk value. We have then modeled the Stark effect in GaN/AlN nanowire heterostructures, in connection with recent experiments on this system. Our present approach however fails to reproduce the magnitude of the experimental electric field. This is likely due to our simplified geometry and the lack of screening mechanisms in the calculation. We will investigate these issues in detail in the next chapter.

Chapter 5

The Stark effect in GaN/AlN nanowire heterostructures

5.1 Introduction

Wide band gap nitride semiconductors are now widely used for light emission in the blue and ultraviolet range (87; 88; 89). Thanks to large band offsets, GaN/AlN heterostructures are also promising candidates for fast telecommunication devices based on intersubband transitions (90) or for high-temperature single photon emitters (91). One specific aspect of nitride heterostructures is the existence of large internal electric fields due to spontaneous electric polarization (pyroelectricity) and strains (piezoelectricity) (92). These built-in fields might transfer charges in the devices, leading for example, to the formation of two dimensional (2D) electron gases at the interfaces between GaN and AlN[1] layers (48; 93; 94; 95; 96). They might also separate electrons from holes in GaN quantum wells and Stranski-Krastanov (SK) quantum dots, thereby reducing the band gap and oscillator strength (quantum confined Stark effect) (97; 98; 99; 100).

The built-in pyro- and piezo-electric fields open a new avenue to tailor the electric and optical properties at the nanoscale, since the band-gap can be controled by modifying the geometry and composition of the quantum dot/nanowire heterostructure. It is therefore essential to understand the built-in electric field in nitride heterostructures to suit a particular application.

Whereas 2D layers usually feature a large density of dislocations, nitride nanowires offer the opportunity to make defect-free heterostructures thanks to the efficient strain relaxation associated with the large surface to volume ratio (22; 23). Single GaN quantum disks (QDs) between two AlN barriers have for example been grown on top of GaN pillars (20–50 nm diameter) with plasma-assisted molecular beam epitaxy (see figure 5.1) (56). The exciton and biexciton luminescence of 1 nm thick GaN QDs has been observed, showing the potential of such heterostructures for nitride optoelectronic devices (56). A strong red shift (below the bulk GaN band gap) has been subsequently observed for larger disk thickness, a signature of the quantum confined Stark effect (24), i.e. the optical gap decreases with the QD thickness.

[1] Such heterostructures are also formed between GaN and alloys such as $Ga_xAl_{1-x}N$. Although these alloys are also interesting, will not be considered in this Thesis.

This redshift is however smaller than expected from a comparison with GaN/AlN quantum wells ((99); see also figure 4.16 in Chapter 4).

The goal of this chapter is to explain the dependence of the optical energy gap on QD thickness and how geometrical relaxation and screening effects influence this dependence, for the case of GaN/AlN QDs. GaN/GaAlN SK dots have been modeled before with $\mathbf{k} \cdot \mathbf{p}$ or tight-binding approaches (29; 101; 102; 103; 104). The key role played by the charges transferred by band bending, which screen the electric field, has been emphasized in 2D GaN/GaAlN layers (48; 93; 94; 95; 96). In this Chapter, we model the electronic properties of GaN/AlN nanowire heterostructures in an atomistic tight-binding framework (63; 72). We first compute strains with a valence force field method (105), and then we calculate the pyro- and piezoelectric field. We account for band bending with a semi-classical Debye-Hückel approach, making no assumption about the pinning of the Fermi level, but including a distribution of surface states which act as a source or trap of carriers. We show: (*i*) that the piezoelectric component of the field can be significantly reduced by the efficient strain relaxation in the nanowire geometry ; (*ii*) that the spontaneous and piezoelectric polarizations create an electron gas at the lower GaN/AlN interface and are likely large enough to create a hole gas in the upper AlN barrier. These electron and hole gases screen the electric field in the GaN QD and reduce the Stark shift ; (*iii*) that for carefully chosen dot and barrier thicknesses (realized experimentally) the GaN QD is empty at equilibrium, consistent with the observation of exciton and biexciton transitions. We discuss the magnitude of the electric field and the electronic stucture of the QDs as a function of the dimensions of the heterostructure.

The rest of this chapter is organized as follows: We review the methods in section 5.2, then discuss the electric field in GaN/AlN nanowire heterostructures in section 5.3, where we introduce a simple 1D model for the pyro- and piezoelectric field that reproduces the main trends. We finally discuss the electronic structure of the GaN QDs and compare our calculations with the available experimental data in section 5.4, where we analyze the dependence of the electronic and optical properties of the QDs on the geometry of the heterostructures.

5.2 Methodology

In this section, we introduce the methods used to compute the structural and electronic properties of the GaN/AlN heterostructures.

Each nanowire is modeled as a 30 nm diameter and 150 nm long (106) cylindrical GaN pillar oriented along $z = [0001]$, with the heterostructure on top. The latter consists of a lower AlN barrier with thickness t_{inf}, a GaN quantum disk with thickness t_{QD} and a upper AlN barrier with thickness t_{sup} (see figure 5.1). The dangling bonds at the surface of the nanowire are saturated with hydrogen atoms.

The strains in the nanowire are computed with Keating's valence field model (39). The elastic energy of the nanowire is minimized with respect to the atomic positions using a conjugate gradients algorithm. The components of the strain tensor, $\varepsilon_{\alpha\beta}$, on each atom are then calculated from the atomic positions using a method similar (107) to reference (31).

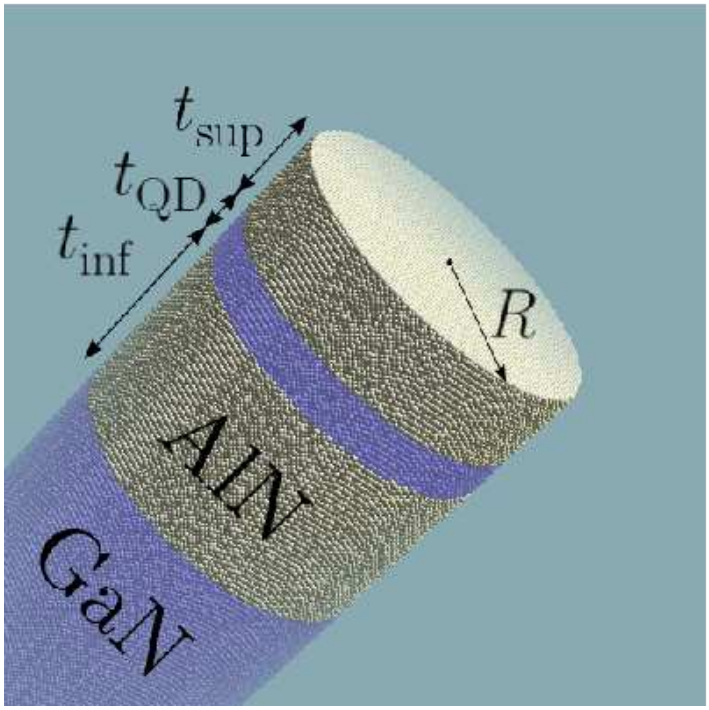

Figure 5.1: Atomistic model of a GaN/AlN nanowire heterostructure - Atomistic model of an AlN/GaN/AlN nanowire heterostructure grown on top of an GaN pillar. The radius of the nanowires is $R = 15$ nm.

The pyro- and piezoelectric polarization density, $\mathbf{P}$, is next computed from the strains on each cation (Ga or Al) :

$$\mathbf{P} = \begin{pmatrix} 0 \\ 0 \\ P_0 \end{pmatrix} + \begin{pmatrix} 2e_{15}\varepsilon_{xz} \\ 2e_{15}\varepsilon_{yz} \\ e_{31}(\varepsilon_{xx}+\varepsilon_{yy})+e_{33}\varepsilon_{zz} \end{pmatrix}, \tag{5.1}$$

where P_0 is the spontaneous polarization, and e_{13}, e_{33} and e_{15} are the piezoelectric constants of either GaN or AlN (see Table 5.1). Poisson's equation for the total, built-in potential $V_p(\mathbf{r})$ is given by

$$\kappa_0 \nabla_{\mathbf{r}} \cdot \kappa(\mathbf{r}) \nabla_{\mathbf{r}} V_p(\mathbf{r}) = \nabla_{\mathbf{r}} \cdot \mathbf{P}(\mathbf{r}), \tag{5.2}$$

and is then solved on a finite difference grid (108) (see appendix I of reference (109) for details). $\kappa(\mathbf{r})$ is the inhomogneous dielectric constant, which we take $\kappa = 9$ inside the nanowire and $\kappa = 1$ outside. The experimental static dielectric are 8.9-9.5 for GaN and 8.5 for AlN ((110)).

The large pyro- and piezoelectric field $\mathbf{E}_p = -\nabla V_p$ in the heterostructure bends the conduction and valence bands and can therefore transfer charges from one part of the system to another. It is for example known that the spontaneous polarization in GaAlN layers grown on GaN pulls out electrons from the GaAlN surface, which accumulate in a 2D electron gas at the GaN/GaAlN interface (48; 93; 94; 95; 96). These electrons leave positive charges at the GaAlN surface, which can be ionized surface donors, emptied surface states or even a hole gas. This redistribution of charges creates, in turn, an electric field opposite to $\mathbf{E}_p$, which can screen the latter to a large extent.

Here the effects of band bending have been self-consistently computed in a semi-classical Debye-Hückel approximation. The local density of electrons, $n(\mathbf{r})$, and the local density of holes, $p(\mathbf{r})$ are calculated as (111):

$$n(\mathbf{r}) = N_c F_{1/2}\left[-\beta\left(E_c - eV(\mathbf{r}) - \mu\right)\right] \tag{5.3a}$$

$$p(\mathbf{r}) = N_v F_{1/2}\left[+\beta\left(E_v - eV(\mathbf{r}) - \mu\right)\right], \tag{5.3b}$$

where N_c and N_v are the effective conduction and valence band density of states of the material at point $\mathbf{r}$, E_c and E_v are its conduction and valence band edge energies (see Table 5.1), $V(\mathbf{r})$ is the total electrostatic potential, and μ is the chemical potential or Fermi energy. $F_{1/2}$ is the Fermi integral of order one-half and $\beta = 1/(kT)$, where $T = 300$ K is the temperature. We have, additionally, assumed that the nanowires were non-intentionally n-doped, with a concentration of donor impurities (silicon, oxygen or vacancies) $N_d = 2 \times 10^{17}$ cm^{-3}. The density of ionized impurities is (111):

$$N_d^+(\mathbf{r}) = \frac{N_d}{1 + 2e^{-\beta[E_c - E_b - eV(\mathbf{r}) - \mu]}}, \tag{5.4}$$

where E_b is the binding energy of the donor, which typically ranges from a few tens to a few hundreds of meV.

As mentioned previously, surface states can play an important role in the electrostatics of nitride nanowires. They might act as a source (48; 94; 95; 96) or as a trap (113; 114) of carriers, effectively pinning the chemical potential in the band gap. Little is however known about the electronic structure of nitride surfaces (115). On one hand, density functional

	GaN	AlN
P_0 (C/m^2)	-0.034	-0.090
e_{13} (C/m^2)	-0.53	-0.54
e_{33} (C/m^2)	0.89	1.56
e_{15} (C/m^2)	-0.33	-0.42
N_v (cm^{-3})	4.6×10^{19}	4.8×10^{20}
N_c (cm^{-3})	2.3×10^{18}	6.3×10^{18}
E_v (eV)	0.0	-0.8
E_c (eV)	3.50	5.45
E_b (meV)	30	170
E_1^+ (eV)	0.25	1.00
E_2^+ (eV)	1.25	3.00
E_1^- (eV)	2.25	4.25
E_2^- (eV)	3.25	5.25

Table 5.1: The material parameters for GaN and AlN (29; 46; 112)

.

theory (DFT) calculations on reconstructed GaN and AlN surfaces (116; 117; 118; 119; 120) suggest the existence of occupied (donor-like) surface states above the valence band edge and empty (acceptor-like) surface states below the conduction band edge (as expected from simple considerations). On the other hand, the extensive literature about 2D electron gases in [0001] GaN/GaAlN heterostructures (48; 94; 95; 96) suggests the existence of dense ($\simeq 10^{13}$ cm^{-2}eV^{-1}) surface donor states only $\simeq 1.5$ eV below the conduction band of $Ga_{1-x}Al_xN$ alloys ($x \simeq 0.4$). Although the nature of these surface donors is still debated, oxygen has often been put forward (121). It is not clear however that the same picture holds for non-polar Ga(Al)N surfaces and for surfaces of *pure* AlN, where the oxide is not the same. The situation is particularly tricky in nanowires, which expose different (polar and non-polar) surfaces. For the sake of simplicity, we assume in this work the existence of a uniform density of occupied surface states in the $[E_1^+, E_2^+]$ energy range above the valence band edge, and of a uniform density of empty surface states in the $[E_1^-, E_2^-]$ energy range below the conduction band edge. The density of ionized occupied surface states is therefore:

$$N_s^+(\mathbf{r}) = kT\, D_s^+ \ln \frac{1+\frac{1}{2}e^{\beta\left[E_2^+ - eV(\mathbf{r})-\mu\right]}}{1+\frac{1}{2}e^{\beta\left[E_1^+ - eV(\mathbf{r})-\mu\right]}}, \tag{5.5}$$

while the density of electrons trapped in the empty surface states is:

$$N_s^-(\mathbf{r}) = kT\, D_s^- \ln \frac{1+2e^{-\beta\left[E_1^- - eV(\mathbf{r})-\mu\right]}}{1+2e^{-\beta\left[E_2^- - eV(\mathbf{r})-\mu\right]}}. \tag{5.6}$$

D_s^+ and D_s^- are the density of occupied and empty surface states, respectively (per unit surface and energy). The values of E_1^+, E_2^+, E_1^- and E_2^- used in this work are also reported

in Table 5.1. We have varied $D_s^+ = D_s^-$ between 5×10^{12} cm^{-2}eV^{-1} and 5×10^{13} cm^{-2}eV^{-1}. Their effects will be discussed in paragraph 5.3. We will show, in particular, that the electric field in the QD is weakly dependent on the model for the surface states up to large D_s^+ and D_s^-.

In practice, the carrier densities $n(\mathbf{r})$ and $p(\mathbf{r})$ are computed on each Ga, Al and N atom, while the surface state densities $N_s^+(\mathbf{r})$ and $N_s^-(\mathbf{r})$ are computed on each hydrogen atom. The charge on each atom is then transferred to the finite difference mesh, and Poisson's equation for the total electrostatic potential $V(\mathbf{r})$ is solved self-consistently with the Newton-Raphson method (122):

$$\begin{aligned} & \kappa_0 \nabla_{\mathbf{r}} \cdot \kappa(\mathbf{r}) \nabla_(\mathbf{r}) V(\mathbf{r}) = \nabla_{\mathbf{r}} \cdot \mathbf{P}(\mathbf{r}) \\ + \quad & \left[n(\mathbf{r}) - p(\mathbf{r}) - N_d^+(\mathbf{r}) + N_s^-(\mathbf{r}) - N_s^+(\mathbf{r}) \right] e \,. \end{aligned} \tag{5.7}$$

The chemical potential μ is adjusted to ensure overall charge neutrality of the nanowire.

Finally, the electronic structure of the GaN QD in the potential $V(\mathbf{r})$ is computed with a $sp^3d^5s^*$ tight-binding model (34; 78; 123; 124). In order to access the relevant states directly, a slice containing the GaN QD and 4 nm of each AlN barrier is cut from the nanowire. The bonds broken by this operation are saturated with hydrogen atoms, and a few conduction and valence band states are computed with a Jacobi-Davidson algorithm (125; 126). The convergence of the electronic structure of the QD with respect to the thickness of the AlN barriers has been checked.

5.3 The built-in electric field in GaN/AlN nanowire heterostructures

In this section we discuss the built-in pyro- and piezo-electric electric fields in GaN/AlN nanowire heterostructures emphasizing/enquiring about how self-consistent screening by charge carriers modifies the built-in fields. It will be shown that screening effects can substantially reduce these fields, thus resulting in a reduction of the Stark red-shift. This reduction is associated with the formation of a 2D layer of holes at the terminating surface of the heterostructure. These screening effects turn out to be essential to explain the experimental results obtained in reference (24).

For definitiveness we will first consider a particular case of a nanowire heterostructure with $t_{\mathrm{QD}} = 4$ nm and $t_{\mathrm{inf}} = t_{\mathrm{sup}} = 8$ nm as geometrical parameters (See figure 5.1) which clearly illustrates the redshift reduction associated with self-consistent screening effects. We then propose a simplified model that reproduces these trends fairly well.

Finally we will investigate the effect of varying the geometrical parameters of our heterostructure model. We will see how the length of the barriers sourronding the quantum dot becomes an important factor, in order of keep the quantum dot clean of free carriers.

5.3.1 Example: AlN (8 nm)/GaN (4 nm)/AlN (8 nm)

We focus as an illustration on a 30 nm diameter nanowire with a $t_{\mathrm{QD}} = 4$ nm thick GaN QD and $t_{\mathrm{inf}} = t_{\mathrm{sup}} = 8$ nm thick AlN barriers. We set $D_s^+ = D_s^- = 10^{13}$ cm^{-2}eV^{-1}.

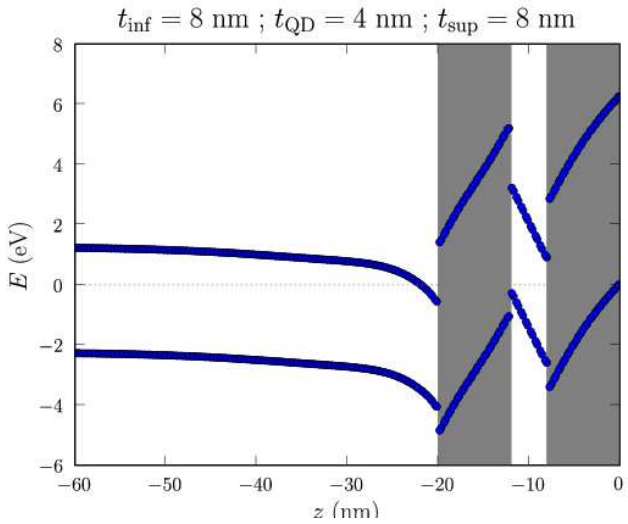

Figure 5.2: Conduction and valence band-edge energies of a AlN (8 nm)/GaN (4 nm)/AlN (8 nm) nanowire heterostructure. - The conduction band-edge energy, $\varepsilon_c(\mathbf{r}) = E_c - eV(\mathbf{r})$, and the valence band-edge energy, $\varepsilon_v(\mathbf{r}) = E_v - eV(\mathbf{r})$, along the axis of a nanowire with $t_{\text{QD}} = 4$ nm and $t_{\text{inf}} = t_{\text{sup}} = 8$ nm. The reference of energy is the chemical potential $\mu = 0$. The position of the AlN barriers is outlined in gray, and the top surface is at $z = 0$.

The conduction band edge energy $\varepsilon_c(\mathbf{r}) = E_c - eV(\mathbf{r})$ and the valence band edge energy $\varepsilon_v(\mathbf{r}) = E_v - eV(\mathbf{r})$ are plotted along the axis of the nanowire in figure 5.2. The reference of energy for this plot is the chemical potential $\mu = 0$. The top of the nanowire is located at $z = 0$ and the position of the AlN barriers is outlined in gray.

The band discontinuities at the GaN/AlN interfaces are clearly visible. The heterostructure undergoes a strong vertical electric field, which is almost homogeneous in the AlN barriers and in the GaN QD. The latter is empty of carriers (electrons and holes). The chemical potential is however pinned at the valence band edge at the top surface of the nanowire, and crosses the conduction band at the interface with the GaN pillar. Electrons therefore accumulate in the GaN pillar, while holes accumulate in the upper AlN barrier.

This redistribution of charges follows from the pyro- and piezoelectric polarizations. Leaving aside piezoelectricity for the moment, the spontaneous polarization in GaN is $P_z = -0.034$ C/m^2, while the spontaneous polarization in AlN is $P_z = -0.090$ C/m^2. This polarization is equivalent to a distribution of charges $\sigma = -0.090$ C/m^2 at the top surface, and $\sigma = \pm(0.090 - 0.034) = \pm 0.056$ C/m^2 at each GaN/AlN interface. Such a charge distribution, if unscreened, would create huge vertical electric fields and potentials of the order of 10 to 20 V in the nanowire (see figure 5.3).

The pyro- and piezoelectric field however bends the conduction and valence bands and tends to draw positive charges at the top of the nanowire, which screen the polarization. The potential actually rises the occupied surface states of the upper AlN barrier above the

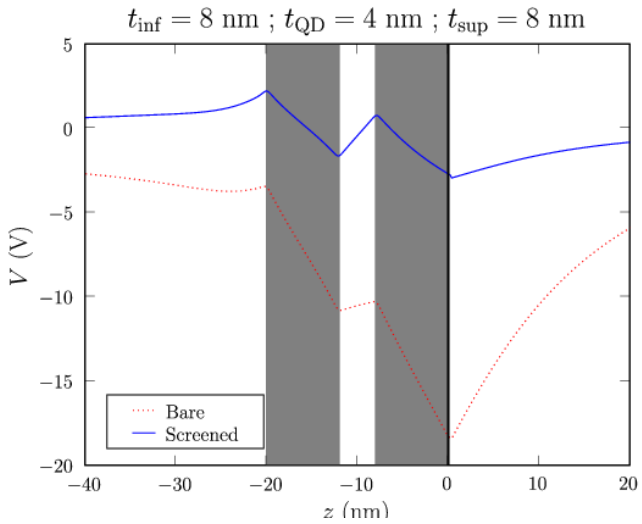

Figure 5.3: unscreened and screened pyro- and piezoelectric potentials - The bare (unscreened) and screened pyro- and piezoelectric potentials along the axis of the nanowire ($t_{QD} = 4$ nm, $t_{inf} = t_{sup} = 8$ nm). The position of the AlN barriers is outlined in gray, and the top surface is at $z = 0$.

Fermi energy. They therefore empty, leaving positive charges at the surface and releasing electrons in the GaN pillar. At moderate electric field, the surface states would be able to provide enough charge to reach equilibrium, and the chemical potential would lie in the band gap at the top AlN surface. Here the electric field is however large enough to empty the $N_{tot}^{+} = D_s^{+}(E_2^{+} - E_1^{+}) = 2 \times 10^{13}$ cm^{-2} occupied surface states. The chemical potential then sinks into the valence band; a gas of holes forms at the top surface and provides the missing charges.

According to this picture, the charge in the system is mostly distributed at the top AlN surface and at the GaN/AlN interfaces. As a consequence, the electric field is typical of a series of parallel plate capacitors, being almost homogeneous in the GaN QD and AlN barriers. This is further emphasized in figure 5.4, which represents the electrostatic potential $V(\mathbf{r})$ in a (xz) plane containing the axis of the nanowire. The equipotential lines are indeed parallel to the interfaces. Finite size electrostatic effects are therefore limited in the GaN QD and barriers in this range of dimensions.

The effective density of states in the conduction and valence bands of GaN and AlN are large enough to "lock" the potential at the interface with the GaN pillar and at the top surface (as a small variation of potential leads to exponential variations of the charge densities once the Fermi energy is in the bands). Hence,

$$\mu \simeq E_v(\text{AlN}) - eV(z = 0) \tag{5.8a}$$

at the top surface, and

$$\mu \simeq E_c(\text{GaN}) - eV(z = -t_{het}) \tag{5.8b}$$

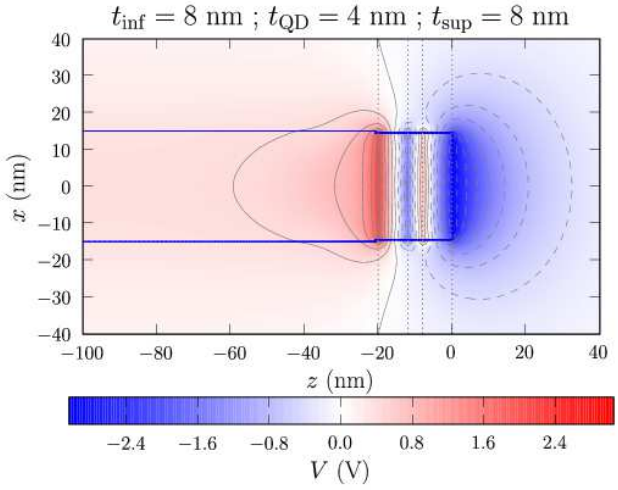

Figure 5.4: The electrostatic potential - $V(\mathbf{r})$ in the (xz) plane containing the axis of the nanowire ($t_{QD} = 4$ nm, $t_{inf} = t_{sup} = 8$ nm). The GaN and AlN layers are delimited by dotted lines.

at the interface $z = -t_{het} = -(t_{inf} + t_{QD} + t_{sup})$ with the GaN pillar. The voltage drop $\Delta V = V(z = -t_{het}) - V(z = 0)$ across the heterostructure is therefore:

$$\begin{aligned} e\Delta V &\simeq E_c(\text{GaN}) - E_v(\text{AlN}) \\ &\simeq E_g(\text{GaN}) + E_v(\text{GaN}) - E_v(\text{AlN}) \,. \end{aligned} \tag{5.9}$$

The voltage drop across the heterostructure is thus primarily defined by the band gap $E_g(\text{GaN})$ of GaN and the valence band offset between GaN and AlN once the Fermi energy is pinned in the valence band of AlN at the top surface. The validity of this assumption will be discussed in the next paragraphs.

5.3.2 A simple 1D model

We can derive a simple 1D model for the electric field E_{QD} in the GaN QD from the above observations. For that purpose, we neglect finite size effects ($R \to \infty$) and doping. We assume that the polarization is homogeneous in the lower AlN barrier ($P_z = P_{inf}$), GaN quantum disk ($P_z = P_{QD}$) and upper AlN barrier ($P_z = P_{sup}$, see figure 5.5). This polarization is equivalent to a charge density $\sigma_{sup} = \Delta P_{sup} = P_{QD} - P_{sup}$ on the upper QD interface and $\sigma_{inf} = -\Delta P_{inf} = -(P_{QD} - P_{inf})$ on the lower QD interface. We also assume that the difference of potential ΔV across the heterostructure is set by band structure effects [equation (5.9) or equivalent if other pinning of the Fermi level]. The electric field is then homogeneous in

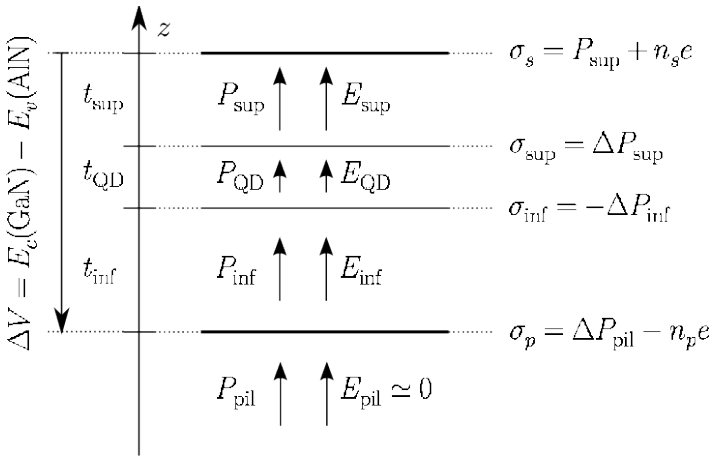

Figure 5.5: The 1D model used for the analysis of the electric field in the GaN QD. -

each layer and fulfills the continuity and integral equations:

$$\kappa_0 \kappa \left(E_{\mathrm{inf}} - E_{\mathrm{QD}}\right) = \Delta P_{\mathrm{inf}} \tag{5.10a}$$

$$\kappa_0 \kappa \left(E_{\mathrm{sup}} - E_{\mathrm{QD}}\right) = \Delta P_{\mathrm{sup}} \tag{5.10b}$$

$$t_{\mathrm{inf}} E_{\mathrm{inf}} + t_{\mathrm{QD}} E_{\mathrm{QD}} + t_{\mathrm{sup}} E_{\mathrm{sup}} = \Delta V\,. \tag{5.10c}$$

We therefore get:

$$E_{\mathrm{QD}} = -\frac{1}{\kappa_0 \kappa} \frac{t_{\mathrm{inf}} + t_{\mathrm{sup}}}{t_{\mathrm{het}}} \Delta \bar{P} + \frac{\Delta V}{t_{\mathrm{het}}} \tag{5.11}$$

where:

$$\Delta \bar{P} = \frac{t_{\mathrm{inf}} \Delta P_{\mathrm{inf}} + t_{\mathrm{sup}} \Delta P_{\mathrm{sup}}}{t_{\mathrm{inf}} + t_{\mathrm{sup}}} \tag{5.12}$$

is an average polarization discontinuity at the interfaces of the QD. Additionally, the electric field in the barriers is:

$$E_{\mathrm{inf}} = \frac{1}{\kappa_0 \kappa} \left[\Delta P_{\mathrm{inf}} - \frac{t_{\mathrm{inf}} + t_{\mathrm{sup}}}{t_{\mathrm{het}}} \Delta \bar{P} \right] + \frac{\Delta V}{t_{\mathrm{het}}} \tag{5.13a}$$

$$E_{\mathrm{sup}} = \frac{1}{\kappa_0 \kappa} \left[\Delta P_{\mathrm{sup}} - \frac{t_{\mathrm{inf}} + t_{\mathrm{sup}}}{t_{\mathrm{het}}} \Delta \bar{P} \right] + \frac{\Delta V}{t_{\mathrm{het}}}\,. \tag{5.13b}$$

The above equations hold as long as the QD is empty – which is also often desired experimentally. Neglecting quantum confinement in a first approximation, the QD is empty as long as the conduction band edge is above the Fermi energy, and the valence band edge below the Fermi energy throughout the dot. Assuming $E_{\mathrm{QD}} < 0$ (which is the case here), the QD is therefore free from holes if $E_v(\mathrm{GaN}) - eV(z = -t_{\mathrm{sup}} - t_{\mathrm{QD}}) < \mu$, and free from electrons if $E_c(\mathrm{GaN}) - eV(z = -t_{\mathrm{sup}}) > \mu$. Using Eqs. (5.8), (5.9) and (5.13), these conditions

respectively translate into the following constraints on $t_{\rm inf}$ and $t_{\rm sup}$:

$$t_{\rm inf} < \frac{E_{\rm g}({\rm GaN})}{eE_{\rm inf}} \tag{5.14a}$$

$$t_{\rm sup} < \frac{\Delta V}{E_{\rm sup}}\,. \tag{5.14b}$$

Assuming fixed pyro- and piezoelectric polarizations, $E_{\rm inf}$ and $E_{\rm sup}$ are independent on $t_{\rm inf}$ and $t_{\rm sup}$ for given $t_{\rm QD}$ and $t_{\rm het}$. Equations (5.14) then show that the QD can be empty only in a finite range of positions within the heterostructure. The QD is indeed filled with electrons if it is too far from the surface, and filled with holes if it is too far from the pillar. The QD might actually never be empty if it is too thick. Note, however, that quantum confinement will practically hinder the charging of the QDs by rising the electron and hole energies. The above constraints thus provide safe bounds for the design of nanowire heterostructures.

Equations (5.11) and (5.13) also give an estimate of the charge densities σ_s and σ_p accumulated at top surface and interface with the pillar, respectively. The continuity equation for the electric field indeed reads at this interface:

$$\kappa_0\kappa\left(E_{\rm inf}-E_{\rm pil}\right)=\sigma_p\,, \tag{5.15}$$

where $E_{\rm pil}$ is the electric field in the pillar. Since $E_{\rm pil}$ decreases rapidly away from the interface,

$$\sigma_p \simeq \kappa_0\kappa E_{\rm inf}\,. \tag{5.16}$$

Assuming that the tip of the nanowire is charge neutral at equilibrium, we then get:

$$\sigma_s \simeq -\left(\sigma_p-\Delta P_{\rm inf}+\Delta P_{\rm sup}\right)\,. \tag{5.17}$$

We can further split σ_s and σ_p into polarization and induced charges:

$$\sigma_p = \Delta P_{\rm pil}-n_p e \tag{5.18a}$$

$$\sigma_s = P_{\rm sup}+n_s e\,, \tag{5.18b}$$

where $\Delta P_{\rm pil}=P_{\rm pil}-P_{\rm inf}$, n_p is the density of the electron gas at the interface with the pillar, and n_s is the density of charges (ionized surface states+holes) at the top surface. The latter thus finally read:

$$n_p e \simeq P_{\rm pil}-P_{\rm QD}+\frac{t_{\rm inf}+t_{\rm sup}}{t_{\rm het}}\Delta\bar{P}-\kappa_0\kappa\frac{\Delta V}{t_{\rm het}} \tag{5.19a}$$

$$n_s e \simeq -P_{\rm QD}+\frac{t_{\rm inf}+t_{\rm sup}}{t_{\rm het}}\Delta\bar{P}-\kappa_0\kappa\frac{\Delta V}{t_{\rm het}}\,. \tag{5.19b}$$

Note that $t_{\rm het}$ must be large enough for the electron gas to form at the interface with the pillar ($n_p>0$) (94), but this is usually not limiting the design of the heterostructure.

We can get a rough estimate of $E_{\rm QD}$, n_p and n_s by neglecting piezoelectricity [$P_{\rm inf}=$

$P_{\text{sup}} = P_0(\text{AlN})$, $P_{\text{pil}} = P_{\text{QD}} = P_0(\text{GaN})$]. We then get from equations (5.11) and (5.19b):

$$E_{\text{QD}} = -\frac{1}{\kappa_0\kappa}\frac{t_{\text{inf}}+t_{\text{sup}}}{t_{\text{het}}}\left[P_0(\text{GaN})-P_0(\text{AlN})\right]+\frac{\Delta V}{t_{\text{het}}} \tag{5.20a}$$

$$n_p e = \frac{t_{\text{inf}}+t_{\text{sup}}}{t_{\text{het}}}\left[P_0(\text{GaN})-P_0(\text{AlN})\right]-\kappa_0\kappa\frac{\Delta V}{t_{\text{het}}} \tag{5.20b}$$

$$n_s e = -\frac{t_{\text{QD}}P_0(\text{GaN})+\left(t_{\text{inf}}+t_{\text{sup}}\right)P_0(\text{AlN})}{t_{\text{het}}}-\kappa_0\kappa\frac{\Delta V}{t_{\text{het}}}\,. \tag{5.20c}$$

As a simple example, the pyroelectric field in a 4 nm thick QD embedded in an infinitely long nanowire ($t_{\text{het}} \to \infty$) would be $|E_{\text{QD}}| = 7.03$ MV/cm. In a finite heterostructure with $t_{\text{het}} = 20$ nm, the induced charges screen this field down to $|E_{\text{QD}}| = 3.47$ MV/cm. The density of the electron gas at the interface with the GaN pillar is then $n_p = 1.73 \times 10^{13}$ cm^{-2}, while the total density of charges (surface states+holes) at the top surface is $n_s = 3.85 \times 10^{13}$ cm^{-2}. Therefore, the Fermi level is actually pinned in the valence band of AlN as long as the total (donor) surface states density is lower than $N^+_{\text{crit}} = 3.85 \times 10^{13}$ cm^{-2}. This critical density, although large, is yet not unreasonable for bare nanowire surfaces. We will however give further evidence in paragraph 5.4 that the Fermi level is pinned at (or at least close to) the valence band edge of AlN.

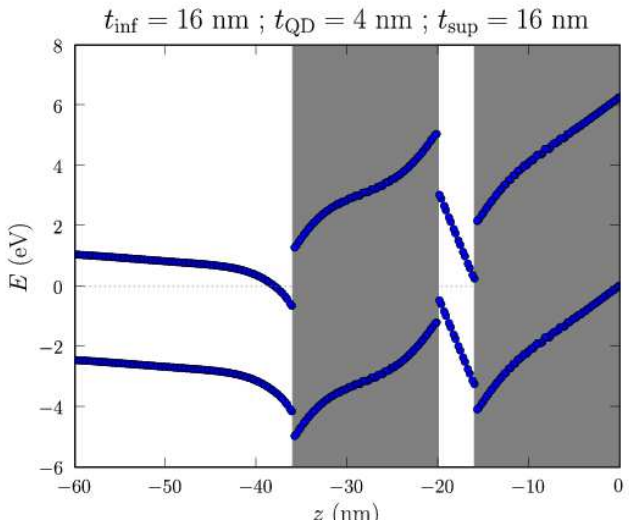

Figure 5.6: Conduction and valence band-edge energies of a AlN (16 nm)/GaN (4 nm)/AlN (16 nm) nanowire heterostructure. - The reference of energy is the chemical potential $\mu = 0$. The position of the AlN barriers is outlined in gray. The electric field is not constant in the barriers due to the inhomogeneous strains and piezoelectricity.

We have tested this simple 1D model against the numerical solution of equations (5.3)–(5.7). It gives an excellent account of the electric field in the QD when $t_{\text{het}} \lesssim 2R$. The effects of the non-intentional doping are indeed negligible with respect to the amount of charges

transferred by the pyro- and piezoelectric field. This model however tends to overestimate n_p (as the electric field in the pillar actually decreases over tens of nanometers) and thus n_s (by around 25% in the above example). Also, the piezoelectric polarization and field become inhomogeneous in thick heterostructures, as the strains are maximum at the interfaces and relax in between (72; 109) (see figure 5.6). The 1D model above is nonetheless very helpful in understanding trends and guiding the design of nanowire heterostructures.

5.3.3 Discussion

The amplitude of the electric field $|E_{\mathrm{QD}}|$, computed with equations. (5.3)–(5.7) as the difference of potential along the QD axis divided by t_{QD}, is plotted in figure. 5.7a as a function of t_{inf} and t_{sup} ($t_{\mathrm{QD}} = 4$ nm). As expected from equation. (5.20a), the electric field increases with the total thickness t_{het} of the heterostructure, and ranges from $\simeq 3.5$ MV/cm for $t_{\mathrm{het}} \simeq 12$ nm to > 7 MV/cm for $t_{\mathrm{het}} = 36$ nm. The electric field is slightly higher than expected from the spontaneous polarization, and does not fulfill the symmetry relation $E_{\mathrm{QD}}(t_{\mathrm{inf}}, t_{\mathrm{sup}}) = E_{\mathrm{QD}}(t_{\mathrm{sup}}, t_{\mathrm{inf}})$ due to piezoelectricity. This is further emphasized in figure 5.7b, which represents the average $\Delta\bar{P}$ obtained by inverting equation (5.11) with the data of figure 5.7a. Three horizontal lines are also plotted on this figure for reference. $\Delta P_{\mathrm{pyro}} = 0.056$ C/m^2 is the spontaneous polarization discontinuity at the GaN/AlN interface, which should provide a lower bound for $\Delta\bar{P}$. $\Delta P_{\mathrm{GaN}} = 0.105$ C/m^2 is the spontaneous and piezoelectric polarization discontinuity in an heterostructure biaxially strained onto GaN, and $\Delta P_{\mathrm{AlN}} = 0.093$ C/m^2 is the polarization discontinuity in an heterostructure biaxially strained onto AlN, which are the expected limits for thin and thick barriers, respectively. The actual $\Delta\bar{P}$ lies between these bounds, as an evidence for piezoelectricity. The piezoelectric field, though still significant, is lower than in a 2D AlN/GaN/AlN quantum well, due to strain relaxation. The variations of $\Delta\bar{P}$ result from a complex interplay between strain relaxation and charging (see discussion below). It is nonetheless worthwhile to note that a very good approximation to the electric field can be obtained with a constant $\Delta\bar{P} \simeq 0.077$ C/m^2 (for given t_{QD} and R) in a wide range of t_{inf} and t_{sup}. The value of $\Delta\bar{P}$ slightly increases with decreasing t_{QD}, up to $\Delta\bar{P} \simeq 0.082$ C/m^2 for $t_{\mathrm{QD}} = 1$ nm.

As discussed above, the QDs might not be empty if they are are too far from the surface or from the pillar. equations (5.3)–(5.7) do not, however, properly take quantum confinement into account. We have therefore refined the assessment of the charge state of the QDs with the tight-binding model: we have tentatively assumed that the QDs were empty (setting $N_{\mathrm{v}} = N_{\mathrm{c}} = 0$), and checked the position of the tight-binding band edges with respect to the Fermi energy. We find that all the QDs of figure 5.7 are actually empty, except those with $t_{\mathrm{sup}} = 4$ nm and $t_{\mathrm{inf}} \geq 8$ nm, which are filled with holes. As expected from equation (5.19b), the total charge density in the AlN barriers increases with t_{het}, from $n_s = 2.39 \times 10^{13}$ cm^{-2} for $t_{\mathrm{inf}} = t_{\mathrm{sup}} = 4$ nm, to $n_s = 3.54 \times 10^{13}$ cm^{-2} for $t_{\mathrm{inf}} = t_{\mathrm{sup}} = 8$ nm, and $n_s = 4.25 \times 10^{13}$ cm^{-2} for $t_{\mathrm{inf}} = t_{\mathrm{sup}} = 16$ nm. The Fermi energy is therefore pinned in the valence band of AlN at the top surface in all heterostructures considered here ($n_s > N_{\mathrm{tot}}^{+} = 2 \times 10^{13}$ cm^{-2}).

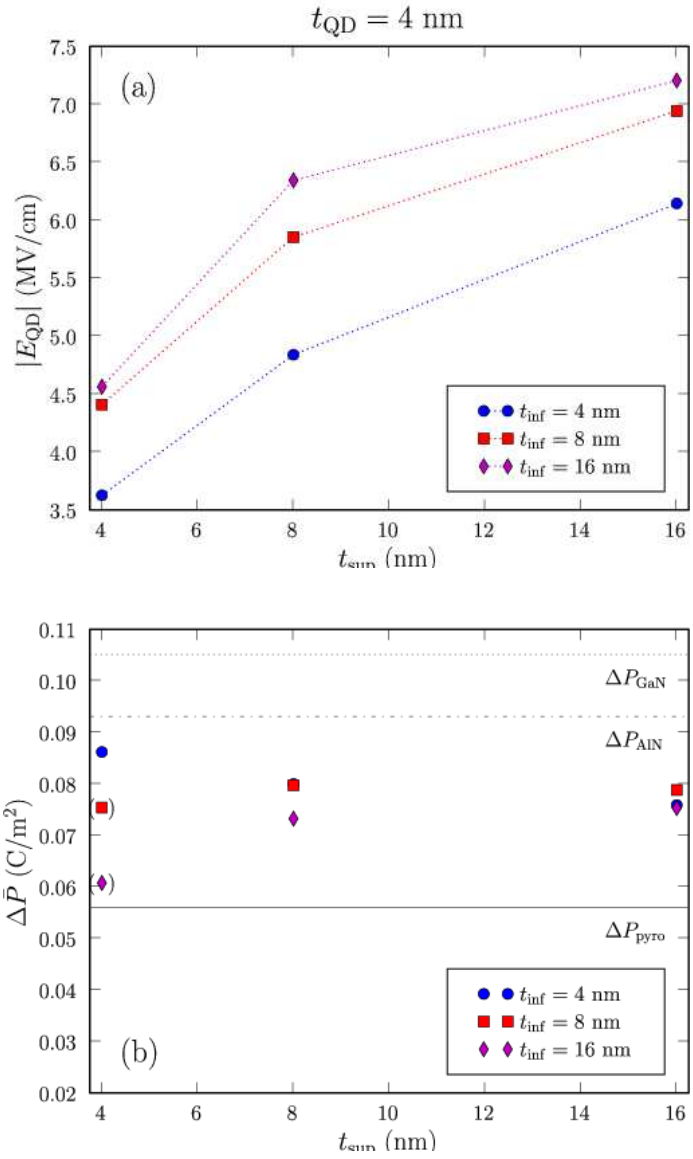

Figure 5.7: (a) The amplitude of the electric field $|E_{QD}|$ in the GaN QD as a function of t_{inf} and t_{sup} ($t_{QD} = 4$ nm). (b) The average polarization discontinuity $\Delta\bar{P}$ deduced from (a) and equation (5.11). The two dots between parentheses are charged with holes.

We would like finally to discuss the role of the lateral surface states. The top surface states play a key role by releasing electrons in the GaN pillar, thereby screening the pyro- and piezo-electric field. The occupied lateral surface states of the upper and lower AlN barrier also act as a (secondary) source of electrons. Most of these extra electrons (as well as the donor electrons) are, however, trapped by the empty lateral surface states of the GaN pillar. As a consequence, the GaN pillar is effectively depleted far away from the heterostructure, and the Fermi level is pinned $\simeq 1.25$ eV below the conduction band edge (see figure. 5.2) (114). This does not, however, have significant influence on the physics of the heterostructure.

5.4 Electronic properties of GaN/AlN nanowire heterostructures

We now discuss the electronic and optical properties of the GaN/AlN nanowire heterostructures, and compare our results with experimental data.

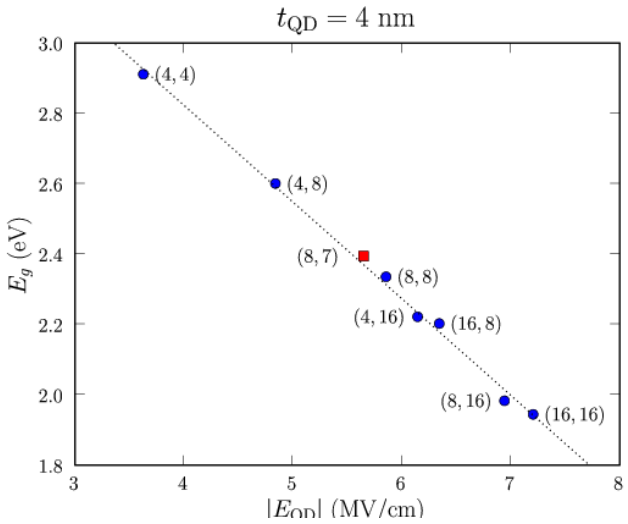

Figure 5.8: The band gap energy of GaN QDs as a function of the electric field - ($t_{QD} = 4$ nm). The dotted line is a guide to the eye. The corresponding (t_{inf}, t_{sup}) are given (in nm) between parenthesis. The red square is the experimental structure discussed in the text.

The tight-binding band gap energy E_g of empty 4 nm thick GaN QDs is plotted as a function of the electric field E_{QD} in figure 5.8. The corresponding values of t_{inf} and t_{sup} are reported between parenthesis. The excitonic correction is not included in this calculation and should further decrease the optical band gap by at most $\simeq 25$ meV. The band gap energy is strongly red-shifted (below the bulk value) by the electric field (Stark effect). It depends almost linearly on E_{QD} and spans around 1 eV in the investigated range of t_{inf} and t_{sup}. The ground-state electron and hole wave functions of a particular QD ($t_{inf} = t_{sup} = 8$ nm) are

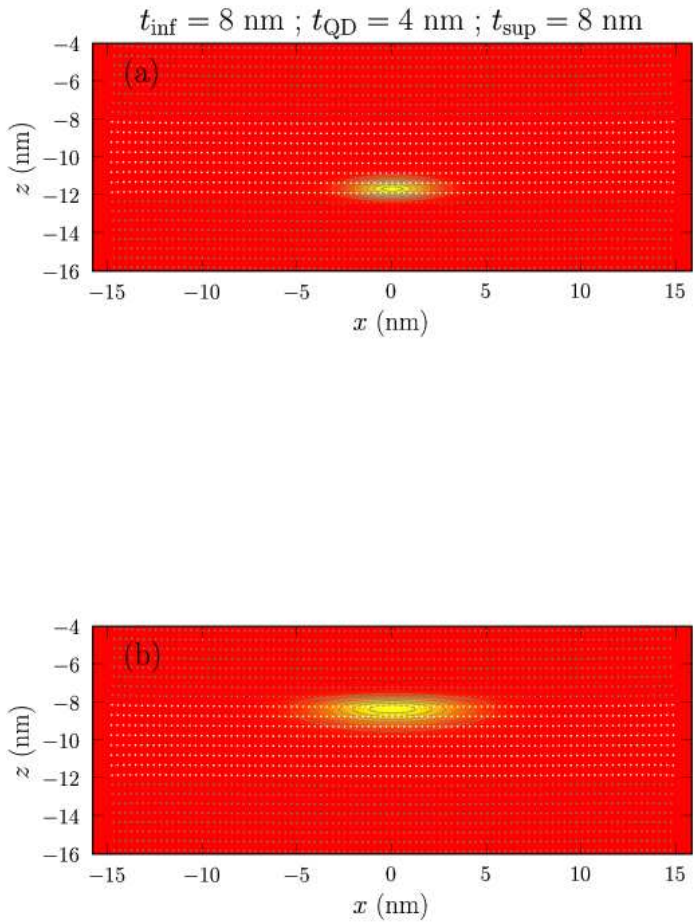

Figure 5.9: The lowest hole (a) and highest electron (b) wave functions in a GaN QD ($t_{QD} = 4$ nm ; $t_{inf} = t_{sup} = 8$ nm). Gallium atoms appear in white, Aluminium atoms in gray.

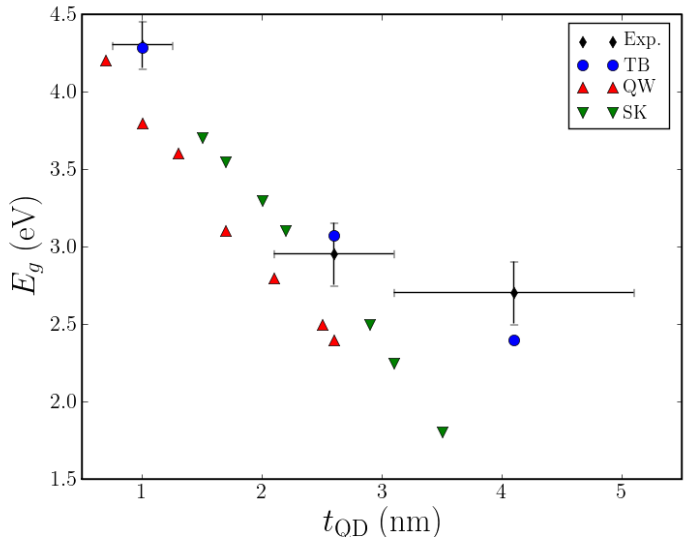

Figure 5.10: The calculated (TB) and experimental (24) (Exp.) band gap energies of the GaN QDs. Experimental GaN/AlN quantum wells (99) (QW) and Stranski-Krastanov (SK) quantum dots (100) with similar sizes are also reported for comparison.

plotted in figure 5.9. As expected, the electron is confined at the upper interface, while the hole is confined at the lower interface of the QD. The electron and hole are, interestingly, both localized around the axis of the nanowire, where the strains are maximum, hence the piezoelectric field slightly larger than at the surface. This helps preventing one of the carriers from being trapped by the charged lateral surface states (114).

Finally, we compare our theoretical predictions with the experimental results of reference (24). In this work, the room-temperature luminescence of 1 to 4 nm thick GaN QDs embedded in 30 nm diameter nanowires showed clear evidence of the quantum confined Stark effect. We have therefore computed the electronic structure of a 1 nm thick QD ($t_{\text{inf}} = 10$ nm, $t_{\text{sup}} = 8$ nm), of a 2.5 nm thick QD ($t_{\text{inf}} = 9$ nm, $t_{\text{sup}} = 10$ nm) and of a 4 nm thick QD ($t_{\text{inf}} = 8$ nm, $t_{\text{sup}} = 7$ nm). The thickness of the barriers was chosen after a detailed analysis of the experimental TEM images (127). The calculated and experimental band gap energies are plotted in figure 5.10. All the dots are empty, which is consistent with the observation of the biexciton in the 1 nm thick QDs (56). The electric field ranges from 5.6 MV/cm for $t_{\text{QD}} = 4$ nm to 7.3 MV/cm for $t_{\text{QD}} = 1$ nm. It is, as expected, much smaller than in GaN/AlN quantum wells (99) (QWs) and Stranski-Krastanov (100) dots (SKs) with similar sizes due to to strain relaxation and screening by the electron gas and surface charges (see the comparison between QWs, SKs and QDs in figure 5.10).

The calculation reproduces the luminescence energies of the 1 and 2.5 nm thick QDs within the error bars, and the downward trend of the electric field with increasing QD size evidenced in the experiment. This agreement supports the conclusion that the Fermi level is

actually pinned in or close to the valence band of AlN at the top surface. Still, the calculation underestimates the luminescence energy of the 4 nm thick QDs, where the Stark effect is the largest, by about 0.3 eV. Looking at figure 5.8, this suggests that the electric field in this QD is overestimated by $\simeq 20$ %. The reason for this discrepancy is unclear at present. Increasing the density of surface states to pin the Fermi level in the bandgap of AlN increases the electric field and ultimately charges the dots. The experimental data have, moreover, been collected at low enough excitation power to prevent screening by photogenerated multiple electron-hole pairs (102; 127). The calculated electric field might be affected by the electromechanical couplings (49; 128) (influence of the electric field on strains), by the uncertainties in the pyro- and piezoelectric constants of GaN and especially AlN, and by their dependence on strains (non-linear piezoelectricity) (63; 129). A simple 1D model however shows that the electromechanical couplings should reduce the electric field by at most $\simeq 5\%$. Plastic strain relaxation in the AlN barriers and slight alloying between GaN and AlN can not be excluded either, but would not be specific to the 4 nm QDs. Further experiments (for different barrier and QD thicknesses) might therefore be needed to get a more complete picture.

5.5 Conclusion

We have modeled the quantum confined Stark effect in AlN/GaN/AlN nanowire heterostructures using a tight-binding approach. We have taken strain relaxation and band bending into account in the calculation of the pyro- and piezoelectric field. We have shown that strain relaxation reduces the piezoelectric polarization, and that the electric field pulls out electrons from the occupied states of the top surface. These electrons accumulate in the GaN pillar below the heterostructure, thereby screening the pyro- and piezoelectric field. We suggest that the electric field is likely strong enough to pin the Fermi level in or close to the valence band edge of AlN at the top surface. As a consequence, the electric field is significantly reduced with respect to GaN/AlN quantum wells or Stranski-Krastanov quantum dots. This is in agreement with recent experimental data on GaN/AlN nanowire heterostructures (24). The calculation however overestimates the electric field in thick quantum dots, which calls for further experiments with different geometries. We have, for this purpose, provided a simple 1D model for the electric field to help the design of such heterostructures.

Chapter 6

Conclusions

Wide band gap nitride semiconductors are now widely used for light emission in the blue and ultraviolet range. Thanks to large band offsets, GaN/AlN heterostructures are also promising candidates for fast telecommunication devices based on intersubband transitions or for high-temperature single photon emitters.

One of the interesting aspects of nanowires compared to bulk material is that their small cross section allows for lateral relaxation, making it possible to combine two materials with different lattice parameters, which grow without obvious dislocations up to a critical cross section. There are, however, residual strains in such nanowire heterostructures, which can still have significant impact on their electronic and optical properties.

In order of study these strains, we have adapted Keating's valence force field model – initially devised for the zinc-blende structures – to arbitrary wurtzite structures. We have derived, in particular the relations between the macroscopic elastic constants c_{ij} and the microscopic bond-bending and bond-stretching constants α and β for arbitrary c/a and u. This model gives a satisfactory description of the elasticity of nitride materials (GaN, AlN and InN). It does directly provide atomic positions suitable for atomistic electronic structure methods like tight-binding.

In this thesis, we have demonstrated the potential accuracy of this valence force field by successfully comparing the results with experimental data like X-Ray diffraction or GPA in TEM images. In the case of GaN/AlN nanowire superlattices without capping, the agreement between experiments and the calculation is consistent with the fact that no dislocations could be identified in the sample at the interfaces between GaN and AlN. In core-shell systems, however, differences between theory and experiment have been observed. Since Keating's model only takes into account elastic relaxation, such discrepancies can be used to diagnose the presence of dislocations associated with plastic relaxation (not accounted for in Keating's model).

The electronic structure of GaN/AlN heterostructures was calculated using the tight-binding method, where the electron and hole states are written as linear combinations of atomical orbitals. In this work we have considered first nearest neighbours two-center $sp^3d^5s^*$ tight-binding models. The effect of strains on the electronic structure of the system can be

characterized by the so-called deformation potentials; at the tight-binding level these are taken into account by a suitable modification of the on-site parameters.

GaN/AlN heterostructures are interesting systems which, due to the low symetry of the wurtzite structure and the ionicity of the bonds, exhibit particular phenomena such as spontaneous polarization and piezoelectricity. This generates a strong electric field along the c axis, which separates the electron from the holes and lowers the bandgap (Stark effect). As an example, we have analyzed a recent experiment on GaN quantum disks embedeed between AlN barriers grown on top of a GaN pillar. The photoluminescence of these disks shifts to the red (below the bulk bandgap) as their thickness increases, a clear sign of the quantum-confined Stark effect. The magnitude of the shift is however lower than in quantum wells or Stranski-Krastanov quantum dots with similar dimensions. We have atually observed in our calculations that the Stark effect is strongly dependent on the geometry of the system. In particular, the electric field is significantly reduced in nanowire by charge redistributions. The electric field indeed pulls out electrons from the occupied states of the top surface. These electrons accumulate in the GaN pillar below the heterostructure, thereby screening the pyro- and piezoelectric field, in agreement with the experimental data. We suggest that the electric field is likely strong enough to pin the Fermi level in or close to the valence band edge of AlN at the top surface. The calculation however overestimates the electric field in the thickest disks, which calls for further experiments with different geometries. We have, for this purpose, provided a simple 1D model for the electric field to help the design of such heterostructures

As future lines of research, several questions need to be adressed regarding these systems:

- The study of the electronical and optical properties of core-shell nanowire heterostructures, in order to understand the photoluminecesnce spectra of this kind of systems.
- The electronic and optical properties of nanowires oriented in a non-polar direction, where the electric field due to spontaneous polarization is oriented along the diameter of the wire and not along the growth axis.
- A new fit of the GaN and AlN tight-binding parameters to have a better account of the effect of strains on the electronic structure.
- For a more complete description of these systems, the effects of the electric field on the strains, i.e. *electro-mechanical couplings*, need to be addressed. They could be introduced in the Keating model through atomic effective charges.
- The calculation of the excitonic contribution to the optical gap.

Publications

- Y. M. Niquet and D. Camacho-Mojica,

  Quantum dots and tunnel barriers in InAs/InP nanowire heterostructures: Electronic and optical properties,

  Phys. Rev. B **77**, 115316 (2008).

- C. Bougerol, R. Songmuang, D. Camacho, Y. M. Niquet, R. Mata, A. Cros, and B. Daudin,

  Structural properties of GaN insertions in AlN nanocolumns,

  Nanotechnology **20**, 295706 (2009).

- D. Camacho and Y. M. Niquet

  Application of Keating's valence force field model to non-ideal wurtzite materials,

  Physica E **42**, 1361 (2009).

- O. Landre, D. Camacho, C, Bougerol, Y. M. Niquet, V. Favre-Nicolin, H Renevier, and B. Daudin,

  Elastic strain relaxation in GaN/AlN nanowire superlattices,

  Accepted for publication in Phys. Rev. B (2010).

- V. Favre-Nicolin, F. Maestropietro, J. Eymery, D. Camacho, Y. M. Niquet, M. Borg, M. E. Messing, L. E Wernersson, R. E. Algra, and E .P. A. M. Bakkers,

  Analysis of strain and staking faults in single nanowires using Bragg coherent diffraction imaging,

  New Journal of Physics (submitted) (2009).

- D. Camacho and Y. M. Niquet,

  Stark effect in GaN/AlN nanowire heterostructures: Influence of strain relaxation and surface states,

  Phys. Rev. B (submitted) (2010).

Bibliography

[1] Y. Cui and C. M. Lieber, Science **291**, 851 (2001). 9

[2] Y.Cui, Q. Wei, H. Park and C.M. Lieber, Science **293**, 1289 (2001). 9

[3] Z. Zhang, C. Hu, Y. Xiong, R. Yang and Z. Wang, Nanotechnology **18**, 46 (2007). 9

[4] J. B. Baxtera and E. S. Aydil, Solar Energy Materials and Solar Cells **90**, 607622 (2006). 9

[5] A. I. Hochbaum, R. Chen, R. Diaz Delgado, W. Liang, E. C. Garnett, M. Najarian, A. Majumdar and P. Yang, Nature **451**, 163 (2008). 9

[6] X. Duan, Y. Hauang, Y cui, J.Wang and C. M. Lieber, Nature **409**, 66 (2001). 9

[7] S.Nakamura, T. Mukai and M. Senoh, Appl. Phys. Lett. **64**, 1687 (1994). 9, 10

[8] W. Lu, J. Xiang, B. P. Timko, Y. Wu, and C. M. Lieber, PNAS **102**, 10046 (2005). 10

[9] M. T. Bjork, B. K. Ohlsson, T. Sass, A. I. Persson, C. Thelander, M. H. Magnussson, K. Deppert, L. R. Wallenger and L. Samuelson, Appl. Phys. Lett. **80**, 1058 (2002). 11

[10] O. Ambacher, J. Phys. D: Appl Phys. **31**, 2653 (1998). 10, 12

[11] R. S. Wagner and W. C. Ellis, Appl. Phys. lett. **4**, 5 (1964). 10

[12] A. M. Morales and C. M. Lieber, Science **279**, 208 (1998). 12

[13] G. B. Stringfellow, Organometallic Vapor-Phase Epitaxy, Theory and Practice, Academic Press, San Diego, California (1999). 12

[14] J. Ristic, E. Calleja, S. Fernandez-Garrido, L. Cerutti, A. Trampert, U.Jahn and K. H. Ploog, J. Cryst. Growth **310**, 4035 (2008). 12

[15] R. Koester, J. S. Hwang, C. Durand, D. Le Si Dang and J. Eymery, Nanotechnology **21**, 015602 (2010). 12

[16] K. A. Bertness, A. Roshko, L. M. Manasfield, T. E. Harvey and N. A. Sanford, J. Cryst. Growth **310**, 3154 (2008).

[17] J.Stangl, V. Holy and G. Bauer, Rev. Mod. Phys. **76**, 725 (2004). 13

[18] M. S. Gudiksen, L. J. Lauhon, J. Wang, D. C. Smith and C. M. Lieber, Nature **415**, 617 (2002). 13

[19] L. J. Lauhon, M. S. Gudiksen, J. Wang, D. C. Smith and C. M. Lieber, Nature **420**, 57 (2002). 13

[20] I. N. Stranski and L. Krastanow, Sitzungsber. Akad. Wiss. Wien, Math- Naturwiss. Abat 2b **146**, 797 (1938). 13, 14

[21] M. T. Bjork, B. J. Ohlsson, T. Sass, A. I. Persson, C. Thelander, M. H. Magnusson, K. Deppert, L. R. Wallenberg and L. Samuelson, Appl. Phys. Lett. **80**, 6 (2002). 14

[22] E. Ertekin, P. A. Greaney, D. C. Chrzan and T. D. Sands, J. Appl. Phys. **97**, 114325 (2005). 14, 28, 30, 36, 83

[23] F. Glas, Phys. Rev. B **74**, 121302 (2006). 14, 28, 36, 83

[24] J. Renard, R. Songmuang, G. Tourbot, C. Bougerol, B. Daudin and B. Gayral, Phys. Rev. B. **80** 121305 (2009). 15, 16, 17, 73, 74, 79, 83, 88, 99, 100, 111

[25] F. Livet, Acta Crystalographica A. foundations of Crystallography **63** , 87 (2007).

[26] G. L. Bir and G. E. Pikus, Symmetry and Strain-Induced Effects in Semiconductors (Wiley, New York, 1974). 19, 56

[27] D. L. Smith and C. Mailhiot, Rev. Mod. Phys. **62**, 173 (1990). 19

[28] Y. M. Niquet, Phys. Rev. B. **74**, 155304 (2006). 19

[29] S. Schulz, A.Berube and E. P. O'Reilly, Phys. Rev. B.**79**, 081401 (2009). 19, 84, 87

[30] L. D. Landau and E. M. Lifshitz, Theory of Elasticity (Elsevier, Oxford, 1986). 19

[31] C. Pryor, J. Kim, L. W. Wang, A. J. Williamson and A. Zunger, J. Appl. Phys. **83**, 2548 (1998). 19, 84

[32] G. Bastard, Wave Mechanics Applied to Semiconductor Heterostruecteres (Les Editions de Physique, Les Ulis, 1988). 19, 56

[33] S. L. Chuang and C. S. Chang, Phys. Rev. B **54**, 4 (1996). 19, 46, 50

[34] J. C. Slater and G. F. Koster Phys. Rev. B **94** (1954). 19, 42, 88

[35] C. Delerue and M. Lannoo, Nanostructures: Theory and Modelling (Springer, New York, 2004). 19

[36] J. R. Chelikowsky and M. L. Cohen, Phys. Rev. B **14**, 556 (1976) ; Phys. Rev. B **30**, 4828(E) (1984). 19

[37] L. W. Wang and A. Zunger, Phys. Rev. B **51**, 17398 (1995). 19

[38] L. Kleinman, Phys. Rev. **128**, 2614 (1962). 19

[39] P. N. Keating, Phys. Rev. **145**, 637 (1966). 19, 22, 24, 84

[40] J. Tersoff, Phys. Rev. B **37**, 6991 (1988). 19

[41] F. Stillinger and T. A. Weber, Phys. Rev. B **31**, 5262 (1985). 19

[42] R. M. Martin, Phys. Rev. B **1**, 4005 (1970). 19, 23

[43] R. M. Martin, Phys. Rev. B **6**, 4546 (1972). 19, 25

[44] S. Yu. Davidov and A. V. Solomonov, Tech. Phys. Lett. **25**, 601 (1999). 19, 25

[45] C. Kittel, Introduction to Solid State Physics, Wiley (1956). 23

[46] I. Vurgaftman and J. R. Meyer, J. Appl. Phys. **94**, 3675 (2003). 26, 44, 51, 55, 67, 87

[47] J. M. Wagner and F. Bechsted, Phys. Rev. B **66**, 115202 (2002). 26

[48] B. Jogai, J. Appl. Phys. **93**, 1631 (2003). 26, 83, 84, 86, 87

[49] B. Lassen, D. Barettin, M. Willatzen and L. C. Lew Yan Voon, Microelectronics Journal **39**, 1226 (2008). 26, 100

[50] W. A. Harrison, Elementary Electronic Structure, World Scientific, Singapore (1999). 26

[51] J. W. Mattews and A. E. Blakeslee, J. Cryst. Growth **27**, 118 (1974). 36

[52] J. Ristic, J. M. Calleja, U. Jahn, A. Trampert and K. H. Ploog, Phys. Rev. B **68**, 125305 (2003). 28

[53] J. B. Schlager, N. A. Sanford, K. A. Bertness, J. M. Barker A. Roshko and P. T. Blanchard, Appl. Phys. Lett. **88**, 213106 (2006). 28

[54] S. N. Yi *et al.*, Appl Phys. Lett. **90**, 101901 (2007). 28

[55] M. Tchernycheva *et al.*, Nanotechonology **18**, 385306 (2007). 28

[56] J. Renard, R. Songmuang, C. Bougerol, B. Daudin and B. Gayral, Nano Lett. **8**, 2092 (2008). 28, 83, 99

[57] A. Kikuchi, M Kawai, M. Tada and K. Kishino, Japan. J. Appl. Phys. **43**, L1524 (2004). 28

[58] H. M. Kim, Y. H. Cho, H. S. Lee, S. I. Kim, S. R. Ryu, D. Y. Kim, T. W. Kang and K. S. Chung, Nano Lett. **4**, 1059 (2004). 28

[59] H. Sekiguchi, K. Kishino and A. Kikuchi, Electron. Lett. **44**, 151 (2008). 28

[60] S. Raychaudhuri and E. T. Yu, J. Appl. Phys. **99**, 114308 (2006). 28, 30

[61] C. Bougerol, R. Songmuang, D. Camacho, Y. M. Niquet, R. Mata, A. Cros and B. Daudin, Nanotechnology **20**, 295706 (2009). 29, 34

[62] W. H. Press, W. T. Vetterling and B. P. Flannery, Numerical Recipies in Fortran, Cambridge University Press, (1992) 30

[63] Y. M. Niquet, Nano Letters **7**, 1105 (2007). 30, 84, 100

[64] R. Songmuang, O. Landre and B. Daudin, Appl. Phys. Lett. **91**, 251902 (2007). 32

[65] C. Roder, S. Einfeldt, S. Figge and D. Hommel, Phys. Rev. B **72**, 085218 (2005). 32, 33

[66] S. Figge, H. Krancke, D. Hommel and B. M. Epelbaum, Appl. Phys. Lett. **94**, 101915 (2009). 32, 33

[67] R. R. Reeber and K. Wang, J. Nitride Semicond. Res. **6**, 3 (2001). 33

[68] F. Kandaswamy, F. Guillot, E. Bellet-Amalric, E. Monroy, L. Nevou, M. Tchernycheva, A. Michon, F. H. Julien, E. Baumann, F. R. Giorgetta, D. Hafostetter, T. Remmele, M. Albrecht, S. Birner and Le Si Dang, J. Appl. Phys. **104**, 093501 (2008). 34

[69] O. Landré, V. Fellmann, P. Jaffrennou, C. Bougerol, H. Renevier, A. Cros and B. Daudin, submitted to Appl. Phys. Lett. 36

[70] D. Rideau, M. Feraille. M. Michaillat, Y. M. Niquet, C. Tavernier and H. Jaouen, Sol. State. Elec. **53**, 452 (2009). 39

[71] Y. M. Sirenko, J. B. Jeon, B. C. Lee, K. W. Kim, M. A. Littlejohn, M. A. Stroscio and G. J. Iafrate, Phys. Rev. B **55**, 7 (1997). 46

[72] Y. M. Niquet and D. Camacho Mojica, Phys. Rev. B. **77**, 115316 (2008). 52, 84, 95

[73] G. Klimeck, S. S. Ahmed, Hansang Bae, N. Kharche, S. Clark, Prada et al IEEE Trans Electron Devices **54**, 2079 (2007). 52

[74] C. Priester, G. Allan and M. Lannoo, Phys. Rev. B. 8519 (1988). 52

[75] J. M. Jancu and P. Voisin, Phys. Rev. B. **76**, 115202 (2007). 52

[76] T. B. Boykin, G. Klimeck and R. C. Bowen, Phys. Rev. B. **66** 125207 (2002) 52

[77] Y. M. Niquet, D. Rideau, C. Tavernier, H. Jaouen and X. Blase, Phys. Rev. B **79**, 245201 (2009). 52, 54

[78] J. M. Jancu, F. Bassani, F. Della Sala and R. Scholz. Appl. Phys. Lett. **81**, 4838 (2002). 44, 45, 52, 54, 55, 88

[79] M. T. Björk, B. J. Ohlsson, T. Sass, A. I. Persson, C. Thelander, M. H. Magnusson, K. Deppert, L. R. Wallenberg and L. Samuelson, Appl. Phys. Lett. **80**, 1058 (2002). 55, 59

[80] M. T. Björk, B. J. Ohlsson, C. Thelander, A. I. Persson, K. Deppert, L. R. Wallenberg and L. Samuelson, Appl. Phys. Lett. **81**, 4458 (2002). 56, 59

[81] C. Thealander, H. A.Nilsson, L. E. Jensen and L. Samuelson, Nano Lett. **5**, 635 (2005). 56, 59

[82] H. A. Nilsson, C. Thealander, L. E. Froberg, J. B. Wagner and L. Samuelson, Appl. Phys. Lett. **89**, 16101 (2006). 56, 59

[83] M. Zervos and L. F. Feiner, J. Appl. Phys. **95**, 281 (2004). 56

[84] C. G. Van de Walle, Phys. Rev. B **39**, 1871 (1989). 56

[85] Y. M. Niquet, A. Lherbier, N. H. Quang, M. V. Fernandez-Serra, X. Blase and C. Delerue, Phys. Rev. B **73**, 165319 (2006). 56, 60

[86] M. T. Björk, B. J. Ohlsson, T. Sass, A. I. Persson, C. Thelander, M. H. Magnusson, K. Deppert, L. R. Wallenberg and L. Samuelson, Nano Lett. **2**, 87 (2002). 59

[87] S. Nakamura, M. Senoh, S. Nagahama, N. Iwasa, T. Yamada, T. Matsushita, Y. Sugimoto and H. Kiyoku, Appl. Phys. Lett. **69**, 4056 (1996). 83

[88] F. A. Ponce and D. P. Bour, Nature **386**, 351 (1997). 83

[89] A. J. Fischer, A. A. Allerman, M. H. Crawford, K. H. A. Bogart, S. R. Lee, R. J. Kaplar, W. W. Chow, S. R. Kurtz, K. W. Fullmer and J. J. Figiel, Appl. Phys. Lett. **84**, 3394 (2004). 83

[90] L. Nevou, N. Kheirodin, M. Tchernycheva, L. Meignien, P. Crozat, A. Lupu, E. Warde, F. H. Julien, G. Pozzovivo, S. Golka, G. Strasser, F. Guillot, E. Monroy, T. Remmele and M. Albrecht, Appl. Phys. Lett. **90**, 223511 (2007). 83

[91] S. Kako, C. Santori, K. Hoshino, S. Götzinger, Y. Yamamoto and Y. Arakawa, Nature Mat. **5**, 887 (2006). 83

[92] F. Bernardini, V. Fiorentini and D. Vanderbilt, Phys. Rev. B **56**, R10024 (1997) ; A. Zoroddu, F. Bernardini, P. Ruggerone and V. Fiorentini, Phys. Rev. B **64**, 045208 (2001). 83

[93] O. Ambacher, J. Smart, J. R. Shealy, N. G. Weimann, K. Chu, M. Murphy, W. J. Schaff, L. F. Eastman, R. Dimitrov, L. Wittmer, M. Stutzmann, W. Rieger and J. Hilsenbeck, J. Appl. Phys. **85**, 3222 (1999). 83, 84, 86

[94] J. P. Ibbetson, P. T. Fini, K. D. Ness, S. P. DenBaars, J. S. Speck and U. K. Mishra, Appl. Phys. Lett. **77**, 250 (2000). 83, 84, 86, 87, 93

[95] H. W. Jang, C. M. Jeon, K. H. Kim, J. K. Kim, S.-B. Bae, J.-H. Lee, J. W. Choi and J.-L. Lee, Appl. Phys. Lett. **81**, 1249 (2002). 83, 84, 86, 87

[96] G. Koley and M. G. Spencer, Appl. Phys. Lett. **86**, 042107 (2005). 83, 84, 86, 87

[97] F. Widmann, J. Simon, B. Daudin, G. Feuillet, J. L. Rouvière, N. T. Pelekanos and G. Fishman, Phys. Rev. B **58**, R15989 (1998). 83

[98] J. Simon, N. T. Pelekanos, C. Adelmann, E. Martinez-Guerrero, R. André, B. Daudin, Le Si Dang and H. Mariette, Phys. Rev. B **68**, 035312 (2003). 83

[99] C. Adelmann, E. Sarigiannidou, D. Jalabert, Y. Hori, J.-L. Rouvière, B. Daudin, S. Fanget, C. Bru-Chevallier, T. Shibata and M. Tanaka, Appl. Phys. Lett. **82**, 4154 (2003). 74, 75, 83, 84, 99

[100] T. Bretagnon, P. Lefebvre, P. Valvin, R. Bardoux, T. Guillet, T. Taliercio, B. Gil, N. Grandjean, F. Semond, B. Damilano, A. Dussaigne and J. Massies, Phys. Rev. B **73**, 113304 (2006). 74, 75, 83, 99

[101] A. D. Andreev and E. P. O'Reilly, Phys. Rev. B **62**, 15851 (2000). 84

[102] V. Ranjan, G. Allan, C. Priester and C. Delerue, Phys. Rev. B **68**, 115305 (2003). 84, 100

[103] J. Ristić, C. Rivera, E. Calleja, S. Fernández-Garrido, M. Povoloskyi and A. Di Carlo, Phys. Rev. B **72**, 085330 (2005). 84

[104] O. Marquardt, D. Mourad, S. Schulz, T. Hickel, G. Czycholl and J. Neugebauer, Phys. Rev. B **78**, 235302 (2008). 84

[105] D. Camacho and Y. M. Niquet, Physica E **42**, 1361 (2010). 84

[106] The nanowires, though shorter than in the experiments of Ref. (24), are long enough to converge strains and potentials. 84

[107] The strains are defined from the deformations of tetrahedra built from atoms belonging to the same sublattice. 84

[108] The heterostructure is placed at the center of the finite difference box, with the nanowire protruding out on one side of the box. Von Neumann (zero normal electric field) boundary conditions are applied on that side of the box, while Dirichlet ($V = 0$) boundary conditions are applied on the others. The convergence of the electric field in the GaN QD with respect to the size of the box has been carefully checked. 86

[109] Y. M. Niquet, Phys. Rev. B **74**, 155304 (2006). 86, 95

[110] H. Harima, Journal of Physics: Cond Matter **14**, R967-R993 (2002). 86

[111] S. M. Sze and Kwok K. Ng, *Semiconductor Devices: Physics and Technology* (3^{rd} edition, Wiley-Interscience, New-York, 2006). 86

[112] H. Morkoç, *Handbook of Nitride Semiconductors and Devices*, Vol. 1 (Wiley-VCH, Weinheim, Germany, 2008). 87

[113] V. Schmidt, S. Senz and U. Gösele, Appl. Phys. A **86**, 187 (2007). 86

[114] B. S. Simpkins, M. A. Mastro, C. R. Eddy Jr. and P. E. Pehrsson, J. Appl. Phys. **103**, 104313 (2008). 86, 97, 99

[115] R. M. Feenstra, Y. Dong and C. D. Lee, J. Vac. Sci. Technol. B **23**, 1174 (2005). 86

[116] J. E. Northrup, R. Di Felice and J. Neugebauer, Phys. Rev. B **55**, 13878 (1997). 87

[117] J. Fritsch, O. F. Sankey, K. E. Schmidt and J. B. Page, Phys. Rev. B **57**, 15360 (1998). 87

[118] D. Segev and C. G. Van de Walle, Europhys. Lett. **76**, 305 (2006). 87

[119] C. G. Van de Walle and D. Segev, J. Appl. Phys. **101**, 081704 (2007). 87

[120] M. S. Miao, A. Janotti and C. G. Van de Walle, Phys. Rev. B **80**, 155319 (2009). 87

[121] Y. Dong, R. M. Feenstra and J. E. Northrup, J. Vac. Sci. Technol. B **24**, 2080 (2006) ; Appl. Phys. Lett. **89**, 171920 (2006). 87

[122] W. H. Press, S. A. Teukolsky, W. T. Vetterling and B. P. Flannery, *Numerical Recipes in Fortran* (Cambridge University Press, 1992). 88

[123] A. Di Carlo, Semicond. Sci. Technol. **18**, R1 (2003). 88

[124] C. Delerue and M. Lannoo, *Nanostructures: Theory and Modelling* (Springer, New York, 2004). 88

[125] G. L. G. Sleijpen and H. A. Van der Vorst, SIAM Journal on Matrix Analysis and Applications **17**, 401 (1996) ; SIAM Review **42**, 267 (2000). 88

[126] Y. M. Niquet, A. Lherbier, N. H. Quang, M. V. Fernández-Serra, X. Blase and C. Delerue, Phys. Rev. B **73**, 165319 (2006). 88

[127] J. Renard, R. Songmuang, G. Tourbot, C. Bougerol, B. Daudin and B. Gayral, private communication. 99, 100

[128] B. Jogai, J. D. Albrecht and E. Pan, J. Appl. Phys. **94** 3984 (2003). 100

[129] G. Bester, X. Wu, D. Vanderbilt and A. Zunger, Phys. Rev. Lett. **96**, 187602 (2006). 100

Résumé

Nous avons modélisé les propriétés structurales et électroniques d'hétérostructures de nanofils de nitrures GaN/AlN à l'aide de méthodes de simulation atomistiques. Nous avons tout d'abord construit un champ de forces "à la Keating" pour les matériaux wurtzite afin de calculer les positions atomiques et la distribution des contraintes dans ces hétérostructures. Grâce à ce modèle, nous avons pu suggérer la présence ou confirmer l'absence de dislocations dans différentes hétérostructures de nanofils GaN/AlN caractérisées expérimentalement par microscopie électronique et diffraction de rayons X. Nous avons ensuite étudié les propriétés électroniques et optiques de ces nanostructures avec la méthode des liaisons fortes. Nous nous sommes particulièrement intéressés à l'effet des champs électriques internes sur les nanofils GaN/AlN. Les expériences de spectroscopie optique ont en effet mis en évidence un important décalage vers le rouge (effet Stark confiné) des raies de luminescence de ces fils, consécutif à la séparation des électrons et des trous par les champs pyro- et piezoélectriques. Ce décalage est toutefois inférieur à celui mesuré sur des puits et des boîtes de dimensions équivalentes. Pour l'expliquer, nous avons montré qu'il était essentiel de tenir compte de l'écrantage du champ électrique par les charges déplacées par celui-ci, et en particulier depuis les états de surface des nanofils. Nous avons notamment proposé un modèle analytique simple pour comprendre les tendances et aider la conception des hétérostructures de nanofils de nitrures.

Mots-clés : Nanofils, nitrures, polarisation spontanée, piezoélectricité, effet Stark, confinement, liaisons fortes.

Abstract

We have modeled the structural and electronic properties of nitride GaN/AlN nanowire heterostructures with atomistic simulation methods. We have first derived a Keating-like valence force field model for arbitrary wurtzite materials in order to compute the atomic positions and strain distribution in these heterostructures. With this model, we have been able to suggest the presence or confirm the absence of dislocations in various GaN/AlN nanowire heterostructures characterized by electron microscopy or X-Ray diffraction. We have then studied the electronic and optical properties of these nanostructures with the tight-binding method. We have been particularly interested in the effect of the internal electric field on GaN/AlN nanowires. Optical spectroscopy experiments have indeed evidenced a strong redshift of the luminescence of these nanowires (quantum confined Stark effect), due to the separation of the electrons and holes by the pyro- and piezoelectric field. This redshift is however smaller than measured in quantum wells and quantum dots with similar dimensions. To explain this, we have shown that it is essential to account for the screening of the electric field by the charges displaced by the latter, in particular from the surface states of the nanowire. We have proposed a simple analytical model to understand the main trends and help the design of nitride nanowire heterostructures.

Keywords : Nanowires, nitrides, spontaneous polarization, piezoelectricity, Stark effect, confinement, tight-binding.